ANL-7444
Engineering and
Equipment

ARGONNE NATIONAL LABORATORY
9700 South Cass Avenue
Argonne, Illinois 60439

THE INTERACTION OF TWO-DIMENSIONAL, STRATIFIED, TURBULENT AIR-WATER AND STEAM-WATER FLOWS

by

John H. Linehan

Reactor Engineering Division

A thesis submitted in partial fulfillment
of the requirements for the degree of
Doctor of Philosophy
(Mechanical Engineering)
at The University of Wisconsin

May 1968

DISCLAIMER

TABLE OF CONTENTS

TABLE OF CONTENTS

TABLE OF CONTENTS

LIST OF FIGURES

LIST OF FIGURES

LIST OF FIGURES

LIST OF TABLES

NOMENCLATURE

a_1	Constant of integration
a_2	Constant of integration
A_{or}	Area of orifice, ft^2
b	Channel spacing, ft
$c_n(x)$	Polynomial coefficients in Eq 82
C	Electrical conductance of films, mhos
C_{or}	Orifice coefficient, dimensionless
C_v	Specific heat at constant volume, Btu/lb_m-°F
C_p	Specific heat at constant pressure, Btu/lb_m-°F
d_1	Constant in Eq 147
d_2	Constant in Eq 150
d_3	Constant equal to the film Stanton number
e	Unit vector
E_A	Voltage in conductance probes circuit, volts
E_B	Voltage in conductance probes circuit, volts
E_C	Voltage in conductance probes circuit, volts
f_b	Wall friction factor, dimensionless
f_i	Interfacial friction factor, dimensionless
Fr	Froude number
g	Gravitational acceleration, ft/sec^2
g_y	Gravitational acceleration in y direction, ft/sec^2
g_c	Unit conversion factor
h	Heat-transfer coefficient, $Btu/hr\text{-}ft^2\text{-}°F$
h_{fg}	Latent heat of vaporization, Btu/lb_m
h_g	Enthalpy of steam, Btu/lb_m
h_ℓ	Enthalpy of liquid, Btu/lb_m
h_0	Enthalpy of liquid at wall surface temperature, Btu/lb_m
i	Unit vector in x direction
I	Current through conductance probes, Amps
j	Unit vector in y direction
k	Thermal conductivity, Btu/hr-ft-°F
k_ℓ	Thermal conductivity of liquid, Btu/hr-ft-°F
K_ℓ	Turbulent thermal conductivity of liquid, Btu/hr-ft-°F
L	Characteristic length, ft
m	Indexing integer for computer calculation
n	Unit normal vector at the interface
N	Order of polynomial in Eq 82
Nu_ℓ	Nusselt number of water
P	Static pressure, lb_f/ft^2
P_a	Static pressure in air, lb_f/ft^2
$\hat{P}_a$	Static pressure in air, dimensionless
P_ℓ	Static pressure in liquid, lb_f/ft^2
$\hat{P}_\ell$	Static pressure in liquid, dimensionless
P_s	Static pressure in steam, lb_f/ft^2
Pr_ℓ	Prandtl number of water
ΔP_{or}	Pressure difference across the orifice plate, lb_f/ft^2
q_c	Interface heat flux, $Btu/hr\text{-}ft^2$
R_h	Hydraulic diameter, ft
R_p	Electrical resistance of film, ohms
Re_a	Reynolds number of air
Re_ℓ	Reynolds number of liquid
Re_s	Reynolds number of steam
St_ℓ	Stanton number of liquid
t	Film thickness, ft
t	Unit tangent vector at the interface
t^+	Dimensionless film thickness, tu^*/ν_ℓ
$\hat{t}$	Film thickness, dimensionless
T	Temperature, °F
T_ℓ	Temperature of liquid, °F
T_0	Temperature of liquid at wall, °F
T_s	Temperature of steam, °F
u	Velocity, ft/sec
$\hat{u}$	Velocity, dimensionless
$\bar{u}$	Mass average velocity, ft/sec
u^*	Friction velocity, ft/sec
u_a	Air velocity, ft/sec
$\hat{u}_a$	Air velocity, dimensionless
$\bar{u}_a$	Mass average air velocity, ft/sec
$\bar{u}_{a_0}$	Mass average air velocity at x = 0, ft/sec
u_ℓ	Water velocity, ft/sec
u_ℓ^+	Water velocity, dimensionless
$\hat{u}_\ell$	Water velocity, dimensionless
$\bar{u}_{\ell_0}$	Mass average water velocity at x = 0, ft/sec
$\bar{u}_\ell$	Mass average water velocity, ft/sec
u_s	Steam velocity, ft/sec
$\bar{u}_s$	Mass average steam velocity, ft/sec
V	Fluid velocity, ft/sec
v	Velocity, ft/sec
$\hat{v}$	Velocity, dimensionless
v_a	Air velocity, ft/sec
$\hat{v}_a$	Air velocity, dimensionless
v_ℓ	Liquid velocity, ft/sec
$\hat{v}_\ell$	Liquid velocity, dimensionless
w	Width of channel, ft
W	Orifice flowrate, lb_m/sec
W_a	Mass flowrate of air per unit width of channel, $lb_m/sec\text{-}ft$
W_ℓ	Mass flowrate of water per unit width of channel, $lb_m/sec\text{-}ft$
W_s	Mass flowrate of steam per unit width of channel, $lb_m/sec\text{-}ft$
$\overline{W}_a$	Mass flowrate of air, lb_m/sec
$\overline{W}_\ell$	Mass flowrate of water, lb_m/sec
$\overline{W}_s$	Mass flowrate of steam, lb_m/sec
x	Rectangular coordinate, ft
$\hat{x}$	Dimensionless distance
y	Rectangular coordinate, ft
$\hat{y}$	Dimensionless distance
y^+	Dimensionless distance, yu^*/ν_ℓ

Greek Letters

α_ℓ	Turbulent thermal diffusivity, ft^2/sec
β	Ratio of average liquid velocity to interface velocity, dimensionless
β_{or}	Ratio of orifice area to pipe area, dimensionless
γ	Defined in Eq 67
δ	Defined in Eq 150, ft
Δ	Incremental value of x, ft
ϵ	Defined in Eq 68
ϵ_H	Eddy diffusivity, ft^2/sec
η	Constant in Eq 161, dimensionless
θ	Time, sec
λ_1	Interface friction factor, dimensionless
λ_1^*	Interface friction factor, with condensation, dimensionless
μ	Dynamic viscosity, $lb_m/ft\text{-}sec$
μ_a	Dynamic viscosity of air, $lb_m/ft\text{-}sec$
μ_ℓ	Dynamic viscosity of water, $lb_m/ft\text{-}sec$
μ_s	Dynamic viscosity of steam, $lb_m/ft\text{-}sec$
ν_a	Kinematic viscosity of air, ft^2/sec
ν_ℓ	Kinematic viscosity of water, ft^2/sec
ρ	Density, lb_m/ft^3
ρ_a	Density of air, lb_m/ft^3
ρ_{avg}	Average density across orifice, lb_m/ft^3
ρ_ℓ	Density of water, lb_m/ft^3
ρ_s	Density of steam, lb_m/ft^3
σ_{xx}	Normal stress, lb_f/ft^2
σ_{yy}	Normal stress, lb_f/ft^2
τ_b	Wall shear stress in gas phase, lb_f/ft^2
τ_i	Interface shear stress, lb_f/ft^2
τ_0	Wall shear stress in film, lb_f/ft^2
$\underline{\tau}$	Shear stress tensor, lb_f/ft^2
τ_{xy}	Shear stress, lb_f/ft^2
ϕ	Condensation parameter defined in Eq. 127, dimensionless
Φ	Viscous dissipation function, sec^{-2}

THE INTERACTION OF TWO-DIMENSIONAL, STRATIFIED, TURBULENT AIR-WATER AND STEAM-WATER FLOWS

by

John H. Linehan

SUMMARY

In this report, analytical models based on an integrated form of the boundary-layer-type equation are developed to describe the interaction of two-dimensional, stratified, turbulent, two-phase fluids. Particular emphasis was placed on the description of flows whereby the gas-phase velocity is at least an order of magnitude larger than the liquid-phase velocity and the gas-phase momentum is the same order of magnitude as the liquid-phase momentum. Under these circumstances, where the momentum transferred from the gas phase to the liquid phase plays a significant role in the behavior of the liquid, the liquid phase occupies a small portion of the flow and is referred to as a film.

The models developed in this report were compared to experiments performed in a horizontal test section whose inner dimensions were 6 by 21/32 in. In the two-component experiments, air flowed over water; in the one-component experiments, steam flowed over water. The film thicknesses in the air-water experiments were measured by the conductance-probes method, and in the steam-water experiments, by the needle-contact-probe method.

In turbulent flow, the phase interface is generally characterized by a complex wave structure. For two-component flows, correlations were proposed for the determination of the momentum transferred from the gas phase to the film via turbulent shear stress. In the three-dimensional and roll-wave regimes, the interfacial friction factor was satisfactorily represented by a linear function of the film Reynolds number only. For one-component flows, where the film was subcooled with respect to the temperature of the saturated vapor, the interfacial shear stress was augmented by a term proportional to the product of the average vapor velocity and the condensation rate. The interface shear stress during film condensation was significantly larger than the two-component turbulent shear stress.

The wall shear stress in the film was evaluated using the wall-layer-model concept and the von Karman universal velocity profile. The wall-layer model satisfactorily predicted the wall shear stress up to 5000, the highest film Reynolds number encountered in the air-water experiments.

Since the film thickness varied in the experiments, the hydrostatic pressure in the film varied in proportion to the axial gradient of film thickness. The hydrostatic pressure variation was an important term in the momentum equations, especially for the low water flowrates.

In the development of the model of film condensation, it was assumed that condensation occurred as a result of the subcooling of the film. A model which emphasized the effect of interfacial wave motion on the transport of heat in the film, was proposed for evaluating the condensing heat-transfer coefficient. This model predicted that the film Stanton number was a constant. The steam-water experiments verified the constancy of the film Stanton number within the range of experimental error; its value was 0.0073.

I. INTRODUCTION

An understanding of the interaction at the phase interface in the concurrent stratified flow of gas and liquid films is of considerable value in the engineering design of various processes. Consider, for example, the liquid-metal MHD film generator. In the film generator, the working fluid is a two-phase mixture prepared so that the phases are, in principle, separated and flow through the generator in a stratified manner. The high-velocity free-surface film that is formed interacts with the magnetic field. The ensuing losses of momentum in the film may be compensated through the momentum exchange between the gas and liquid at the phase interface. For a high-velocity, two-component gas and liquid, this interaction is through the turbulent shear stress at the wavy gas-liquid interface. In a one-component fluid, additional momentum can be transferred from the vapor to the liquid by subcooling the liquid film, causing condensation. In the above example, comparison of the one- and two-component film generators necessitates a fundamental understanding of the effects of the transport processes at the gas-liquid interface on the physical behavior of the film. In addition to the film generator, the interaction at the phase interface is of importance in the following: film cooling of rocket motors, turbine blades, etc., conveying of liquids by concurrent gas streams as in oil pipelines, annular film boiling, etc.

To elucidate the effects of interfacial transport processes on film flow, this report is concerned with the horizontal, concurrent, stratified flow of a turbulent gas stream over a turbulent liquid film. In the two-component case, the only interaction of interest between the gas stream and liquid film is the interface shear stress. In the one-component case, an additional interaction between the vapor stream and liquid film at the phase interface is considered as a result of condensation of the vapor. The one- and two-component fluids selected for consideration in the experimental portion of this report were, respectively, steam-water and air-water.

A. Previous Work

1. Two-component Concurrent Stratified Flow

Many aspects of the flow of a film in the presence of a concurrent gas phase have been studied. An excellent review, including an extensive bibliography, covering all phases of the research on film flow has been prepared by Fulford.[19] The following discussion considers only those results relevant to the research presented here.

The interface between gas and liquid phases that are flowing concurrently is usually characterized by the presence of wavelike disturbances. Hanratty and Woodmansee[23] observed five distinct interfacial conditions for the flow of air over liquid films:

1) Smooth interface.

2) Two-dimensional waves: long crested waves extended over the entire breadth of the channel.

3) Three-dimensional waves: a cross-hatched wave structure giving the surface a pebbly appearance.

4) Roll waves: large-amplitude, long-crested waves superimposed on a pebbly structure.

5) . Atomization or entrainment: liquid drops torn from the film and carried in the gas phase.

In general, a smooth interface between the gas and liquid phases is difficult to produce in the laboratory. For example, in the turbulent flow of air over water, Cohen[9] found that the interface was always disturbed.

The presence of interfacial disturbances has been a complicating factor in arriving at a physical understanding of the interfacial shear stress in film flow. This has provided the impetus to develop correlations, for the interfacial shear stress, which are related to some overall properties of the flow, such as the film and gas Reynolds numbers. A correlation of this type would alleviate the necessity of considering the details of the interfacial transport mechanisms. The experimental flow systems normally used in determining the correlation can be classified as either the annular flow of gas and liquid phases inside a pipe or the stratified flow of gas and liquids over vertical or horizontal surfaces. In either case, the direct measurement of an interfacial shear stress is not practical. The indirect determination involves consideration of the changes in momentum of the gas and liquid phases, the pertinent wall shear stresses, and the pressure gradient.

A desirable means of indirectly measuring the interface shear stress is to study the flow in a region where it is "fully developed," i.e., where the momentum change in the gas and liquid phases is negligible. In this case, the pressure drop is a function of only the shear stress at the enclosing surfaces. Hanratty and Engen[22] studied the interaction of a turbulent air stream flowing over a horizontal water film in a region in which the momentum of the flow did not change. They showed that by measuring the pressure drop, the location of the velocity maximum in the air by a pitot traverse, and the film thickness, the interfacial shear stress could be calculated from a simple force balance.

The effect of waves on the gas phase can be imagined as being similar to that of a roughened solid surface. Lilleleht and Hanratty[33] used the method of Nikuradse[41] to establish a correlation for the interfacial friction factor. They measured the interfacial friction factor in the manner proposed by Hanratty and Engen and tried to find a relationship between the "equivalent sand roughness" of Nikuradse and the measured root-mean-square displacement of the film from its average height. An order-of-magnitude agreement was achieved. Cohen,[9] using the same experimental facility as Lilleleht, found that when the interfacial waves at the interface between a turbulent air stream and a horizontal liquid film were three-dimensional, the interface friction factor was essentially independent of the air velocity and could be correlated with a dimensionless, root-mean-square wave-height parameter.

Interface friction factors have also been determined for the annular flow of air and water in vertical tubes. Generally, the interfacial shear stress was evaluated by measuring the pressure drop over a length of tube and then applying a momentum balance written for the flow. For example, Shearer and Nedderman[42] measured the pressure drop for the annular flow of air and various liquids, where the phase interface was covered with small ripples. The force balance they used to calculate the interfacial friction factor assumed that the momentum change of the flow was negligible. Using the measured pressure drop and an analytically determined film thickness, they calculated the interfacial friction factors. Relating the interface friction factor to the equivalent sand roughness of Nikuradse, they proposed a correlation for the equivalent sand roughness and various parameters of the flow.

The interface shear stress plays an important role in determining the behavior of a film flowing in the presence of a gas. However, the wall shear stress in the film is equally important. Because the amplitude of the interfacial disturbances is usually of the same order of magnitude as the mean liquid film thickness,[4] obtaining direct measurements of the wall shear stress is very difficult.

In lieu of a measurement of the wall shear stress in the film, it has been evaluated through relationships developed from the concept of the "wall-layer model" of film flow. Carpenter and Colburn[7] first suggested this concept when they assumed that a liquid film flowing under the influence of a high-velocity turbulent gas stream behaves as the wall layer of a single-phase liquid flow with the same thickness and wall shear stress. The wall-layer model uses a single-phase velocity profile to establish an expression for the wall shear stress. Various single-phase velocity profiles have been used with varying degrees of success. For example, Dukler and Bergelin[14] used the von Karman[49] universal velocity distribution in studying the flow of films over vertical surfaces. Where no interfacial shear existed, the agreement between measured film thicknesses and those calculated was quite close. Anderson and Mantzouranis[4] used the von Karman velocity profile in their study of annular flow in a vertical tube. Predictions of the liquid film thickness were accurate to ±15%. In another analysis of film flow, Dukler[15] used the expression proposed by Deissler[13] for the eddy viscosity near the solid boundary. The thickness of a liquid film flowing concurrently with a gas was predicted theoretically. In a succeeding paper, Dukler[16] compared the aforementioned results with data and found good agreement for both the case of zero and finite interfacial shear stress. For the horizontal flow of turbulent air over liquid films, Hershman[24] compared the predictions of film thickness evaluated by using Deissler's results in the wall-layer model to measured film thicknesses. He concluded that the wall-layer model is a valid description of a liquid film when the surface is disturbed by waves. Using the same experimental facility as Hershman, Cohen[9] found that, by assuming a constant velocity in the film from the interface up to a distance near the wall, and then a linear variation in velocity until the wall is reached, a one-parameter model resulted which could be chosen to fit the data of measured film thicknesses.

It is very difficult to predict the behavior of a film under the influence of a concurrent gas phase when momentum changes in the flow are important and when the phase interface is covered by waves. Wallis[50] discussed various methods of attacking this problem. The usual procedure is (1) to circumvent considering the interfacial disturbances by assuming that the interface is smooth, and (2) to introduce appropriate correlations for the interface and wall shear stresses and the static pressure gradient which account for the effects of the waves. Just as there are various models for describing the shear stresses, there are a number of correlations for the pressure gradient. A notable example is the Lockhart and Martinelli[34] correlation, which was derived to enable predictions to be made of the frictional pressure drop in horizontal annular or stratified flow. This correlation has also been applied with some success to other pipe orientations and flow regimes.

Increase of the gas velocity eventually causes liquid droplets to be torn from the film and carried along in the gas phase. Since this flow

condition is excluded from consideration in this report, results from studies concerning the onset of this flow regime are cited. Entrainment for air flowing concurrently over water, aqueous solutions, and oils in horizontal flow has been investigated experimentally by Van Rossum.[48] The onset of entrainment was determined by visual observation. For water, the critical velocity occurred at 59 ft/sec. Wallis[50] visually determined, in a flow geometry similar to Van Rossum's, the onset velocity for entrainment for the flow of air over water and glycerine. He reported a critical velocity range of 53-58 ft/sec for the flow of air over water. Hanratty and Woodmanse[23] have given a physical explanation of entrainment. They stated that atomization occurs by the suction of drops from the crests of waves and by the eruption of rafts of bubbles from the crests of roll waves.

2. Condensing One-component Concurrent Stratified Flow

Extensive reviews of the literature on condensing heat transfer have been compiled in Refs. 3 and 51. Only the results of research pertaining to the condensation on films moving under the influence of saturated vapors are reviewed here.

In his classic work on film condensation, Nusselt[39] extended his analysis of film condensation on a vertical surface with no vapor motion to include laminar film condensation inside a vertical tube with vapor motion. He assumed that the liquid-vapor interfacial shear stress was proportional to the frictional pressure drop for pipe flow containing the vapor alone. This presumed that the condensate film was small enough to render the vapor velocity constant. In this analysis, the mass balance between the condensate and vapor flow is not satisfied. Jacob, Erk, and Eck[29] extended the analysis to correct the mass balance, but retained the simplified model of liquid-vapor shear stress.

Many of the early experiments on film condensation produced data that yielded heat-transfer coefficients higher than that calculated from the Nusselt theory. Kirkbride[32] summarized some of these data. This variance between experiment and theory prompted modifications to the Nusselt theory in the form of relaxation of one or more of Nusselt's assumptions.

Since the data were higher than predicted, it was speculated that perhaps the film was turbulent rather than laminar. Turbulent film condensation was considered first by Colburn.[10] He presumed that the film became turbulent at a film Reynolds number of 400. His semitheoretical relationship for heat-transfer coefficients still yielded heat-transfer coefficients lower than those observed experimentally for condensing, though closer than the Nusselt prediction. Colburn concluded that lower "transition"

Reynolds number and thinning of the film due to liquid-vapor interfacial shear stress may be the reasons for the continued discrepancies. Later, Carpenter and Colburn[7] studied the effects of mass transfer and shear stress at the liquid-vapor interface on film condensation inside a vertical tube. The correlation of Bergelin et al.[5] was used to evaluate the shear stress at the liquid-vapor interface. This correlation was developed for two-component flow. They assumed the film to be turbulent and used the concept of the wall-layer model mentioned earlier in this chapter. They further assumed that the significant resistance to heat flow was due to the viscous sublayer of the condensate. The momentum transferred to the film by condensation was taken to be equal to the product of the vapor velocity and the condensation rate. Their heat-transfer coefficients varied directly with the average mass velocity of the vapor. These predictions showed the right trend when compared with the data of Carpenter.[8]

A further refinement was reported by Rohsenow, Webber, and Ling,[40] who attempted to account for the heat-transfer resistance of the entire film. Using the concept of the wall-layer model, they assumed that the velocity distribution in the film was that of von Karman.[49] They also considered the effect of subcooling in the film and shear stress at the liquid-vapor interface. They developed a "transition" Reynolds number, which is a function of interfacial shear. Evaluation of the heat-transfer coefficient via their model necessitates knowledge of the interfacial shear stress. To calculate the interfacial shear stress, Rohsenow, Webber, and Ling suggest using the correlation of Bergelin et al.[5] As speculated by Colburn, the results show that the interfacial shear increases the heat-transfer coefficient.

In all the aforementioned analyses, convective momentum and energy changes were considered negligible. The preceding theories have enjoyed some success in the prediction of heat-transfer coefficients for condensation inside tubes except for liquid metals. Research in liquid-metal film condensation has isolated this discrepancy in terms of a liquid-vapor interfacial resistance.[46,47]

Akers, Deans, and Crosser[1] studied the effect of vapor velocity, temperature difference, and fluid properties on the heat-transfer coefficient of a vapor condensing in a horizontal tube. Their resulting correlation was within 20% of the data. Meyers and Rosson[37] condensed methanol in horizontal tubes and found that the average heat-transfer coefficients were independent of vapor velocity, but dependent on condensate flowrates. The maximum film Reynolds number in their experiments was less than 500. Altman, Staub, and Norris[2] used the method of Carpenter and Colburn to correlate local heat-transfer data obtained by condensing Freon-22 in horizontal tubes at high vapor velocities. For inlet qualities less than 92%, fair agreement was obtained. For qualities greater than 92%, an empirical

factor was introduced to correlate the data. Soliman, Schuster, and Berenson[45] developed a correlation for the heat-transfer coefficient in the form given by Carpenter and Colburn. Re-evaluating the constants in this correlation, they found that the predictions of this correlation agreed well with the available experimental data over a range of vapor velocities from 20 to 1000 ft/sec and a range of Prandtl numbers from 1 to 10.

Hilding[26] derived differential equations for high-velocity condensation, assuming the flow regime to be annular and one-dimensional. The maximum steam velocity encountered was 1800 ft/sec. To predict the behavior of the flow with axial length, Hilding used the continuity, vapor momentum, and energy equations. To relate the velocities of each phase at the interface, he assumed that the dynamic pressures on either side of the vapor-liquid interface were equal. Dukler,[17] in his written discussion of the paper, questioned the validity of this last assumption and the method used to solve the governing equations. The assumption of annular flow is also in question. Borchmann[6] condensed vapor in annuli and found that approximately 75% of the condensate was entrained by the vapor when the vapor velocity was approximately 110 ft/sec.

B. Scope of the Investigation

The principal objective of this report was to study the effects of interfacial transport processes on the physical behavior of a film in a system where a turbulent gas stream flows parallel to a horizontal turbulent film. In the two-component case, the only interaction considered between the gas and liquid phases was the interface shear stress. In the one-component case, the additional interfacial interaction resulting from condensation of the vapor was also considered.

The survey of the literature on the stratified turbulent flow of one- and two-component fluids revealed the physical complexity of the flow mechanics. To alleviate the necessity of a detailed consideration of the local flow mechanics, assumptions appropriate to simplifying the pertinent equations of change were delineated. An analytical model, consistent with the aforementioned assumptions, was developed to describe the horizontal, stratified, turbulent flow of a gas over a liquid film.

Experiments to confirm the model were performed on air-water and steam-water flows in a horizontal, rectangular test section.

In both the air-water and steam-water experiments, the variation in the mean film thickness with axial length from the entrance of the test section was measured. Information regarding the heights of the crests and troughs of the waves in relation to the mean film thickness were obtained. The flow regimes were observed visually. Other primary

measurements included were the inlet flowrates of the gas and liquid phases and, in the steam-water experiment, the temperature of the film at the wall surface.

Models developed for the interface shear stress for two-component flow have required knowledge of the structure of the interfacial waves. Noting the distinct characteristics of the various wave regimes, the aforementioned models were simplified by investigating correlations for the interface shear stress which only require knowledge of the wave regime and not of the details of the structure. The interface characteristics for the turbulent flow of water films in the presence of a turbulent gas phase are three-dimensional, roll-wave, or entraining. Since entrainment occurs from the roll-waves when the gas velocity increases to the appropriate magnitude, and since this phenomena was excluded from consideration in this research, the three-dimensional wave regime was given principal consideration.

In the condensing heat-transfer literature, the interface shear stress has generally been evaluated from correlations for two-component flow. The applicability of this type of correlation and the possible effect of condensation was investigated.

In previous work on film condensation, the principal resistance to heat transfer in the film was in the region of the film in close proximity to the wall from which cooling was effected. This region of the film is viscous and largely unaffected by the presence of interfacial waves. To investigate the effect of waves on heat transfer in the main portion of the film, condensation was effected by initially subcooling the film. Since the resistance to heat transfer in this case is related to the overall characteristics of the film, previously developed models which emphasize the wall region are not applicable. Thus, a new model, which considers the resistance to be a function of the overall characteristics of the film, was developed.

II. THEORY

In this chapter, analytical models are developed to describe the interaction of two-dimensional, stratified, turbulent, two-phase fluids. Emphasis is placed on the description of flows whereby the gas-phase velocity is at least an order of magnitude larger than the liquid-phase velocity, and the gas-phase momentum is the same order of magnitude as the liquid-phase momentum. Under these circumstances, where the momentum transferred from the gas phase to the liquid phase plays a significant role in the behavior of the liquid, the liquid phase occupies a small portion of the total flow area and is referred to as a film. Since the liquid-gas interface is generally quite disturbed (wavy), one goal of the model development is to provide the capability of describing the actual behavior without knowing the details of the local flow mechanics.

Although the primary intention of the succeeding development is to consider turbulent flow, laminar flow is also of interest. In particular, laminar flow is useful since it avoids consideration of the Reynold stresses when the primary interest is directed at developing the appropriate forms of the governing equations and boundary conditions. As will be shown in the development, the extension of the laminar-flow model to the turbulent-flow model is quite straightforward. Consideration of laminar flow also provides an indication of the possible extension of the results of this chapter to other flow regimes, say turbulent gas and laminar liquid flow.

A. Two-component Flow

In this section, governing equations are derived to describe the two-dimensional, stratified flow of a gas and liquid stream in both the laminar and turbulent flow regimes. The pertinent equations of change for each component are:

Continuity

$$\frac{1}{\rho}\frac{D\rho}{D\theta} = (\nabla \cdot V); \tag{1}$$

Momentum

$$\rho \frac{DV}{D\theta} = -\nabla P - (\nabla \cdot \underline{\tau}) + \rho g; \tag{2}$$

Energy

$$\rho C_v \frac{DT}{D\theta} = \nabla \cdot (k \nabla T) - T\left(\frac{\partial P}{\partial T}\right)_\rho (\nabla \cdot V) + \mu \Phi. \tag{3}$$

Figure 1 shows the coordinate system to be used in this development.

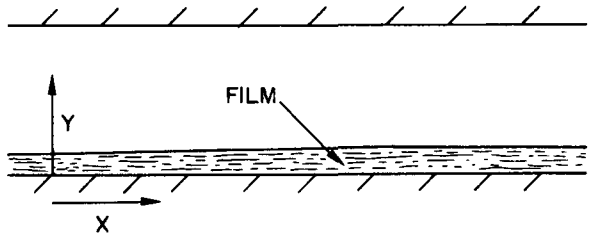

Fig. 1

Coordinate System Used in Developing the Governing Equations

1. Laminar Flow

a. Equations of Motion. The following assumptions delineate the model used in this section:

1. The flow pattern is laminar and two-dimensional.
2. The fluids are incompressible.
3. The transport properties are constant.
4. No temperature gradients exist.
5. The interface between the gas and liquid streams is smooth.
6. The flow is time-indepdendent.
7. No mass transfer occurs between the phases.

From these assumptions, Eqs. 1-3 reduce, for each component, to

$$\frac{\partial u}{\partial x} + \frac{\partial v}{\partial y} = 0; \tag{4}$$

$$u\frac{\partial u}{\partial x} + v\frac{\partial u}{\partial y} = -\frac{1}{\rho}\frac{\partial P}{\partial x} + \frac{\mu}{\rho}\left(\frac{\partial^2 u}{\partial x^2} + \frac{\partial^2 u}{\partial y^2}\right); \tag{5}$$

$$u\frac{\partial v}{\partial x} + v\frac{\partial v}{\partial y} = -\frac{1}{\rho}\frac{\partial P}{\partial y} - g_y + \frac{\mu}{\rho}\left(\frac{\partial^2 v}{\partial x^2} + \frac{\partial^2 v}{\partial y^2}\right). \tag{6}$$

b. Boundary Conditions. The boundary and compatibility conditions that the solutions to Eqs. 4-6 satisfy are noted or derived in this section. At $y = 0$,

$$u_\ell = v_\ell = 0; \tag{7}$$

$$\frac{\partial P_\ell}{\partial x} = \mu_\ell\left(\frac{\partial^2 u_\ell}{\partial y^2}\right); \tag{8}$$

$$\frac{\partial P_\ell}{\partial y} = -\rho_\ell g_y + \mu_\ell\left(\frac{\partial^2 v_\ell}{\partial y^2}\right). \tag{9}$$

at y = b,

$$u_a = v_a = 0; \tag{10}$$

$$\frac{\partial P_a}{\partial x} = \mu_a\left(\frac{\partial^2 u_a}{\partial y^2}\right); \tag{11}$$

$$\frac{\partial P_a}{\partial y} = -\rho_a g_y + \mu_a\left(\frac{\partial^2 v_a}{\partial y^2}\right). \tag{12}$$

At y = t (the interface), the velocity in both phases is the same; i.e., there is no slip. This requirement may be satisfied by requiring that the velocities normal and tangential to the surface of the interface be the same in both phases.

The unit normal and tangential vectors to the interface are

$$n = \frac{-dt/dx}{\left(1+(dt/dx)^2\right)^{1/2}} i + \frac{1}{\left(1+(dt/dx^2\right)^{1/2}} j \tag{13}$$

and

$$t = \frac{1}{\left(1+(dt/dx)^2\right)^{1/2}} i + \frac{dt/dx}{\left(1+(dt/dx)^2\right)^{1/2}} j. \tag{14}$$

The no-slip condition at the interface requires that the velocity vector in each phase at the interface be identical. The tangential and normal components of this vector are

$$V \cdot t = \frac{u}{\left(1+(dt/dx)^2\right)^{1/2}} + \frac{v\, dt/dx}{\left(1+(dt/dx)^2\right)^{1/2}} \tag{15}$$

and

$$V \cdot n = \frac{-u\, dt/dx}{\left(1+(dt/dx)^2\right)^{1/2}} + \frac{v}{\left(1+(dt/dx)^2\right)^{1/2}}. \tag{16}$$

Now, since $(V \cdot t)_\ell = (V \cdot t)_a$ and $(V \cdot n)_\ell = (V \cdot n)_a$, the following identities are written:

$$(V \cdot t)_\ell \frac{dt}{dx} + (V \cdot n)_\ell = (V \cdot t)_a \frac{dt}{dx} + (V \cdot n)_a; \tag{17}$$

$$(V \cdot t)_\ell - (V \cdot n)_\ell \frac{dt}{dx} = (V \cdot t)_a - (V \cdot n)_a \frac{dt}{dx}. \tag{18}$$

Substituting Eqs. 15 and 16 into Eqs. 17 and 18 gives the following results:

$$u_a\Big|_t = u_\ell\Big|_t; \tag{19}$$

$$v_a\Big|_t = v_\ell\Big|_t. \tag{20}$$

For a two-component flow with no mass transfer, we have, from continuity considerations, $V \cdot n = 0$. From Eq. 16, the following result is obtained:

$$\frac{dt}{dx} = \frac{v\big|_t}{u\big|_t}. \tag{21}$$

The force at the interface, neglecting surface tension, is (see, for example, Lodge[35])

$$Pn + (\underline{\tau} \cdot n) = \sum_i P n_i + \sum_i e_i \sum_j \tau_{ij} n_j \tag{22}$$

$$= \left\{ i \left(\frac{-\sigma_{xx}\, dt/dx}{[1 + (dt/dx)^2]^{1/2}} + \frac{\tau_{xy}}{[1 + (dt/dx)^2]^{1/2}} \right) \right\}$$

$$+ \left\{ j \left(\frac{-\tau_{yx}\, dt/dx}{[1 + (dt/dx)^2]^{1/2}} + \frac{\sigma_{yy}}{[1 + (dt/dx)^2]^{1/2}} \right) \right\}, \tag{23}$$

where

$$\sigma_{xx} = P - 2\mu \left.\frac{\partial u}{\partial x}\right|_t, \tag{24}$$

$$\sigma_{yy} = P - 2\mu \left.\frac{\partial v}{\partial y}\right|_t, \tag{25}$$

and

$$\tau_{xy} = \tau_{yx} = -\mu \left(\left.\frac{\partial u}{\partial y}\right|_t + \left.\frac{\partial v}{\partial x}\right|_t \right). \tag{26}$$

Equating the forces in the x and y directions in each phase gives

$$\left(\sigma_{xx_\ell} - \sigma_{xx_a}\right)\Big|_t \frac{dt}{dx} - \left(\tau_{xy_\ell} - \tau_{xy_a}\right)\Big|_t = 0, \tag{27}$$

and

$$\left(\sigma_{yy_\ell} - \sigma_{yy_a}\right)\Big|_t - \left(\tau_{xy_\ell} - \tau_{xy_a}\right)\Big|_t \frac{dt}{dx} = 0. \tag{28}$$

Substituting Eqs. 24-26 into Eqs. 27 and 28 yields

$$\left\{-P_\ell\Big|_t + 2\mu_\ell \frac{\partial u_\ell}{\partial x}\Big|_t + P_a\Big|_t - 2\mu_a \frac{\partial u_a}{\partial x}\Big|_t\right\}\frac{dt}{dx}$$

$$- \left\{\mu_\ell \frac{\partial u_\ell}{\partial y}\Big|_t + \mu_\ell \frac{\partial v_\ell}{\partial x}\Big|_t - \mu_a \frac{\partial u_a}{\partial y}\Big|_t - \mu_a \frac{\partial v_a}{\partial x}\Big|_t\right\} = 0, \tag{29}$$

and

$$\left\{-P_\ell\Big|_t + 2\mu_\ell \frac{\partial v_\ell}{\partial y}\Big|_t + P_a\Big|_t - 2\mu_a \frac{\partial v_a}{\partial y}\Big|_t\right\}$$

$$- \left\{\mu_\ell \frac{\partial u_\ell}{\partial y}\Big|_t + \mu_\ell \frac{\partial v_\ell}{\partial x}\Big|_t - \mu_a \frac{\partial u_a}{\partial y}\Big|_t - \mu_a \frac{\partial v_a}{\partial x}\Big|_t\right\}\frac{dt}{dx} = 0. \tag{30}$$

Adding and subtracting Eqs. 29 and 30 gives

$$\mu_\ell \left\{\frac{\partial u_\ell}{\partial y}\Big|_t + \frac{\partial v_\ell}{\partial x}\Big|_t\right\} - \mu_a \left\{\frac{\partial u_a}{\partial y}\Big|_t + \frac{\partial v_a}{\partial x}\Big|_t\right\} = 0, \tag{31}$$

and

$$\left\{P_a\Big|_t - P_\ell\Big|_t\right\} + \left\{2\mu_\ell \frac{\partial u_\ell}{\partial x}\Big|_t - 2\mu_a \frac{\partial u_a}{\partial x}\Big|_t\right\}\left\{\frac{(dt/dx)^2 + 1}{(dt/dx)^2 - 1}\right\} = 0. \tag{32}$$

Equations 4-6 and the associated boundary conditions are difficult to solve, even numerically. However, a contraction of the aforementioned system of equations and boundary conditions to a system of equations similar to the boundary-layer equations can be accomplished by an order-of-magnitude analysis similar to that conventionally used (e.g., see Schlichting[41]).

c. Development of Boundary-layer-type Equations. When the film is thin with respect to the channel spacing, and when the gas velocity is an order of magnitude larger than the film velocity, the rate of change of film thickness with respect to axial length, dt/dx, is small. Qualitatively, this means that the gas can transfer an amount of momentum to the film that is approximately equal to the momentum loss from the film to the wall. In light of the preceding, it is assumed that $dt/dx \ll 1$. Equation 21 then implies that $v|_t \ll u|_t$. To examine the extent to which the assumption that $dt/dx \ll 1$ can simplify Eqs. 4-6, these equations, as applied to the film, are made dimensionless, and the magnitudes of the various terms are estimated.

The following dimensionless variables are defined:

$$\frac{u_\ell}{\bar{u}_{\ell_0}} = \hat{u}_\ell, \quad \frac{v_\ell}{\bar{u}_{\ell_0}} = \hat{v}_\ell, \quad \frac{P_\ell}{\rho_\ell \bar{u}_{\ell_0}^2} = \hat{P}_\ell, \quad \frac{x}{L} = \hat{x}, \quad \frac{y}{L} = \hat{y}.$$

The length, L, is a characteristic axial length. The characteristic velocity, $\bar{u}_{\ell_0}$, is chosen as the mass average velocity at $x = 0$. This choice is dictated by the fact that the average velocity in the film varies with axial length in inverse proportion to the mean film thickness. However, since it has been assumed that dt/dx is small, the difference between the average velocity at $x = 0$ and elsewhere in the film should also be small. This follows from continuity considerations, since the mass flowrate per unit width, W_ℓ, remains constant. That is,

$$W_\ell = \int_0^t \rho_\ell u_\ell dy \equiv \rho_\ell \bar{u}_\ell t = \text{constant}. \tag{33}$$

Substituting the dimensionless variables into Eqs. 4-6 gives

$$\frac{\partial \hat{u}_\ell}{\partial \hat{x}} + \frac{\partial \hat{v}_\ell}{\partial \hat{y}} = 0, \tag{34}$$

$$\hat{u}_\ell \frac{\partial \hat{u}_\ell}{\partial \hat{x}} + \hat{v}_\ell \frac{\partial \hat{v}_\ell}{\partial \hat{y}} = - \frac{\partial \hat{P}_\ell}{\partial \hat{x}} + \frac{\nu_\ell}{\bar{u}_{\ell_0} L} \left\{ \frac{\partial^2 \hat{u}_\ell}{\partial \hat{x}^2} + \frac{\partial^2 \hat{u}_\ell}{\partial \hat{y}^2} \right\}, \tag{35}$$

and

$$\hat{u}_\ell \frac{\partial \hat{v}_\ell}{\partial \hat{x}} + \hat{v}_\ell \frac{\partial \hat{v}_\ell}{\partial \hat{y}} = - \frac{\partial \hat{P}_\ell}{\partial \hat{y}} - \frac{g_y L}{\bar{u}_{\ell_0}^2} + \frac{\nu_\ell}{\bar{u}_{\ell_0} L} \left\{ \frac{\partial^2 \hat{v}_\ell}{\partial \hat{x}^2} + \frac{\partial^2 \hat{v}_\ell}{\partial \hat{y}^2} \right\}. \tag{36}$$

The dimensionless parameters in these equations are a Reynolds number, $\bar{u}_{\ell_0} L/\nu_\ell$, and a Froude number, $\bar{u}_{\ell_0}^2/g_y L$.

The characteristic length, L, is assumed to be chosen so that

$$\frac{\partial \hat{u}_\ell}{\partial \hat{x}} = O(1),$$

where the O notation means "approximate magnitude of" and does not infer a bound in a limiting process. From Eq. 34, it can be concluded that

$$\frac{\partial \hat{v}_\ell}{\partial \hat{y}} = O(1).$$

Since

$$\hat{v}_\ell\big|_t = \hat{u}_\ell\big|_t \frac{d\hat{t}}{d\hat{x}}$$

and

$$\hat{u}_\ell = O(1),$$

it follows that

$$\frac{\partial \hat{u}_\ell}{\partial \hat{y}} = O\left(\frac{1}{d\hat{t}/d\hat{x}}\right).$$

Thus, the orders of magnitude of the various terms in Eqs. 34 and 35 are

$$\frac{\partial \hat{u}_\ell}{\partial \hat{x}} + \frac{\partial \hat{v}_\ell}{\partial \hat{y}} = 0,$$

$$\downarrow \qquad \downarrow$$

$$1 \qquad \frac{d\hat{t}/d\hat{x}}{d\hat{t}/d\hat{x}},$$

$$\hat{u}_\ell \frac{\partial \hat{u}_\ell}{\partial \hat{x}} + v_\ell \frac{\partial \hat{u}_\ell}{\partial \hat{y}} = -\frac{\partial \hat{P}_\ell}{\partial \hat{x}} + \frac{\nu_\ell}{\bar{u}_{\ell_0} L}\left\{\frac{\partial^2 \hat{u}_\ell}{\partial \hat{x}^2} + \frac{\partial^2 \hat{u}_\ell}{\partial \hat{y}^2}\right\},$$

$$\downarrow \quad \downarrow \quad \downarrow \quad \downarrow \qquad\qquad\qquad \downarrow \quad \downarrow$$

$$1 \cdot 1 \quad \frac{d\hat{t}}{d\hat{x}} \cdot \frac{1}{d\hat{t}/d\hat{x}} \qquad\qquad\qquad 1 \quad \frac{1}{(d\hat{t}/d\hat{x})^2}$$

Therefore, for the viscous terms to be of the same order of magnitude as the momentum terms (a necessity if the order of the differential equation is to be preserved), the order of magnitude of the Reynolds number must be

$$\frac{\bar{u}_{\ell_0} L}{\nu_\ell} = O\left\{\frac{1}{(dt/dx)^2}\right\}.$$

It can also be concluded that $\partial^2 \hat{u}_\ell / \partial \hat{x}^2$ can be neglected in favor of $\partial^2 \hat{u}_\ell / \partial \hat{y}^2$.

The orders of magnitude of the various terms in Eq. 36 are

$$\hat{u}_\ell \frac{\partial \hat{v}_\ell}{\partial \hat{x}} + \hat{v}_\ell \frac{\partial \hat{v}_\ell}{\partial \hat{y}} = - \frac{\partial \hat{P}_\ell}{\partial \hat{y}} - \frac{g_y L}{\bar{u}^2_{\ell_0}} + \frac{\nu_\ell}{\bar{u}_{\ell_0} L}\left\{\frac{\partial^2 \hat{v}_\ell}{\partial \hat{x}^2} + \frac{\partial^2 \hat{v}_\ell}{\partial \hat{y}^2}\right\}$$

$$\downarrow \quad \downarrow \quad \downarrow \quad \downarrow \qquad\qquad\qquad \downarrow \quad \downarrow \quad \downarrow$$

$$1 \cdot \frac{d\hat{t}}{d\hat{x}} \quad \frac{d\hat{t}}{d\hat{x}} \cdot 1 \qquad\qquad\qquad \left(\frac{d\hat{t}}{d\hat{x}}\right)^2 \quad \frac{d\hat{t}}{d\hat{x}} \quad \frac{1}{\frac{d\hat{t}}{d\hat{x}}}.$$

Since all terms in the above equation are of $O(d\hat{t}/d\hat{x})$,

$$- \frac{\partial \hat{P}_\ell}{\partial \hat{y}} - \frac{g_y L}{\bar{u}^2_{\ell_0}} = O\left(\frac{dt}{dx}\right) \simeq 0. \tag{37}$$

Equation 37 can be integrated to give

$$\hat{P}_\ell = \frac{g_y L}{\bar{u}^2_{\ell_0}}\left[y + f(x)\right].$$

The constant of integration can be determined as follows: At $\hat{y} = \hat{t}$,

$$\hat{P}_\ell = \hat{P}_\ell \Big|_t;$$

$$\therefore \hat{P}_\ell = \frac{g_y L}{\bar{u}^2_{\ell_0}}(\hat{t} - \hat{y}) + \hat{P}_\ell \Big|_t. \tag{38}$$

If Eq. 38 is differentiated with respect to x, the axial variation of pressure in the liquid film becomes

$$\frac{\partial \hat{P}_\ell}{\partial \hat{x}} = \frac{g_y L}{\bar{u}^2_{\ell_0}}\left(\frac{d\hat{t}}{d\hat{x}}\right) + \frac{d\left(\hat{P}_\ell\big|_t\right)}{d\hat{x}}. \tag{39}$$

Summing up, the pertinent equations in the liquid film can be written

$$\frac{\partial \hat{u}_\ell}{\partial \hat{x}} + \frac{\partial \hat{v}_\ell}{\partial \hat{y}} = 0, \tag{40}$$

and

$$\hat{u}_\ell \frac{\partial \hat{u}_\ell}{\partial \hat{x}} + \hat{v}_\ell \frac{\partial \hat{u}_\ell}{\partial \hat{y}} = -\frac{d\left(\hat{P}_\ell\big|_t\right)}{d\hat{x}} - \frac{g_y L}{\bar{u}^2_{\ell_0}} \frac{d\hat{t}}{d\hat{x}} + \frac{\nu_\ell}{\bar{u}_{\ell_0} L} \frac{\partial^2 \hat{u}_\ell}{\partial \hat{y}^2}. \tag{41}$$

The boundary-layer-type equations derived here differ from the normal equations in that a body-force term proportional to $d\hat{t}/d\hat{x}$ is included. This body force is normally neglected in single-phase boundary-layer equations where the pressure is taken to be equal to the difference between the pressure during motion and at rest. Since a free surface is present in this situation, the effect of the body force term is not, a priori, negligible. The significance of the body-force term is manifested in the modified Froude number,

$$Fr = \frac{\bar{u}^2_{\ell_0}}{g_y L \frac{d\hat{t}}{d\hat{x}}}.$$

Physically, Eqs. 40 and 41 are realistic. At large values of x, $d\hat{t}/d\hat{x}$ approaches zero. This represents the case of fully developed stratified flow for which $u_\ell = u_\ell(y)$ and $v_\ell = 0$. For fully developed stratified flow, the governing equations in the film are

$$\frac{\partial \hat{u}_\ell}{\partial \hat{x}} = 0, \tag{42}$$

and

$$0 = -\frac{d\hat{P}_\ell}{d\hat{x}} + \frac{\nu_\ell}{\bar{u}_{\ell_0} L} \frac{d^2 \hat{u}_\ell}{d\hat{y}^2}. \tag{43}$$

Now, for $dt/dx \neq 0$ but $<< 1$, it is physically reasonable that the momentum changes in the film in the axial direction are much more important than those in the y direction. Thus, the choice of the boundary-layer-type equations as

the governing equations in the liquid film is indicated. Since equations of the form of Eqs. 42 and 43 apply to the gas phase at large $\hat{x}$, it is physically reasonable that the aforementioned arguments regarding the boundary-layer-type equations apply not only to the film, but also to the gas phase. Since the density ratio of liquid and gas phases under consideration is O(1000), the body-force term is significant only in the film momentum equation, implying that the static pressure in the gas phase is constant over the y coordinate. In light of the foregoing, the pertinent boundary-layer-type equations in the gas phase are

$$\frac{\partial \hat{u}_a}{\partial \hat{x}} + \frac{\partial \hat{v}_a}{\partial \hat{y}} = 0, \tag{44}$$

$$\hat{u}_a \frac{\partial \hat{u}_a}{\partial \hat{x}} + \hat{v}_a \frac{\partial \hat{u}_a}{\partial \hat{y}} = - \frac{d\hat{P}_a}{d\hat{x}} + \frac{\nu_a}{\bar{u}_{a_0} L} \frac{\partial^2 \hat{u}_a}{\partial \hat{y}^2}, \tag{45}$$

and

$$\frac{\partial \hat{P}_a}{\partial \hat{y}} = 0, \tag{46}$$

where $\bar{u}_{a_0}$ for the gas phase refers to the average gas velocity at x = 0. All other normalizing parameters remain the same.

Considering the boundary conditions, only Eqs. 31 and 32 are subject to simplification. For example, in Eq. 31,

$$\frac{\partial \hat{u}}{\partial \hat{y}} = O\left(\frac{1}{\frac{d\hat{t}}{d\hat{x}}}\right) \text{ and } \frac{\partial \hat{v}}{\partial \hat{x}} = O\left(\frac{d\hat{t}}{d\hat{x}}\right).$$

Therefore,

$$\mu_\ell \left.\frac{\partial u_\ell}{\partial y}\right|_t = \mu_a \left.\frac{\partial u_a}{\partial y}\right|_t. \tag{47}$$

In Eq. 32, noting that $d\hat{t}/d\hat{x} << 1$, the dimensionless form of the liquid terms is

$$\hat{P}_\ell - \frac{2\nu_\ell}{\bar{u}_{\ell_0} L} \frac{\partial \hat{u}_\ell}{\partial \hat{x}}.$$

Now, since $\hat{P}_\ell = O(1)$,

$$\partial \hat{u}_\ell / \partial \hat{x} = O(1),$$

and

$$\nu_\ell / \bar{u}_{\ell_0} L = O\left[\left(\frac{d\hat{t}}{d\hat{x}}\right)^2\right],$$

the second term is negligible in comparison with the first. Therefore, Eq. 32 reduces to

$$P_\ell \big|_t = P_a \big|_t. \tag{48}$$

Since $P_a = f(x)$, Eq. 39 in dimensional form becomes

$$\frac{\partial P_\ell}{\partial x} = \rho_\ell g_y \frac{dt}{dx} + \frac{dP_a}{dx}. \tag{49}$$

In summary, the governing equations and boundary conditions for each phase are as follows:

The liquid film

$$\frac{\partial u_\ell}{\partial x} + \frac{\partial v_\ell}{\partial y} = 0; \tag{50}$$

$$u_\ell \frac{\partial u_\ell}{\partial x} + v_\ell \frac{\partial u_\ell}{\partial y} = -\frac{1}{\rho_\ell} \frac{dP_a}{dx} - g_y \frac{dt}{dx} + \nu_\ell \frac{\partial^2 u_\ell}{\partial y^2}. \tag{51}$$

The gas phase

$$\frac{\partial u_a}{\partial x} + \frac{\partial v_a}{\partial y} = 0; \tag{52}$$

$$u_a \frac{\partial u_a}{\partial x} + v_a \frac{\partial u_a}{\partial y} = -\frac{1}{\rho_a} \frac{dP_a}{\partial x} + \nu_a \frac{\partial^2 u_a}{\partial y^2}. \tag{53}$$

The boundary conditions

$$y = 0; \quad u_\ell = 0, \quad v_\ell = 0; \tag{54}$$

$$y = b; \quad u_a = 0, \quad v_a = 0; \tag{55}$$

$$y = t; \quad u_\ell = u_a, \quad v_\ell = v_a; \tag{56}$$

$$P_\ell = P_a; \tag{57}$$

$$\mu_\ell \frac{\partial u_\ell}{\partial y} = \mu_a \frac{\partial u_a}{\partial y}. \tag{58}$$

d. Fully Developed Stratified Flow. The fully developed flow pattern is, by definition, the asymptotic flow pattern, i.e., the case for which $dt/dx = 0$ and $u = u(y)$. For this case, the governing equations and boundary conditions reduce to the following:

The liquid film

$$\frac{dP_a}{dx} = \mu_\ell \frac{d^2 u_\ell}{dy^2}. \tag{59}$$

The gas phase

$$\frac{dP_a}{dx} = \mu_a \frac{d^2 u_a}{dy^2}. \tag{60}$$

The boundary conditions

$$y = 0; \quad u_\ell = 0; \tag{61}$$

$$y = b; \quad u_a = 0; \tag{62}$$

$$y = t; \quad u_\ell = u_a; \tag{63}$$

$$\mu_\ell \frac{du_\ell}{dy} = \mu_a \frac{du_a}{dy}. \tag{64}$$

Solutions of Eqs. 59 and 60 are

$$u_\ell = \frac{1}{2\mu_\ell} \frac{dP_a}{dx} y^2 + a_1 y, \text{ and } u_a = \frac{1}{2\mu_a} \frac{dP_a}{dx} (y^2 - b^2) + a_2 (y - b).$$

The equations above satisfy the boundary conditions at $y = 0$ and $y = b$. The constants of integration, a_1 and a_2, can be found from the boundary conditions at $y = t$.

$$\frac{1}{2\mu_\ell} \frac{dP_a}{dx} t^2 + a_1 t = \frac{1}{2\mu_a} \frac{dP_a}{dx} (t^2 - b^2) + a_2 (t - b); \; t \frac{dP_a}{dx} + \mu_\ell a_1 = t \frac{dP_a}{dx} + \mu_a a_2.$$

Solving for a_1 and a_2 gives the complete solution,

$$u_\ell = \frac{1}{2\mu_\ell} \frac{dP_a}{dx}(y^2 - \gamma y), \tag{65}$$

and

$$u_a = \frac{1}{2\mu_a} \frac{dP_a}{dx}\left[(y^2 - b^2) - \gamma(y - b)\right], \tag{66}$$

where

$$\gamma \equiv \frac{b^2 - t^2(1 - \epsilon)}{b - t(1 - \epsilon)} \tag{67}$$

and

$$\epsilon = \frac{\mu_a}{\mu_\ell}. \tag{68}$$

The fully developed film thickness and pressure gradient can be determined from Eqs. 65 and 66 by continuity considerations. The continuity equations for the liquid and gas phases are

$$W_\ell = \int_0^t \rho_\ell u_\ell \, dy, \tag{69}$$

and

$$W_a = \int_t^b \rho_a u_a \, dy. \tag{70}$$

Substituting Eqs. 65 and 66 into Eqs. 69 and 70 and integrating, we obtain

$$\frac{2W_\ell \mu_\ell}{\rho_\ell} = \frac{dP_a}{dx}\left\{\frac{t^3}{3} - \frac{\gamma t^2}{2}\right\}, \tag{71}$$

and

$$\frac{2W_a \mu_a}{\rho_a} = \frac{dP_a}{dx}\left\{-\frac{t^3}{3} - \frac{2}{3}b^3 + \frac{\gamma b^2}{2} + \frac{\gamma t^2}{2} - \gamma bt + b^2 t\right\}. \tag{72}$$

Dividing Eqs. 71 and 72 and simplifying result in the following quartic equation for the film thickness:

$$\frac{1-\epsilon}{b^4}\left(1+\epsilon\frac{W_a}{W_\ell}\right)t^4+\frac{2}{b^3}\left\{1+3\epsilon(1-\epsilon)+\frac{\epsilon W_a}{W_\ell}\right\}t^3$$

$$+\frac{3}{b^2}\left\{3(1-\epsilon)-1-\epsilon\frac{W_a}{W_\ell}\right\}t^2+\frac{4}{b}(1-\epsilon)\,t-1=0. \qquad (73)$$

The pressure gradient can be determined by substituting the solution of Eq. 73 into Eqs. 71 or 72.

e. Momentum Integral Equations. For $dt/dx \neq 0$, the pertinent system of governing equations is Eqs. 50-53. These highly nonlinear partial differential equations are coupled through boundary conditions expressed by Eqs. 54-58. Since the flow is bounded by two confining surfaces, an analytical solution to these equations is not possible. Thus, an approximate method is proposed.

A well-known method used in solving the boundary-layer-type equations is the momentum-integral technique. In this technique, the governing equations are integrated over the coordinate normal to the flow, in this case, the y coordinate. If this method is applied to the liquid film, Eqs. 50 and 51 are integrated from y = 0 to y = t as follows:

$$v_\ell\Big|_t = -\int_0^t \frac{\partial u_\ell}{\partial x}\,dy;$$

$$\therefore \frac{1}{2}\int_0^t \frac{\partial (u_\ell)^2}{\partial x}\,dy+\int_0^t v_\ell\frac{\partial u_\ell}{\partial y}\,dy =$$

$$-\frac{1}{\rho_\ell}\int_0^t \frac{dP_a}{dx}\,dy-\int_0^t g_y\frac{dt}{dx}\,dy+\nu_\ell\int_0^t \frac{\partial^2 u_\ell}{\partial y^2}\,dy.$$

Integrating by parts results in

$$\int_0^t v_\ell\frac{\partial u_\ell}{\partial y}\,dy=\int_0^t \frac{\partial(u_\ell v_\ell)}{\partial y}\,dy-\int_0^t u_\ell\frac{\partial v_\ell}{\partial y}$$

$$=(u_\ell v_\ell)\Big|_t-(u_\ell v_\ell)\Big|_0+\int_0^t u_\ell\frac{\partial u_\ell}{\partial x}\,dy.$$

Substituting this result into the integrated momentum equation gives

$$\int_0^t \frac{\partial (u_\ell)^2}{\partial x}\, dy + u_\ell\big|_t v_\ell\big|_t = -\frac{t}{\rho_\ell}\frac{dP_a}{dx} - g_y t\frac{dt}{dx} + \nu_\ell\left\{\frac{\partial u_\ell}{\partial y}\bigg|_t - \frac{\partial u_\ell}{\partial y}\bigg|_0\right\}.$$

With the substitution of the integrated continuity equation into the above equation and with application of the Liebnitz rule to the left-hand side of the above, the momentum integral equation becomes

$$\frac{d}{dx}\int_0^t u_\ell^2 dy - u_\ell\big|_t \frac{d}{dx}\int_0^t u_\ell dy = -\frac{t}{\rho_\ell}\frac{dP_a}{dx} - g_y t\frac{dt}{dx} + \nu_\ell\left\{\frac{\partial u_\ell}{\partial y}\bigg|_t - \frac{\partial u_\ell}{\partial y}\bigg|_0\right\}. \tag{74}$$

The gas-phase momentum integral equation is derived from Eqs. 52 and 53 in a similar manner to give

$$\frac{d}{dx}\int_t^b u_a^2 dy - u_a\big|_t \frac{d}{dx}\int_t^b u_a dy = -\frac{b-t}{\rho_a}\frac{dP_a}{dx} + \nu_a\left\{\frac{\partial u_a}{\partial y}\bigg|_b - \frac{\partial u_a}{\partial y}\bigg|_t\right\}. \tag{75}$$

For a two-component system, continuity considerations require that since

$$W_\ell = \int_0^t \rho_\ell u_\ell dy = \text{constant}, \tag{69}$$

and

$$W_a = \int_t^b \rho_a u_a dy = \text{constant}, \tag{70}$$

therefore

$$\frac{d}{dx}\int_0^t u_\ell dy = 0,$$

and

$$\frac{d}{dx}\int_t^b u_a dy = 0.$$

Thus, the momentum integral equations for the two-component system are, finally,

$$\frac{d}{dx}\int_0^t u_\ell^2 dy = -\frac{t}{\rho_\ell}\frac{dP_a}{dx} - g_y t\frac{dt}{dx} + \nu_\ell\left\{\left.\frac{\partial u_\ell}{\partial y}\right|_t - \left.\frac{\partial u_\ell}{\partial y}\right|_0\right\}, \tag{76}$$

and

$$\frac{d}{dx}\int_t^b u_a^2 dy = -\frac{b-t}{\rho_a}\frac{dP_a}{dx} + \nu_a\left\{\left.\frac{\partial u_a}{\partial y}\right|_b - \left.\frac{\partial u_a}{\partial y}\right|_t\right\}. \tag{77}$$

The associated boundary conditions reduce to

$$y = 0; \quad u_\ell = 0; \tag{78}$$

$$y = b; \quad u_a = 0; \tag{79}$$

$$y = t; \quad u_\ell = u_a; \tag{80}$$

$$\mu_\ell\frac{\partial u_\ell}{\partial y} = \mu_a\frac{\partial u_a}{\partial y}. \tag{81}$$

f. Velocity Profiles in the Gas and Liquid Phases. The approximate method of solving the integrated boundary-layer equations has been credited to von Karman and Pohlhausen. In this method, plausible assumptions are made about the velocity distribution in the boundary layer, abandoning any attempt to satisfy the boundary-layer equations for every fluid particle. The form of the velocity distribution is usually chosen to be a polynomial of degree N, as follows

$$u(x,y) = \sum_{n=0}^{N} c_n(x)y^n. \tag{82}$$

The coefficients, $c_n(x)$, are evaluated by requiring that the assumed velocity distribution satisfy the same boundary conditions as the exact solution. In addition, the presence of a pressure gradient requires that the assumed distribution must allow for a point of inflection for a positive pressure

gradient and for no point of inflection for a negative pressure gradient. The boundary and compatibility conditions that manifest these requirements are

$$y = 0; \quad u_\ell = 0; \tag{78}$$

$$\frac{dP_a}{dx} = -\rho_\ell g_y \frac{dt}{dx} + \mu_\ell \frac{\partial^2 u_\ell}{\partial y^2}; \tag{83}$$

$$y = t; \quad u_\ell = u_a; \tag{80}$$

$$\mu_\ell \frac{\partial u_\ell}{\partial y} = \mu_a \frac{\partial u_a}{\partial y}; \tag{81}$$

$$y = b; \quad u_a = 0; \tag{79}$$

$$\frac{dP_a}{dx} = \mu_a \frac{\partial^2 u_a}{\partial y^2}. \tag{84}$$

Since the mass flowrate of the gas and liquid phases remains constant, the velocity profiles must also satisfy the integrated continuity equations,

$$W_\ell = \int_0^t \rho_\ell u_\ell \, dy, \tag{69}$$

and

$$W_a = \int_t^b \rho_a u_a \, dy. \tag{70}$$

Keeping in mind the preceding requirements, the following cubic polynomials are chosen for the velocity distributions in the liquid and gas phases:

$$u_\ell = c_{\ell_3} y^3 + \left\{ \frac{1}{2\mu_\ell} \frac{dP_a}{dx} + \frac{\rho_\ell g_y}{2\mu_\ell} \frac{dt}{dx} \right\} y^2 + c_{\ell_1} y, \tag{85}$$

and

$$u_a = c_{a_3} \left(\frac{y^3}{b} - 3y^2 + 2b^2 \right) + \frac{1}{2\mu_a} \frac{dP_a}{dx} (y^2 - b^2) + c_{a_1} (y - b). \tag{86}$$

The velocity distributions presented above satisfy Eqs. 78, 83, 79, and 84. The remaining variable coefficients, c_{ℓ_1}, c_{ℓ_3}, c_{a_1}, and c_{a_3}, can be evaluated by using Eqs. 80, 81, 69, and 70.

Once the remaining coefficients are determined, the assumed velocity profiles can be substituted into the momentum integral equations, Eqs. 76 and 77. Inspection shows that the result will be two simultaneous, second-order, nonlinear differential equations. The dependent variables in these equations are the pressure, P_a, and the film thickness, t. Since the differential equations are of second order, four initial conditions must be specified: the initial film thickness and pressure and the initial gradients of these variables. Normally, the values of the initial gradients of film thickness and pressure are not known without recourse to experiment. This is, therefore, a disadvantage that causes a practical barrier to use of this technique as a predictive method.

g. Discussion. An analytical model describing the flow of thin films under the influence of a concurrent gas phase has been developed. If $dt/dx \ll 1$, boundary-layer-type equations can be used to describe the flow. The influence of the hydrostatic pressure gradient has been indicated by the modified Froude number, $\bar{u}_{\ell_0}^2/g_y L\, dt/dx$.

An approximate method of solution of the boundary-layer-type equations has been proposed, using the momentum integral technique. This method is not, a priori, predictive due to the necessity of the experimental determination of the initial film thickness and pressure gradients.

However, as will be shown in Section 2, below the momentum integral equations offer a simple means of predicting the pressure gradient and the film thickness when the flow regime is turbulent.

2. Turbulent Flow

This section considers the concurrent, turbulent flow of stratified gas and liquid phases. Of principal interest are flows that are not fully developed in the sense that $dt/dx \neq 0$, and whose phase interface is characterized by three-dimensional disturbances.

The purpose of the succeeding development is to construct, for the aforementioned flows, a simple analytical model that requires little knowledge of the details of the local flow mechanics.

a. Critical Film and Gas Reynolds Number. Fulford[19] defined three regimes of film flow: smooth laminar, wavy laminar, and wavy turbulent. The film Reynolds number used to delineate the transition from laminar to turbulent flow is defined as follows:

$$Re_\ell = \frac{W_\ell}{\mu_\ell}. \tag{87}$$

Data concerning the critical Reynolds number might be expected to exhibit some spread since the transition is probably a combination of a Tollmien-Schlichting instability in conjunction with disturbances in the film resulting from the action of the surface waves. After critically examining many data, Fulford concluded that the critical Reynolds number for film flow is between 250 and 400. Fulford noted that the critical Reynolds number is usually determined from distinct slope changes in the curves of film thickness, surface velocity, heat- or mass-transfer coefficients in the film, etc., when plotted against Re_ℓ.

Complete data are not available regarding the critical Reynolds number for two-dimensional flow of a single-phase fluid. Therefore, the critical Reynolds number for the gas phase will be bracketed by considering the critical Reynolds number of single-phase fluids flowing in conduits of similar geometry. Schlichting[41] defined the Reynolds number for conduits of noncircular cross section as

$$Re_a = \frac{\overline{u}_a R_h}{\nu_a}, \tag{88}$$

where R_h denotes the hydraulic diameter. In Figure 20.12 of Ref. 41, Schlichting plots friction factors versus Re_a for various geometries. For a rectangular conduit of aspect ratio 3.5:1, the break in the curve occurs at a Reynolds number of approximately 2000. Another curve in that figure is for a narrow annulus, which is analogous to a rectangular channel of large aspect ratio. The critical Reynolds number from this curve appears to be 4000. Thus, the critical Reynolds number in this research will be assumed to be from 2000 to 4000.

b. Momentum Integral Equations. The shear-stress terms in the momentum integral equations already derived for the laminar flow of the gas and liquid phases were expressed in terms of the products of the viscosity times the gradient of velocity in the y direction, evaluated at either the wall or the interface. Writing the shear stresses in terms of the symbol τ, and considering u to be the time-averaged velocity in the x direction, we can assume the momentum integral equations to be valid for turbulent flow as well as laminar flow. Thus, for turbulent gas and liquid flow, the momentum integral equations are

$$\frac{d}{dx}\int_0^t u_\ell^2 dy = -\frac{t}{\rho_\ell}\frac{dP_a}{dx} - g_y t\frac{dt}{dx} + \frac{1}{\rho_\ell}(\tau_i - \tau_0), \tag{89}$$

and

$$\frac{d}{dx}\int_t^b u_a^2 dy = -\frac{b-t}{\rho_a}\frac{dP_a}{dx} - \frac{1}{\rho_a}(\tau_i + \tau_b). \tag{90}$$

In Eqs. 89 and 90, τ_b, τ_0, and τ_i represent, respectively, the turbulent shear stress on the upper and lower solid surface and at the gas-liquid interface.

In the development of the momentum integral equations, it has been assumed that the phase interface is smooth. For turbulent liquid and gas flows, this is generally not true. The interface is normally characterized by disturbances that range from two-dimensional waves for the lower Re_ℓ and Re_a through three-dimensional waves, roll waves, and finally, entrainment for the higher Re_a and Re_ℓ. Data concerning the amplitude and frequency of these interfacial waves for nonfully developed flows ($dt/dx \neq 0$) are lacking. Thus, with the aforementioned state of knowledge regarding interfacial disturbances, it is reasonable to assume a smooth interface and include the effects of waves in the evaluation of τ_i. This allows the construction of a relatively simple analytical model, as evidenced by Eqs. 89 and 90.

Another assumption is that there is no mass transfer across the phase interface. This eliminates, in effect, the consideration of entraining flows by the present model.

c. Velocity Profiles in the Gas and Liquid Phases. As for laminar gas and liquid flow, velocity distributions must be assumed in each phase so that the convective momentum terms can be evaluated. However, because of the relative "flatness" of turbulent velocity profiles, it is possible to bypass the necessity of explicitly introducing assumed velocity distributions into the convective momentum terms. For example, it can be assumed for comparison that the velocity distribution in the gas phase follows the well-known 1/7 power law. That is,

$$\frac{u_a}{u_{max}} = \left(\frac{2y}{b - t}\right)^{1/7}. \tag{91}$$

To show that the velocity distribution in the convective-momentum terms do not need to be considered explicitly, it is necessary that

$$\overline{u_a^2} \simeq \bar{u}_a^2.$$

The definitions of $\overline{u_a^2}$ and $\bar{u}_a^2$ are

$$\overline{u_a^2} \equiv \frac{2}{b - t} \int_0^{\frac{b-t}{2}} u_a^2 \, dy \tag{92}$$

and

$$\bar{u}_a^2 \equiv \frac{4}{(b-t)^2}\left(\int_0^{\frac{b-t}{2}} u_a \, dy\right)^2 . \tag{93}$$

Substituting Eq. 91 into Eqs. 92 and 93 and integrating gives

$$\overline{u_a^2} = \frac{64}{63}\bar{u}_a^2 .$$

Therefore, the error in replacing $\overline{u_a^2}$ by $\bar{u}_a^2$ is approximately 1.6%. A similar result is obtained by assuming the 1/7 power law for the film.

Thus, the convective momentum terms can be expressed approximately as

$$\frac{d}{dx}\int_0^t u_\ell^2 dy = \frac{d}{dx}(t\bar{u}_\ell^2),$$

and

$$\frac{d}{dx}\int_t^b u_a^2 dy = \frac{d}{dx}\left((b-t)\,\bar{u}_a^2\right).$$

These last two equations can be rewritten by using Eqs. 69 and 70, giving

$$\frac{d}{dx}\int_0^t u_\ell^2 dy = -\frac{W_\ell^2}{\rho_\ell^2 t^2}\frac{dt}{dx}, \tag{94}$$

and

$$\frac{d}{dx}\int_t^b u_a^2 dy = \frac{W_a^2}{\rho_a^2 (b-t)^2}\frac{dt}{dx}. \tag{95}$$

Substituting Eqs. 94 and 95 into Eqs. 89 and 90 yields

$$-\frac{W_\ell^2}{\rho_\ell^2 t^2}\frac{dt}{dx} = -\frac{t}{\rho_\ell}\frac{dP_a}{dx} - g_y t\frac{dt}{dx} + \frac{1}{\rho_\ell}(\tau_i - \tau_0), \tag{96}$$

and

$$\frac{W_a^2}{\rho_a^2(b-t)^2}\frac{dt}{dx} = -\frac{b-t}{\rho_a}\frac{dP_a}{dx} - \frac{1}{\rho_a}(\tau_i + \tau_b). \tag{97}$$

Equations 96 and 97 are simultaneous, nonlinear, ordinary, differential equations in the dependent variables, t and P_a. To solve the equations, expressions must be found for the interface shear stress, τ_i, and the two wall shear stresses, τ_b and τ_0.

d. Turbulent Wall Shear Stress. The evaulation of the wall shear stress in the liquid film requires an assumption concerning the turbulent nature of the film, particularly in the region near the wall. Carpenter and Colburn[7] suggested what is termed the "wall-layer model" of film flow. This model assumes that a liquid film flowing under the influence of a high-velocity turbulent gas stream behaves as the wall layer of a single-phase liquid flow with the same thickness and wall shear stress. In other words, an observer looking into the film and observing events at the wall cannot "see" far enough into the liquid to distinguish whether the liquid is flowing as a film or as a single-phase fluid. The "wall-layer model" allows use of a single-phase velocity profile to establish an expression for the wall shear stress.

Different velocity profiles have been used by various investigators in the "wall-layer model." One of the assumed profiles is the von Karman universal velocity distribution. For example, it has been used successfully by Dukler and Bergelin[14] for the falling flow of films on a vertical wall, by Anderson and Mantzouranis[4] for concurrent annular flow, and by Rohsenow, Webber, and Ling[40] for turbulent film condensation.

The universal velocity distribution, which is used in this research, is

$$u_\ell^+ = y^+ \qquad \text{for } 0 \le y^+ \le 5, \tag{98}$$

$$u_\ell^+ = -3.05 + 5.0 \ln y^+ \qquad \text{for } 5 \le y^+ \le 30, \tag{99}$$

and

$$u_\ell^+ = 5.5 + 2.5 \ln y^+ \qquad \text{for } 30 \le y^+ \le t, \tag{100}$$

where

$$u_\ell^+ \equiv u_\ell/u^*,\ y^+ \equiv y\,u^*/\nu_\ell,$$

and

$$u^* \text{ (the frictional velocity)} \equiv \sqrt{\tau_0/\rho_\ell}.$$

For values of $t^+ > 30$, the universal velocity distribution may be integrated, using Eq. 69, to give

$$Re_\ell = 3.0t^+ + 2.5t^+ \ln t^+ - 64. \tag{101}$$

Substituting $t^+ = 30$ into Eq. 101 results in $Re_\ell = 270$. This value of the Reynolds number corresponds closely to the lower value of the critical Reynolds number cited earlier.

Hershman[24] studied the fully developed flow of turbulent air over various liquid films in a channel whose aspect ratio was 12:1. Assuming the "wall-layer model" and using Deissler's velocity distribution, Hershman compared measured values of t^+ versus Re_ℓ for experiments in which three-dimensional waves were present on the film surface. The maximum value of Re_ℓ in his experiments was approximately 600. He concluded that the agreement between experiment and theory was satisfactory. For a given Re_ℓ, the values of t^+ calculated using the von Karman and Deissler velocity profiles agree within 1-4% over the range of t^+ in the Hershman experiments, and this variation is within the experimental scatter of Hershman's data. The principal advantage of using the von Karman distribution over that of Deissler is that the former is easier to use in practice.

An expression for the wall shear stress results from the following definition of t^+:

$$t^+ \equiv \frac{t}{\nu_\ell}\sqrt{\frac{\tau_0}{\rho_\ell}}$$

Rearranging results in

$$\tau_0 = \rho_\ell\left\{\frac{\nu_\ell t^+}{t}\right\}^2. \tag{102}$$

Thus, Eqs. 101 and 102 are a set of equations that allow the evaluation of the wall shear stress, τ_0, in terms of the film thickness, t, and the film Reynolds number, Re_ℓ.

The evaluation of the wall shear stress in the gas phase requires knowledge of the turbulent profile in the gas phase, particularly in the region of the wall. Hanratty and Engen[22] found, for the fully developed flow of a horizontal, stratified, turbulent gas and liquid, that the velocity profile in the gas phase near the wall was unaffected by the presence of the moving liquid phase.

In light of these results, it is assumed that the wall shear stress in the gas phase may be determined from the Blasius equation for the friction factor in turbulent flow.[41]

The Blasius equation for the friction factor is defined as

$$f_b = \frac{0.316}{(Re_a)^{1/4}}. \tag{103}$$

The relationship between the friction factor and the wall shear stress for a rectangular channel is defined by

$$\tau_b = \frac{f_b}{8}\rho_a \bar{u}_a^2. \tag{104}$$

Combining Eqs. 103 and 104 and using the continuity equation, Eq. 70 yields

$$\tau_b = \frac{0.316}{(Re_a)^{1/4}} \frac{W_a^2}{8\rho_a(b - t)^2}. \tag{105}$$

Cohen[9] measured the wall shear stress for the flow of air in a rectangular channel of aspect ratio 12:1. He found that the Blasius friction factor increased by about 9%. That is,

$$f_b = \frac{0.346}{(Re_a)^{1/4}}. \tag{106}$$

Since the aspect ratio for the gas flow in the experimental test section used in this research is approximately 10:1, this result is used in place of Eq. 103. Cohen's data further indicate that Eq. 106 is valid above $Re_a \simeq 7000$. Replacing the coefficient in Eq. 105 gives

$$\tau_b = \frac{0.346}{(Re_a)^{1/4}} \frac{W_a^2}{8\rho_a(b - t)^2}. \tag{107}$$

e. Interfacial Shear Stress. The evaluation of the shear stress at the interface between the gas phase and liquid film is complicated by the wavy structure. Depending on the Reynolds numbers of the gas and liquid phases, various interfacial wave forms occur.

The various interfacial disturbances that appear as the gas flowrate is increased for a fixed liquid flowrate are: 1) smooth surface, 2) two-dimensional waves, 3) three-dimensional waves (pebbly structure), 4) roll waves, and 5) entrainment. The characteristic amplitude and wavelength of the various disturbances are functions of both the gas and liquid Reynolds numbers.

Reasoning that the effect of the waves on the gas phase is similar to that of a roughened solid surface, attempts have been made to correlate the interfacial friction factor by using the method of Nikuradse.[41] This necessitates establishing a relationship between the "equivalent sand roughness" of Nikuradse and the actual interfacial structure. For example, Lilleleht and Hanratty[33] compared the root-mean-square displacement of the film from its average height with Nikuradse's measurements with sand roughness. An order-of-magnitude agreement was achieved. The principal disadvantage of this method is that it requires knowledge of the actual interfacial structure.

In the three-dimensional wave regime (the regime of principal interest in this research), a simple model is proposed so that detailed knowledge of the interfacial structure is not necessary. The interface friction factor is defined as

$$f_i \equiv \frac{8\tau_i}{\rho_a \overline{u}_a^2}. \tag{108}$$

In place of the average velocity of the gas, the difference between the average velocities in the gas and liquid phases could be used in Eq. 108. However, the average gas velocity is normally much larger than the average liquid velocity; therefore, choosing the latter over the former has no advantage.

Hershman[24] measured values of f_i for the flow of air over various liquid films when $dt/dx = 0$. He noted that over the various wave regimes, f_i was a function of both Re_ℓ and Re_a for a given liquid. Cohen,[9] using the same experimental facility as Hershman, found that in the three-dimensional wave regime, f_i was essentially independent of the air velocity and could be correlated with a dimensionless root-mean-square wave-height parameter. The independence of f_i on Re_a is analogous to the independence of the friction factor on Reynolds number for flow in a rough pipe where the roughness elements are coarse and closely spaced.[41] Cohen's data further revealed that the root-mean-square wave height varied with Re_ℓ for a given Re_a. These results suggest the possibility of constructing a correlation for the interfacial friction factor as a function of Re_ℓ alone.

A correlation of the type suggested above represents a significant simplification of the problem of evaluating the interface shear stress. In effect, such a correlation allows the calculation of the interfacial shear stress without reference to any detailed knowledge of the interfacial structure. Using Cohen's data for the flow of air over water as the basis for the construction of a correlation, the following relationship between f_i and Re_ℓ is proposed:

For $Re_\ell < 340$,

$$f_i = 7.5 \cdot Re_\ell \cdot 10^{-5} + 0.0272; \tag{109}$$

for $Re_\ell > 340$,

$$f_i = 0.926 \cdot Re_\ell \cdot 10^{-5} + 0.0524. \tag{110}$$

Figure 2 compares Eqs. 109 and 110 and Cohen's data. These data cover a range of Re_a from 7,000 to 11,000.

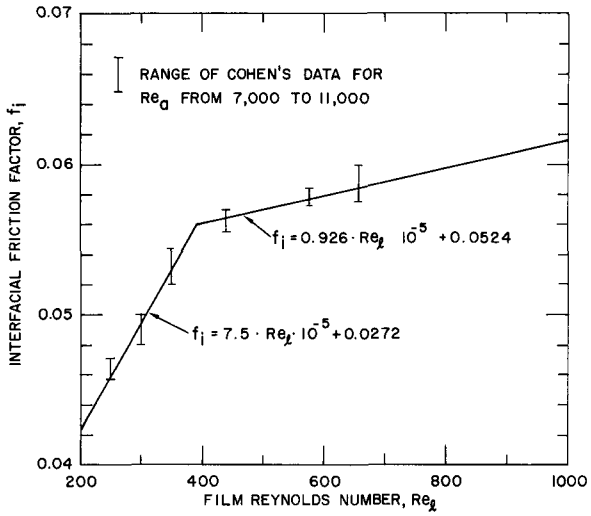

Fig. 2. Comparison of the Proposed Relationship for the Interfacial Friction Factor with the Data of Cohen.

The transition to three-dimensional waves, as pointed out by Cohen, is a function of liquid viscosity. Therefore, the proposed correlation is probably limited to liquids with viscosities comparable to that of water. The possible extrapolation of this correlation to Re_ℓ greater than the range of Cohen's data was investigated experimentally.

B. One-component Flow

The stratified flow of a one-component fluid in which the mass flow across the phase interface is from the vapor to liquid is usually referred to as film condensation. In this section, an analytical model is developed to describe film condensation when the vapor and liquid phases are turbulent. The assumptions made in the succeeding development are similar to those made for the two-component flow in Section A. The principal difference between the model of film condensation delineated here and previously developed models is that it is assumed that the phase change that occurs is a result of the subcooling in the film and that no heat is transferred from the film to the ambient (adiabatic walls).

1. Turbulent Momentum Equations

a. Momentum Integral Equations. The assumptions, which are similar to those made in Section A, pertinent to the development of the model are:

1. The flow pattern is turbulent and two-dimensional.
2. The fluids are incompressible.

3. The interface between the vapor and liquid streams is smooth.

4. The flow is time-independent.

5. $dt/dx \ll 1$.

Since $dt/dx \ll 1$, the boundary-layer-type equations are assumed applicable to the vapor and liquid streams. For turbulent flow, Eqs. 74 and 75 are:

For the film,

$$\frac{d}{dx}\int_0^t u_\ell^2 dy - u_\ell\Big|_t \frac{d}{dx}\int_0^t u_\ell dy = -\frac{t}{\rho_\ell}\frac{dP_s}{dx} - g_y t\frac{dt}{dx} + \frac{1}{\rho_\ell}(\tau_i - \tau_0); \tag{111}$$

for the vapor phase,

$$\frac{d}{dx}\int_t^b u_s^2 dy - u_s\Big|_t \frac{d}{dx}\int_t^b u_s dy = -\frac{b-t}{\rho_s}\frac{dP_s}{dx} - \frac{1}{\rho_s}(\tau_b + \tau_i). \tag{112}$$

The subscript s refers to the vapor phase.

Assuming, as in Section A, that $\overline{u^2} \simeq \overline{u}^2$ for each phase, the first terms on the left-hand sides of Eqs. 111 and 112 can be written as

$$\frac{d}{dx}\int_0^t u_\ell^2 dy \simeq \frac{d}{dx}\left(t\overline{u}_\ell^2\right) \tag{113}$$

and

$$\frac{d}{dx}\int_t^b u_s^2 dy \simeq \frac{d}{dx}\left[(b-t)\,\overline{u}_s^2\right]. \tag{114}$$

At any given x, continuity considerations require that

$$W_\ell = \int_0^t \rho_\ell u_\ell \, dy, \tag{115}$$

and

$$W_s = \int_t^b \rho_s u_s \, dy. \tag{116}$$

Using Eqs. 115 and 116, Eqs. 113 and 114 can be expressed as

$$\frac{d}{dx}\int_0^t u_\ell^2 dy \simeq \frac{1}{\rho_\ell^2}\frac{d}{dx}\left(\frac{W_\ell^2}{t}\right), \tag{117}$$

and

$$\frac{d}{dx}\int_0^t u_s^2 dy \simeq \frac{1}{\rho_s^2}\frac{d}{dx}\left(\frac{W_s^2}{b-t}\right). \tag{118}$$

Differentiating Eqs. 115 and 116 with respect to x yields

$$\frac{1}{\rho_\ell}\frac{dW_\ell}{dx} = \frac{d}{dx}\int_0^t u_\ell\, dy, \tag{119}$$

and

$$\frac{1}{\rho_s}\frac{dW_s}{dx} = \frac{d}{dx}\int_t^b u_s\, dy. \tag{120}$$

Substituting Eqs. 117-120 into Eqs. 111 and 112 gives

$$-\frac{W_\ell^2}{\rho_\ell^2 t^2}\frac{dt}{dx} + \left(\frac{2W_\ell}{\rho_\ell^2 t} - \frac{u_\ell|_t}{\rho_\ell}\right)\frac{dW_\ell}{dx} = -\frac{t}{\rho_\ell}\frac{dP_s}{dx} - g_y t\frac{dt}{dx} + \frac{1}{\rho_\ell}(\tau_i - \tau_0), \tag{121}$$

and

$$\frac{W_s^2}{\rho_s^2(b-t)^2}\frac{dt}{dx} + \left(\frac{2W_s}{\rho_s^2(b-t)} - \frac{u_s|_t}{\rho_s}\right)\frac{dW_s}{dx} = -\frac{b-t}{\rho_s}\frac{dP_s}{dx} - \frac{1}{\rho_s}(\tau_b + \tau_i). \tag{122}$$

Note that $dW_\ell/dx = -dW_s/dx$, and that the value of dW_s/dx is evaluated from energy considerations. Equations 121 and 122 are simultaneous, nonlinear, ordinary differential equations whose dependent variables are t and P_s. To solve these equations, relationships for τ_i, τ_0, τ_b, $u_\ell|_t$, and $u_s|_t$ must be established. In Section A, expressions for τ_b and τ_0 have been delineated, and these results are assumed applicable to the present case.

b. Interfacial Velocity. At the interface, Eq. 80 requires that

$$u_\ell|_t = u_s|_t.$$

Although the interface has been assumed to be smooth, the interface is highly disturbed in the actual case. The interface velocity, $u|_t$, could be anywhere between the average vapor velocity and the average liquid velocity. In their analysis of turbulent film condensation, Carpenter and Colburn[7] chose the vapor velocity. However, because of the order-of-magnitude difference in the viscosities of the vapor and liquid phases, the magnitude of the interface velocity is probably closer to the liquid average velocity than to the vapor average velocity. The relationship between $u|_t$ and $\bar{u}_\ell$ is frequently expressed as

$$u|_t = \beta \bar{u}_\ell. \tag{123}$$

Various investigators of turbulent film condensation have chosen values of β in the range from 1 to 2. For example, Hilding[26] used $\beta = 2$, while Soliman, Schuster, and Berenson[45] used $\beta = 1.25$. Assuming the interface to be smooth and the velocity profile in the film to follow the 1/7 power law, the value of β is calculated to be 1.14. Since the contribution of the momentum term containing the interface velocity has usually been found to be of minor importance (Rohsenow, Webber, and Ling[40]), the value of 1.14 is used in this report.

If the indicated substitution for $u|_t$ is made, Eqs. 121 and 122 become

$$\left(-\frac{W_\ell^2}{\rho_\ell^2 t^2} + g_y t\right)\frac{dt}{dx} + \frac{t}{\rho_\ell}\frac{dP_s}{dx} = -\left(\frac{0.86 W_\ell}{\rho_\ell^2 t}\right)\frac{dW_\ell}{dx} + \frac{1}{\rho_\ell}(\tau_i - \tau_0), \tag{124}$$

and

$$\frac{W_s^2}{\rho_s^2 (b-t)^2}\frac{dt}{dx} + \frac{b-t}{\rho_s}\frac{dP_s}{dx} = \left\{\frac{2W_s}{\rho_s^2 (b-t)} - \frac{1.14 W_\ell}{\rho_s \rho_\ell t}\right\}\frac{dW_\ell}{dx} - \frac{1}{\rho_s}(\tau_b + \tau_i). \tag{125}$$

c. Effect of Condensation on the Interface Shear Stress. In constructing models of turbulent film condensation, investigators have generally acknowledged that establishing a model for evaluating the interface shear stress is particularly difficult. Part of the difficulty is that the structure of the phase interface is normally disturbed. This part of the problem has been discussed in Section A. However, the principal difficulty has been to assess to the effect of condensation on the interface shear stress.

Because of the relative abundance of data for two-component systems in comparison to one-component systems, many investigators have used these data and ignored the effect mentioned in the last sentence of the above paragraph. Soliman, Schuster, and Berenson[45] stated that there is no effect of condensation on the interface shear stress.

In contrast to the aforementioned assumptions of most investigators of turbulent film condensation, Silver[43] and Silver and Wallis[44] tried to account for the effect of condensation on interfacial shear stress by using the concept of a "Reynolds flux" in the vapor phase. Admitting to the possible oversimplification of the actual phenomenon, Silver and Wallis derived the following result:

$$\frac{\lambda_i^*}{\lambda_i} = \exp\left(\frac{\phi}{2\lambda_i}\right) - \frac{\phi}{\lambda_i}, \tag{126}$$

where

$$\phi \equiv \frac{2}{\rho_s \bar{u}_s} \frac{dW_s}{dx}, \tag{127}$$

and

$$\lambda_i = \frac{f_i}{4} = \frac{2\tau_i}{\rho_s \bar{u}_s^2}. \tag{128}$$

Note that λ_i^* and λ_i are, respectively, the friction factors with and without condensation for the same free-stream conditions. Note also that dW_s/dx is negative.

Equation 126 was not compared to any data on turbulent film condensation. However, the form Eq. 126 is reasonable, as may be seen by the following analogy. The effect of condensation on interface shear stress may be visualized by analogy with the familiar problem of suction from turbulent boundary layers flowing over flat plates. The shear stress at the surface of the flat plate in the presence of suction is augmented by a term which is proportional to the volumetric suction rate times the free-stream velocity. This result is clearly consistent with Eq. 126.

Mickley et al.[38] used "film theory" to develop an expression relating the friction factor with suction to the friction factor without suction for the same free-stream flow conditions. Their results was

$$\frac{\lambda_i^*}{\lambda_i} = \frac{\phi/\lambda_i}{\exp(\phi/\lambda_i) - 1} \tag{129}$$

They concluded that, within the precision of their experimental results, film theory predicted the measured effect of suction on the friction factor.

Equations 126 and 129 may be compared by considering large values of the suction parameter, ϕ. Both equations indicate that λ_i^*/λ_i is approximately equal to ϕ. From Eq. 128, this result shows that the interface shear stress is proportional to the product of the condensation rate and the average vapor velocity. That is,

$$\tau_i \simeq -\bar{u}_s \frac{dW_s}{dx}. \tag{130}$$

The above result is, perhaps, an indication of the reason for the success of the model of Carpenter and Colburn[7] for turbulent film condensation. Although Carpenter and Colburn used two-component flow data to evaluate f_i, they considered the interface velocity to be equal to $\bar{u}_s$. Since $\bar{u}_s$ is usually much larger than $u|_t$, they, in fact, correctly accounted for the total momentum exchange at the interface.

Neither Eq. 126 nor 129 is based on a model that is completely analogous to film condensation, i.e., a flat plate with no pressure gradient, in comparison to a wavy, moving surface in the presence of a pressure gradient. However, in light of these models, and considering the success of the Carpenter and Colburn correlation, a simple model is proposed. In essence, it is assumed that the interface shear stress is augmented by an amount exactly equal to the condensation rate times the average vapor velocity, or

$$\tau_i = f_i \frac{\rho_s \bar{u}_s^2}{8} - \bar{u}_s \frac{dW_s}{dx}. \tag{131}$$

In terms of the friction factor ratio, λ_i^*/λ_i, this model states that

$$\frac{\lambda_i^*}{\lambda_i} = 1 - \frac{\phi}{\lambda_i}. \tag{132}$$

From Eq. 116, Eq. 131 can be expressed as

$$\tau_i = \frac{f_i}{8} \frac{W_s^2}{\rho_s (b - t)^2} + \frac{W_s}{\rho_s (b - t)} \frac{dW_\ell}{dx}. \tag{133}$$

2. Turbulent Energy Equations

a. Energy Integral Equations. The vapor phase is assumed to be saturated, and the temperature of the vapor is assumed to be constant throughout the region of interest. Thus, the only energy equation considered pertains to the liquid phase. It is assumed that the turbulent boundary-layer-type energy equation can be applied to the film to give

$$u_\ell \frac{\partial T_\ell}{\partial x} + v_\ell \frac{\partial T_\ell}{\partial y} = \frac{\partial}{\partial y}\left(\alpha_\ell \frac{\partial T_\ell}{\partial y}\right), \tag{134}$$

where α_ℓ is the turbulent thermal diffusivity. The pertinent boundary conditions are

$$y = 0; \quad u_\ell = 0; \quad v_\ell = 0; \tag{135}$$

$$T_\ell = T_0; \tag{136}$$

$$y = t; \quad T_\ell = T_s. \tag{137}$$

Integrating Eq. 134 with respect to y yields

$$\int_0^t u_\ell \frac{\partial T_\ell}{\partial x} + \int_0^t v_\ell \frac{\partial T_\ell}{\partial y} = \int_0^t \frac{\partial}{\partial y}\left(\alpha_\ell \frac{\partial T_\ell}{\partial y}\right) dy. \tag{138}$$

The right-hand side of the above equation becomes

$$\int_0^t \frac{\partial}{\partial y}\left(\alpha_\ell \frac{\partial T_\ell}{\partial y}\right) dy = \alpha_\ell\Big|_t \frac{\partial T_\ell}{\partial y}\Big|_t - \alpha_\ell\Big|_0 \frac{\partial T_\ell}{\partial y}\Big|_0.$$

The surface at y = 0 is assumed to be adiabatic; i.e., condensation results from subcooling in the film. Therefore,

$$\int_0^t \frac{\partial}{\partial y}\left(\alpha_\ell \frac{\partial T_\ell}{\partial y}\right) = \alpha_\ell\Big|_t \frac{\partial T_\ell}{\partial y}\Big|_t. \tag{139}$$

The second term on the left-hand side of Eq. 138 may be integrated by parts to give

$$\int_0^t v_\ell \frac{\partial T_\ell}{\partial y} = v_\ell\Big|_t T_s - v_\ell\Big|_0 T_0 - \int_0^t T_\ell \frac{\partial v_\ell}{\partial y}\, dy.$$

Noting that $v_\ell|_0 = 0$ and using the continuity equation produces

$$\int_0^t v_\ell \frac{\partial T_\ell}{\partial y} = -T_s \int_0^t \frac{\partial u_\ell}{\partial x} dy + \int_0^t T_\ell \frac{\partial u_\ell}{\partial x} dy. \tag{140}$$

Substituting Eqs. 139 and 140 into Eq. 138 results in

$$\int_0^t \frac{\partial}{\partial x}(u_\ell T_\ell)dy - T_s \int_0^t \frac{\partial u_\ell}{\partial x} dy = \alpha_\ell|_t \left.\frac{\partial T_\ell}{\partial y}\right|_t$$

Using Liebnitz's rule on the left-hand side of the above equation produces the energy integral equation,

$$\frac{d}{dx}\int_0^t u_\ell T_\ell dy - T_s \frac{d}{dx}\int_0^t u_\ell dy = \alpha_\ell|_t \left.\frac{\partial T_\ell}{\partial y}\right|_t. \tag{141}$$

Equation 141 may be simplified further by assuming that the temperature in the film is uniform and equal to the temperature at $y = 0$. Justification for this assumption lies in the effect of the interfacial disturbances on the film. Hilding and Coogan[25] measured film thickness for high-velocity condensing annular flow inside horizontal tubes. Their results indicated that the waves deeply penetrated the film. A plot of the ratio of mean film thickness to the maximum wave height versus film average velocity showed the average ratio to be about 1/2. Since the model considered here assumed that the surface at $y = 0$ is adiabatic, the resulting agitation of waves on the film may be visualized as tending to minimize any temperature gradients in the y direction. If it is assumed, therefore, that $T_\ell \simeq T_0$, Eq. 141 becomes

$$\rho_\ell C_p \frac{d}{dx}\left(T_0 \int_0^t u_\ell dy\right) - \rho_\ell C_p T_s \frac{d}{dx}\int_0^t u_\ell dy = K_\ell|_t \left.\frac{\partial T_\ell}{\partial y}\right|_t, \tag{142}$$

where $K_\ell|_t$ is the turbulent thermal conductivity.

The right-hand side of Eq. 142 represents the heat transferred into the film by the condensation process. This is expressed by

$$q_c = K_\ell|_t \left.\frac{\partial T_\ell}{\partial y}\right|_t = h_{fg}\frac{dW_\ell}{dx}. \tag{143}$$

Substituting Eqs. 143 and 119 into Eq. 142 gives the final form of the film energy equation,

$$C_p W_\ell \frac{dT_0}{dx} + C_p(T_0 - T_s) \frac{dW_\ell}{dx} = h_{fg} \frac{dW_\ell}{dx}. \tag{144}$$

Alternatively, Eq. 144 may be expressed in terms of the enthalpy of the liquid film by assuming $h_\ell = C_p T_\ell$. Thus,

$$W_\ell \frac{dh_0}{dx} = (h_g - h_0) \frac{dW_\ell}{dx}. \tag{145}$$

To solve Eqs. 144 and 145 requires finding an independent relationship for the condensation rate, dW_ℓ/dx.

b. Condensing Heat-transfer Coefficient. Many correlations have been proposed for the condensing heat-transfer coefficient for turbulent film condensation. In general, the models developed are for films that are cooled by heat transfer through the wall and have, therefore, emphasized the "laminar" region of the film close to the wall. It has been assumed that the remaining "turbulent" region of the film contributed insignificantly to the overall thermal resistance.[7]

In this research, the wall is adiabatic. Therefore, the region of the film near the wall is not expected to be the major thermal resistance. Instead, it might be supposed that because of interfacial disturbances on the film, the major thermal resistance is related to some overall characteristics of the film.

The condensing heat-transfer coefficient is defined as

$$h \equiv \frac{q_c}{T_s - T_0}. \tag{146}$$

From Eq. 143, the heat transferred to the film is related to the temperature gradient at the interface times an effective turbulent thermal conductivity, or

$$q_c = K_\ell \Big|_t \frac{\partial T_\ell}{\partial y}\Big|_t. \tag{143}$$

The unsteady, chaotic motion of turbulent flow is frequently characterized by the concept of turbulent eddies. In terms of the kinetic energy of the turbulent motion, the "large-scale" eddies are considered to contain the main part of the kinetic energy, supplying this energy to the

"small-scale" eddies, which in turn dissipate the energy by viscous action. Turbulent eddies are characterized by their velocities and the distances over which their velocities change significantly. Thus, the most rapid eddy motion is present in the large-scale eddies. For example, in pipe flow the large-scale eddies are described in terms of the average velocity of the flow and the diameter of the tube.

In free turbulent flow, Prandtl[41] related the eddy diffusivity for momentum to the large-scale eddies. He hypothesized that the momentum transferred in the mixing zone was determined by the dimensions of this zone and the velocity difference across the zone. This model has found many applications in describing jet flows.

In the transfer of heat in a turbulent film on an adiabatic surface, the transport mechanism is visualized as being largely dependent on the action of the interfacial disturbances. That is, the deep penetrating waves cause a "large-scale eddy motion." Since the characteristic velocity of the film is $\bar{u}_\ell$ and the characteristic dimension of the "mixing zone" is t, it is assumed that the eddy diffusivity of heat may be expressed as

$$\epsilon_H = d_1 t \bar{u}_\ell. \tag{147}$$

The eddy diffusivity of heat is related to the turbulent thermal conductivity by

$$K_\ell\big|_t = K_\ell = \rho_\ell C_p \epsilon_H. \tag{148}$$

Substituting Eq. 147 into Eq. 148 gives

$$K_\ell\big|_t = d_1 \rho_\ell C_p t \bar{u}_\ell = d_1 k_\ell Re_\ell Pr_\ell. \tag{149}$$

Note that $K_\ell \neq f(y)$.

It was assumed earlier that the average temperature of the film is T_0. This implies that the variation of temperature from T_s at the interface to the average temperature, T_0, exists over a very small length, δ, in the vicinity of the interface. Since the mixing zone is assumed equal to the film thickness, it is reasonable to assume that the length, δ, is proportional to t. That is,

$$\delta = d_2 t. \tag{150}$$

Assuming a linear variation of T_ℓ across the length, δ, gives

$$\left.\frac{\partial T_\ell}{\partial y}\right|_t \simeq \frac{T_s - T_0}{d_2 t}. \tag{151}$$

Combining Eqs. 143, 146, 149, and 151 yields

$$h = \frac{d_1}{d_2}\frac{k_\ell}{t} Re_\ell Pr_\ell. \tag{152}$$

Defining

$$Nu_\ell \equiv \frac{ht}{k_\ell},$$

and substituting this definition into Eq. 152 gives

$$\frac{Nu_\ell}{Re_\ell Pr_\ell} = St_\ell = d_3. \tag{153}$$

Thus, the model developed here predicts that the Stanton number is a constant. Note the possible application of this result. In particular, assumptions concerning the cause of the heat transferred to the surface were not required. Thus, this model may find application in describing heat transfer to wavy films in a adiabatic, two-component system. In addition, using the analogy between energy and mass transfer, the model might also predict the absorption of a gas into a wavy liquid film, when the liquid-phase diffusion resistance is controlling.

The constant, d_3, in Eq. 153 must be evaluated by experiment. To accomplish this evaluation, the following form of Eq. 152 is used;

$$h = d_3 \frac{C_p W_\ell}{t}. \tag{154}$$

Combining Eqs. 143 and 146 results in another relationship for h,

$$h = \frac{h_{fg}}{T_s - T_0}\frac{dW_\ell}{dx}. \tag{155}$$

Using Eq. 144 in conjunction with Eqs. 154 and 155 gives the following result for d_3:

$$St_\ell = d_3 = t\frac{dT_0}{dx}\frac{1}{\left[1 + \frac{T_s - T_0}{h_{fg}}\right](T_s - T_0)}. \tag{156}$$

Thus, the Stanton number can be evaluated by measuring the average film thickness, t, the surface temperature, T_0, and the vapor temperature, T_s. This evaluation can also validate the conclusion that the Stanton number is constant.

Equation 156 is not affected by any error resulting from the increase in heat-transfer surface area due to waves.

III. EXPERIMENTAL EQUIPMENT AND PROCEDURE

A. Description

All steam-water experiments were conducted in an experimental facility, which is schematically represented in Fig. 3.

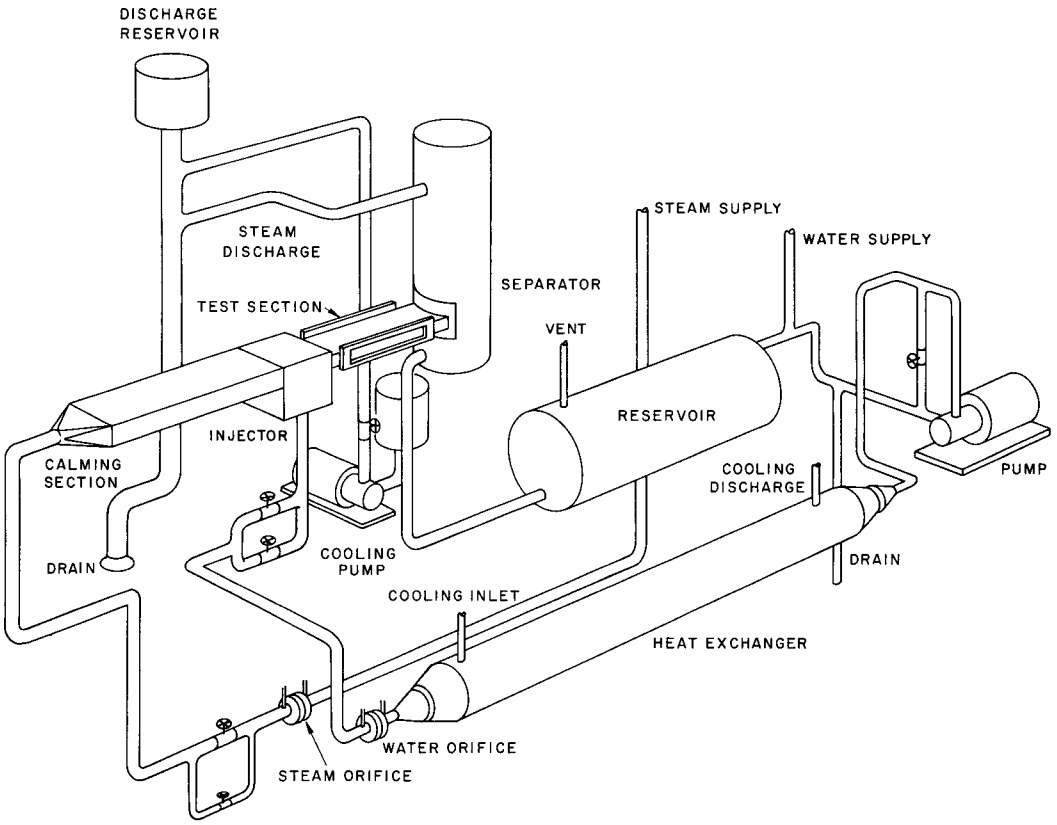

Fig. 3. Schematic Diagram of the Experimental Facility

B. Experimental Equipment

1. Flow Systems

a. Liquid System. The water-supply pressure was produced by a two-stage Aurora turbine pump driven by a 25-hp electric motor. The maximum output of this pump was 100 gpm at 80 psig. All piping from the pump exit to the injector was 1-in. Schedule 40 stainless steel. The shell and tube heat exchanger consisted of a 3-in.-diam pipe containing 17 copper tubes. The 1/2-in.-OD tubes had a wall thickness of 0.0325 in. The water flowrate to the injector was controlled by either a 1- or 1/2-in. globe valve. The water flowrate was determined by measuring the differential pressure across an orifice plate with a manometer.

The liquid system was operated as a closed system. The water was drained by gravity to the feed pump via the reservoir through

a 2-in.-diam flexible hose. The liquid system was not insulated in either the air-water or steam-water experiments. In the steam-water experiments, sufficient heat losses were sustained in the reservoir and associated piping so that cavitation in the pump was prevented. The water temperature at the inlet to the injector was controlled by varying the cooling-water flowrate on the shell side of the heat exchanger. In the air-water experiments, the water temperature was maintained at the ambient temperature.

In the steam-water experiments, the temperature at the exit of the heat exchanger was monitored by a copper-constantan sheathed thermocouple.

b. Air and Steam Systems. The air and steam systems were virtually identical. Laboratory service supplies were used in both systems. The air was supplied through a regulator, which maintained a constant supply pressure. The air temperature was within 2°F of the ambient temperature. No provision was made for controlling the air temperature; the over 300 ft of uninsulated piping from the source reservoir maintained the air at the ambient temperature. This constancy of temperature was further noted by measuring the temperature of the water at the separator inlet. Varying the air flowrate over the ranges used in these experiments produced no noticeable change in water temperature.

The steam was supplied through a regulator so that the pressure at the connection to the loop was 90 psia. The maximum flowrate was 0.2 lb/sec. The air content in the steam supply was measured at the connection to the loop, and the ratio of the mass flowrate of air to steam was approximately 3×10^{-7}. This result is consistent with the fact that the boiler feedwater at the laboratory central steam supply is deaerated.

The piping from the supply to the inlet calming section was 1-in. Schedule 40 stainless steel pipe. The flowrate of air or steam was controlled by either a 1- or 1/2-in. globe valve. The air or steam flowrate was determined by measuring the differential pressure across an orifice plate with a manometer. The upstream pressure at the orifice plate was measured by a Bourdon pressure gauge. In addition, the steam temperature was measured at the orifice plate by the immersion of an iron-constantan sheathed thermocouple in the steam.

The 4-ft-long calming section at the injector inlet was a rectangular stainless steel conduit with inner dimensions of 6 in. (width) by 9/16 in. (height). At the exit of the calming section, the steam temperature was measured by an iron-constantan sheathed thermocouple immersed in the steam, and the pressure was measured by a Heise gauge. These measurements were made to ensure that the steam was not superheated.

The separator in the air-water experiments was a 55-in.-long, 11-in.-diam Lucite tank. The top end of the tank was open to the atmosphere. The separator in the steam-water experiments was a 5-ft-long, 15-in.-diam stainless steel tank. The top of the tank was vented to the atmosphere by a 1-in. copper discharge line. The steam-discharge line was inserted into a 2-in. stainless steel pipe in which cold water was injected by the cooling pump. The supply of cold water condensed the steam to prevent it from entering the drain.

In the steam-water experiments, the steam system was insulated with either $1\frac{3}{4}$-in.-thick Fiberglas insulation covered with an aluminum backing or 1-in. Fiberglas lagging.

c. Injector. The injector introduced two parallel streams of fluid into the test section so that the flow was two-dimensional. Figure 4 is a cross-sectional schematic diagram of the injector. Soft solder was used to fabricate the injector from stainless steel plates.

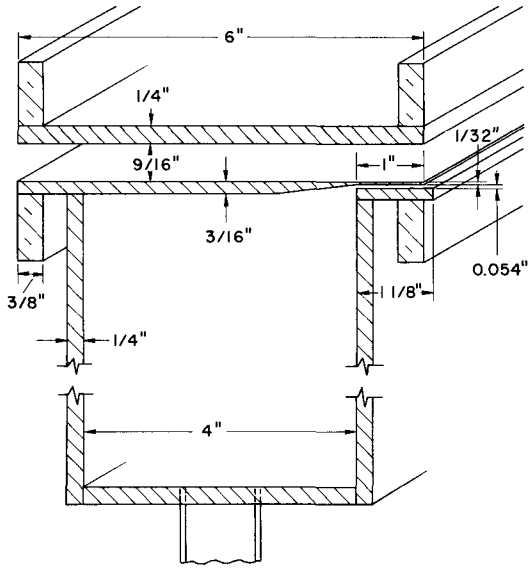

Fig. 4. Cross-sectional Schematic Diagram of the Injector

The most important function of the injector was to ensure that the water formed a uniform film across the lower surface of the test section. To prevent jetting into the gas stream, the horizontal slit immediately adjacent to the initial interaction of the two streams should be as long as possible. There should also be as little material as possible between the two streams at the approach to the point of initial interaction. Because the width of the slit was 6 in., difficulties encountered in machining the surfaces of the slit caused a compromise in achieving the aforementioned desired goals. The configuration shown in Fig. 4 was the result of this compromise. The large water reservoir, whose inner dimensions were 4 in. (length) by 6 in. (height) by 6 in. (width), was chosen to ensure uniform velocities in the entrance of the slit. This diminished the effect of the transition from the pipe to the narrow slit. Uniformity of the slit at the point where the two streams met was ensured by soft-soldering on the upper surface of the injector four uniformly spaced 1/64-in.-diam pins, which extended to the upper surface of the slit. The lower surface of the slit was extended beyond the exit plane of the injector. This allowed machining the lower surface of the test section to match that of the slit to guarantee a smooth lower surface. The height of the slit, as measured by feeler gauges, was 0.054 in. The inner dimensions of the gas channel were the same as those of the calming section.

In the steam-water experiments, the injector was insulated with $1\frac{3}{4}$-in.-thick Fiberglas insulation covered with aluminum backing, and the temperature of the water in the injector reservoir was measured by an iron-constantan sheathed thermocouple 1/2 in. below the surface separating the steam and water and 3 in. from the exit plane of the injector.

d. Air-Water Test Section. The air-water test section was fabricated from 3/8-in.-thick Lucite sheets. The inner dimensions of the rectangular channel were 6 in. (width) by 21/32 in. (height), yielding an aspect ratio of 9.1:1. The length of the test section was 2.5 ft.

The lower surface of the test section was machined so that its union with the lower surface of the slit of the injector was smooth. At approximately 3/8 in. from the plane of the injector exit, three 1/32-in. needles were inserted flush with the lower surface of the test section. These needles, which were used for dye-injection studies, were 1/2, $2\frac{1}{2}$, and $4\frac{1}{2}$ in. from one side of the test section.

Symmetric about the centerline of the test section and normal to the flow, 1/8-in. stainless steel electrodes (conductance probes) were mounted flush with the lower surface of the test section. The spacing between the centers of each pair of electrodes was 1/2 in. The first pair of electrodes was mounted 1 in. from the exit plane of the injector along the axis of flow. Additional pairs of electrodes were placed at 2-in. intervals through the first 13 in. Further pairs of electrodes were spaced at 6-in. intervals to the end of the test section. Four more pairs of electrodes were mounted normal to the direction of flow, 13 in. from the exit plane of the injector. Again, the spacing between the centers of the electrodes was 1/2 in. The centers between the four pairs of electrodes were positioned symmetrically with respect to the centerline of the test section at distances of 1.25 and 2.25 in.

A needle-contact probe was mounted on the upper surface of the test section, 3 in. from the exit plane of the injector. The details of the needle-contact-probe assembly are given in Section B.2.a of this chapter. The relative distance between the needle-contact probe and the lower surface of the test section was measured by a micrometer anchored to the test section by an aluminum bracket.

At the exit of the test section, the water temperature was measured by an iron-constantan thermocouple inserted into the film.

e. Steam-Water Test Section. Figure 5 is a photograph of the steam-water test section in place in the experimental facility. The upper and lower surfaces of the test section were machined from 3/8-in.-thick stainless steel plates. Their length, which was the overall length of the test section, was 18 in. The lower surface was machined so that it mated

smoothly with the lower surface of the slit in the injector. For visual observation of the phenomenon, the sides of the test section were constructed of 1/4-in. stainless steel plates and optical glass. The first $1\frac{1}{2}$ in. and the last $3\frac{1}{2}$ in. of the test-section sides were stainless steel; the middle 13 in. was glass. The glass was ground in a step pattern, forming a flange for sealing as shown schematically in Fig. 6. Stainless steel flanges were then machined to fit over the glass and bolted in place. The stainless steel components of the test section were fabricated by using soft solder.

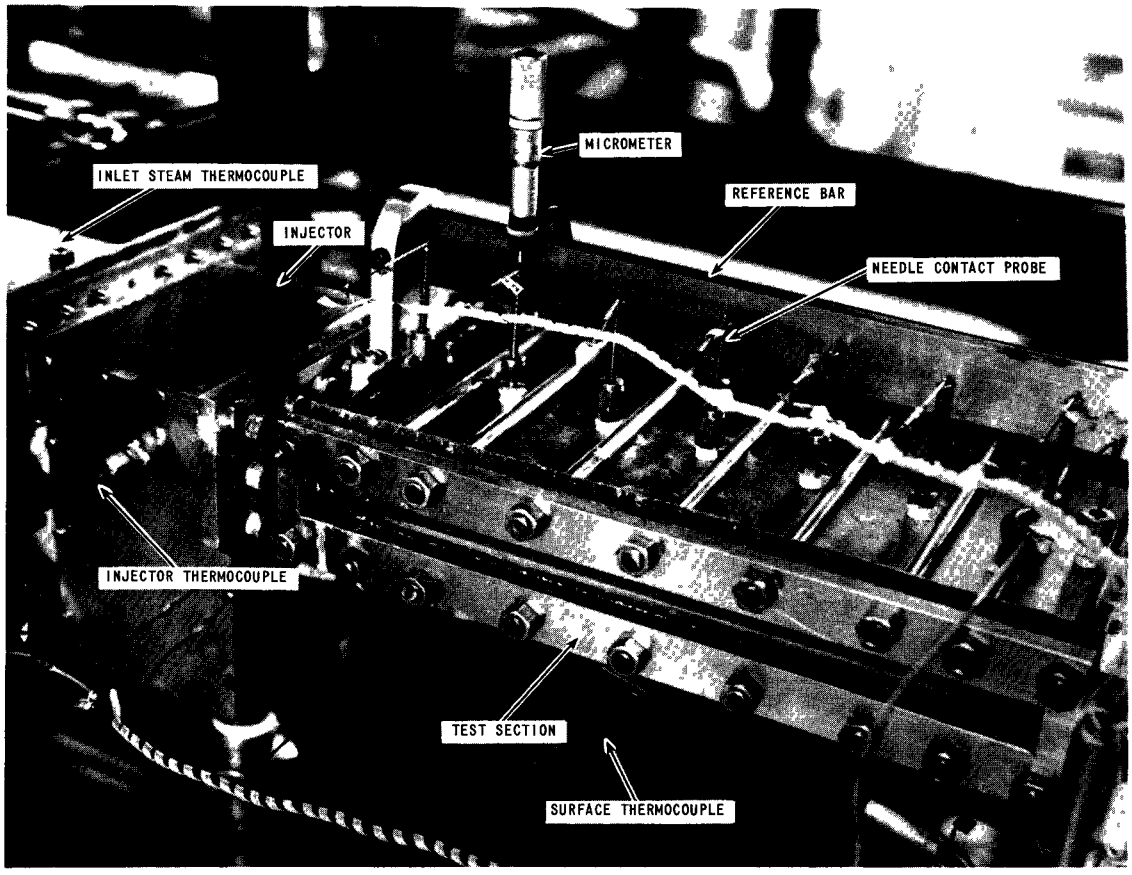

112-9801-A

Fig. 5. Steam-Water Test Section

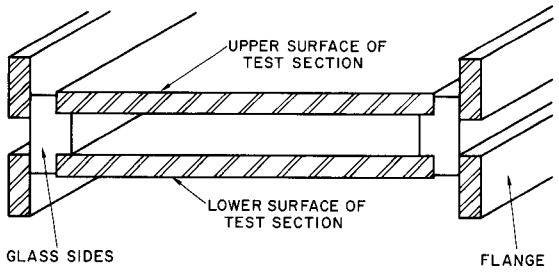

Fig. 6

Cross-sectional Schematic Diagram of Steam-Water Test Section

Thermocouples used to measure the surface temperature of the water along the centerline of the test section were positioned at the exit plane of the injector, 3/8 in. from the exit plane, and at successive 1-in. intervals thereafter to the exit of the test section. In all, there were 17 thermocouples. The water-surface thermocouples were fabricated from select-grade, 30-gauge copper-constantan wire. A silver-solder junction was formed, cut in half, and mechanically forced through a die so that its diameter was 0.073 in. The thermocouple was then checked for electrical continuity. At the appropriate locations in the lower surface of the test sections, 0.067-in.-diam holes were drilled and counterbored to 0.125 in. The junction of the thermocouples was then mechanically forced into the counterbored hole, flush with the surface, to form a friction fit. The thermocouples were then checked again for electrical continuity.

Eight needle-contact probes were mounted on the upper surface of the test section, $1\frac{3}{8}$ in. from the exit plane of the injector and at successive 2-in. intervals. The 2-in. interval between successive needle-contact probes necessitated the design of a compact device for measuring the position of the tip of the needle-contact probe relative to the lower surface of the test section. A reference bar was provided, extending the length of the test section, along which a micrometer could be indexed from probe to probe. The probe reference bar was machined true to 0.005 in. over its length. Parallel slots at the top and bottom of the bar, 180° apart, and an arc segment were machined to provide a guide for the traversing of the micrometer. A Vlier plunger and slot keys were fixed to the micrometer for indexing and locating the micrometer at each probe location. The bar was fixed to blocks at each end of the test section.

At 2 in. from the exit of the test section, an iron-constantan sheathed thermocouple was inserted into the steam to measure the exiting steam temperature.

Except for the glass surfaces, the test section was insulated with $1\frac{3}{4}$-in.-thick Fiberglas insulation covered with aluminum backing.

In all the experiments, the steam at the inlet to the test section was saturated. This was established by measuring the temperature and pressure of the steam at the inlet of the injector. The quality of the steam at the connection to the service supply was measured over the range of steam flowrates encountered in the experiments. The minimum quality measured was 99%. By conservatively estimating heat losses from the steam, the minimum quality at the entrance to the test section was calculated to be 97%.

2. Film-thickness Measurement Methods

The formidable problem of measuring liquid film thicknesses in the presence of arbitrary disturbances at the gas-liquid interface has

encouraged the development of many different experimental methods. Collier and Hewitt[12] critically reviewed the various techniques that have been employed by experimenters. In general, the various methods can be classified as follows:

a) Methods that measure an "average" thickness over some arbitrary long length of film.

b) Methods that measure a local thickness.

The nature of the experiments conducted in these researches dictated criteria that a film-thickness measurement had to satisfy. Quantitatively, the basic requirement was to measure the local temporal average thickness of the film at selectively spaced distances from the exit plane of the injector. The method of measurement had to be indirect or of such a mobility that arbitrary disturbances were not generated that would interfere with subsequent measurements. The instrument had to be compact to the extent that film thicknesses could be measured at relatively close intervals. Finally, for wavy gas-water interfaces, the technique itself had to provide a temporal mean thickness without requiring additional analytical averaging procedures. Of the many techniques described by Collier and Hewitt,[12] the conductance probes method and the needle-contact-probe method appeared to satisfy most of the cited requirements.

a. Conductance Probes. The conductance-probes method is based on the functional dependence of the electrical conductance of the film on the film thickness. For example, if the probes project across the full thickness of the film, the current field in the film is approximately two-dimensional and equivalent to that of two line electrodes supported in an infinite conducting media. In the latter case, Hewitt, King, and Lovegrove[27] showed that C, the conductance of the film, is linearly related to t, the film thickness. In practice, it has not been desirable to have the probes projecting into the films as they would disrupt the film flow and would have to be adjustable to account for varying film thicknesses. Thus, the probes are mounted flush with the film-solid surface. In this case, the above linear relationship will probably no longer hold (although for small values of t, it should hold approximately); however, the method now provides for an indirect measurement of t.

The basic advantage of this method is that a localized, indirect measurement of film thickness can be obtained. Also, this method can easily provide a temporal mean thickness with appropriate recording instruments or produce limited information about the instantaneous variation of the film with time. The principal disadvantage of this method is that, because of the nonlinearity in the dependence of film conductance on film thickness, the relationship must be established by calibration.

The size, spacing, and geometry of the electrodes are arbitrary. Van Rossum[48] used rectangular electrodes placed normal to the flow. At AERE, Harwell, England,[11,20,27,28] round electrodes were used. Because of the ease in installing round electrodes in the test section, they were used in this research. At Harwell, 1/8-in.-diam stainless steel rods, spaced 1/2 in. apart, were installed parallel to the flow in vertical round tubes. The results of their experiments were quite satisfactory. Therefore, the same rod size and spacings were used in these researches, the orientation of the electrodes being changed, however, by making them normal to the flow. With this orientation, a more localized film thickness was obtained in the direction of the flow. Figure 7 is a schematic diagram of the rods in relation to a typical film.

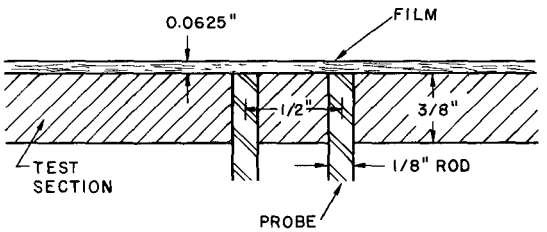

Fig. 7. Orientation of Conductance Probes in Relation to a Typical Film Thickness

Figure 8 is a schematic representation of the conductance-probes circuit. Basically, it was a balanced, ungrounded circuit driven by a Hewlett-Packard audiosweep oscillator (Model 207A). The circuit was balanced and ungrounded to eliminate the effects of capacitance, ground loops, and noise. The size of the 1% resistors was arbitrarily chosen so that the total circuit resistance would be low, yet large enough so that the voltage drop across them was a reasonable fraction of the circuit input voltage. The oscillator was operated arbitrarily at 1000 Hz, a frequency high enough to prevent hydrolysis at the electrode interface, but low enough to avoid capacitance effects.

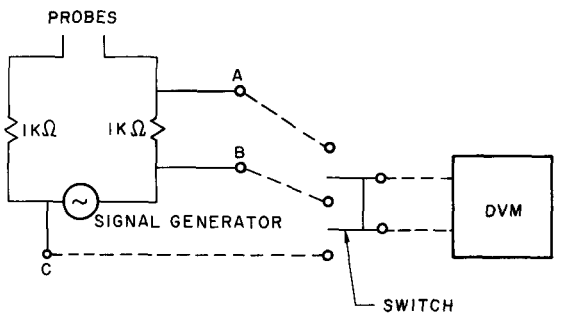

Fig. 8. Circuit for Conductance-probes Method

The voltage supplied to the circuit by the oscillator was approximately 12 V. The conductance or inverse resistance of the film was determined in the following way:

$$E_B - E_C = I(R_P + 2000); \tag{157}$$

$$E_A - E_B = I(1000). \tag{158}$$

Dividing these two equations and rearranging gives

$$C = \frac{1}{R_P} = \frac{10^{-3}}{\frac{E_B - E_C}{E_A - E_B} - 2}. \tag{159}$$

To arrive at temporal mean thicknesses in the presence of arbitrary interfacial disturbances, the instantaneous values of $E_B - E_C$ and $E_A - E_B$ was integrated with time. This was accomplished by using a Hewlett-Packard integrating DVM (Model 2401C) with an ac/ohms converter (Model 2410B). The integrating interval was chosen as 10 sec. Over a large number of runs, the integrated value of $E_A - E_B$ was constant to within three significant figures. Since the lowest wave frequency encountered was approximately 10 Hz, the average included approximately 100 cycles. The accuracy of the aforementioned temporal mean thicknesses is discussed in Appendix A. The time variation of the film was monitored by displaying the voltage drop, $E_A - E_B$, on a Tektronix oscilloscope (Type 531A) with a plug-in differential amplifier (Type D). The differential amplifier eliminated errors due to noise. From the display on the oscilloscope, it was easy to determine, for most cases, a characteristic frequency of the surface disturbances.

Collier and Hewitt[11] noted that the geometry of the calibration cell must be close to that of the experimental test facility. This criterion was incorporated into the design of the calibration cell shown in Fig. 9.

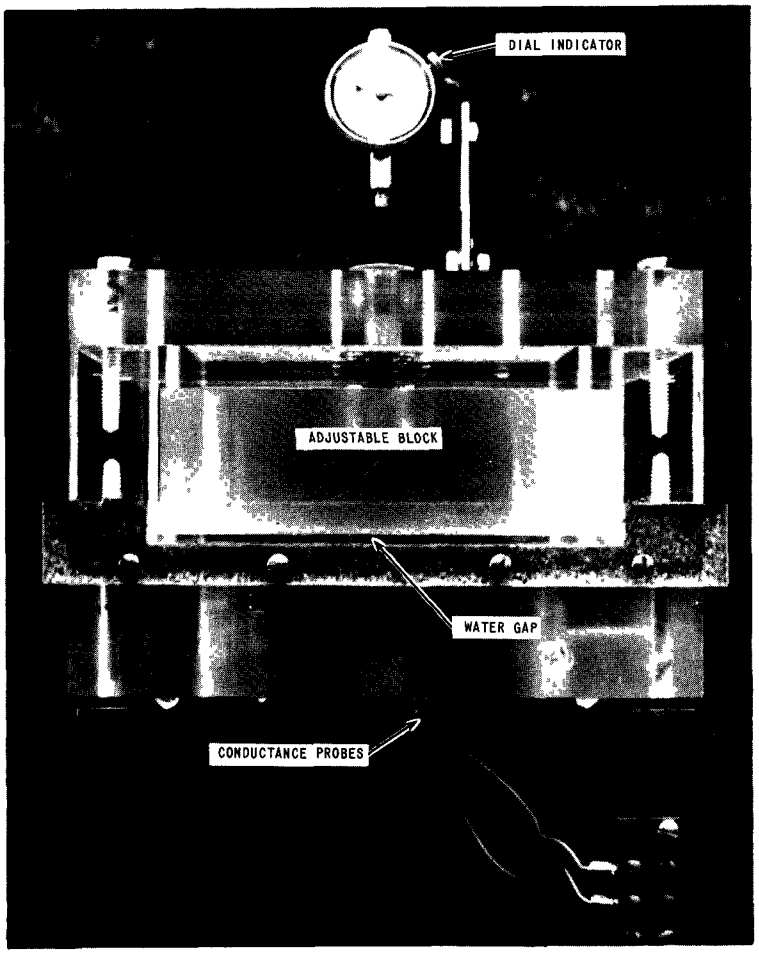

112-9802-A

Fig. 9. Calibration Cell for the Conductance-probes Method

Basically, the cell consisted of two blocks of Lucite arranged such that two carefully prepared flat surfaces could be moved parallel to each other. The flat surfaces were milled and polished, and the maximum deviation across the surface was determined by a surface gauge to be less than 0.0004 in. Two methods of measuring the distance between the surfaces were tried: (1) by placing micrometer-measured shim stock along the four edges, and (2) by measuring the displacement of the adjustment screw by a dial indicator. The dial indicator was used for calibrating, as it was shown to be consistent within 0.001 in. of the value of the surface separation determined by using the shims.

Since tap water was used in the air-water experiments, a calibration curve was obtained each time the loop was filled. The calibration being a function of the specific resistivity of the water, the loop was operated within 2-3°F of room temperature to ensure that the calibration obtained at room temperature was valid. The sample of water used in the calibration was taken directly from the separator at the exit of the test section.

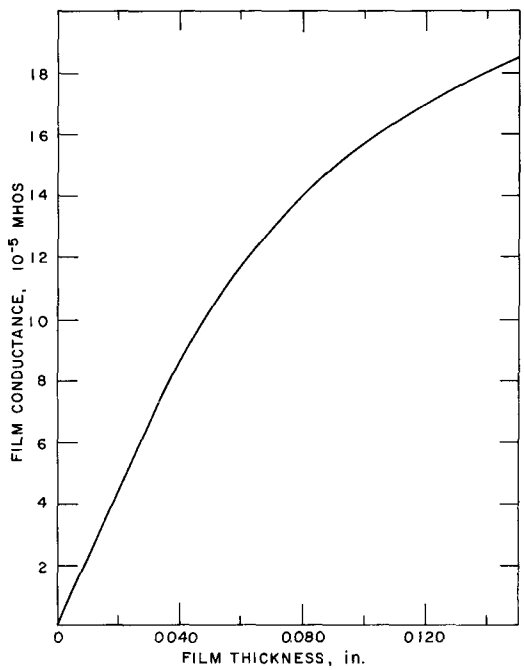

Fig. 10. Calibration Curve for the Conductance-probes Method

Before water was introduced into the calibration cell, a zero reading was taken on the dial indicator. As noted above, the dial indicator read correctly to within 0.001 in. Figure 10, a typical calibration curve, shows that the variation of C with t was nonlinear at large values of t.

b. Needle-contact Probe. The needle-contact-probe method consists of bringing a needle up to the surface of the film and measuring the distance from the tip of the needle to the wall upon contact with the film. This technique has been used by many investigators, for example, McManus,[36] Hewitt, King, and Lovegrove,[27] and Hilding and Coogan.[25]

Figure 11 is a photograph of the needle-contact probe. The needle was fabricated from a 6-in. length of 0.024-in. spring steel. The tip, approximately 1/4 in. long, was ground and polished to a point. The longer segment of the needle was encased in a Teflon sleeve to provide electrical insulation and fitted into a $3\frac{3}{8}$-in.-long piece of 1/8-in.-diam stainless steel tubing. At the end of the tubing opposite the point, the probe was bent to a right angle and mechanically fixed. The needle tip was then brush-coated with three applications of silicone varnish and cured at approximately 400°F

for 1 hr after each coating. The varnish sealed and covered the probe to approximately 0.001 in. of the point. Then the probe was installed in a Swagelock fitting. At the end of the fitting, a brass sleeve was bored to a 0.26-in. diameter and was concentrically located and soldered to the fitting, which was also bored to a 0.26-in. diameter. The sleeve length was 1/8 in. An identical sleeve and an O-ring were located in the fitting ferrule area. These guides ensured a true vertical travel of the probe. The spring between the fitting nut and a collar at the end of the tubing provided a tension against the probe.

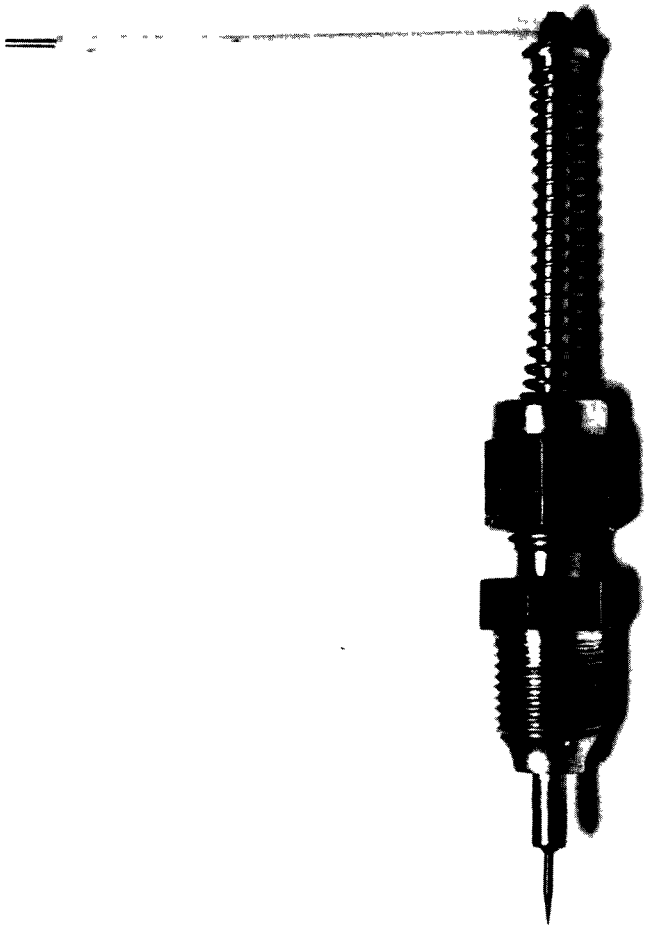

112-9803

Fig. 11. Needle-contact Probe

When the interface between the gas and water was wavy, first contact was with the crests of the waves. Continuous contact with the film did not occur until the troughs of the waves were being touched. To establish the temporal mean thickness, the method of relative contact time suggested by McManus[36] was used. McManus defined the temporal mean thickness as "the distance from the tube wall where a line in the axial direction would have half its length in the water and half its length in the air." That is, at a given distance from the wall for some unit of time, the needle would be in contact with the film half the time and in contact with the gas half the time.

To measure the relative contact time, the needle-contact probe was made part of a series dc circuit containing a Simpson 25-μAmp current meter of the d'Arsonval type, a 7.5-V battery, and a decade box. The decade box was used to set an upper limit on the dc current compatible with full-scale deflection of the current meter. This circuit is shown schematically in Fig. 12. When the needle was not in contact with the film, no current flowed in the circuit. As the needle penetrated the waves on the film surface, current flowed through the circuit on an interrupted basis. The current was continuous when the needle touched the troughs of the waves. McManus considered the temporal mean thickness as the location at which the current reading was 50% of the value measured when the needle touched the troughs of the waves. The following procedure was used to measure the film thickness: The needle was lowered until it came into contact with the troughs of the waves. The current reading on the meter was then noted. Then the needle was withdrawn until the current reading reached 50% of the aforementioned value, marking the location of the mean film thickness. Finally, the needle was withdrawn into the upper surface of the test section so that subsequent measurements were not affected.

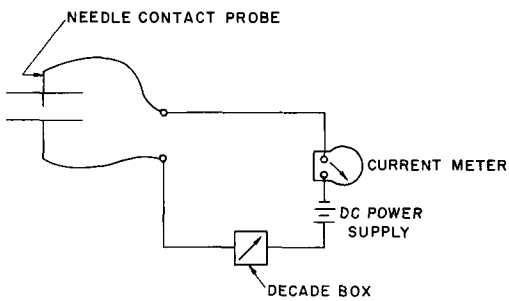

Fig. 12. Circuit for Needle-contact-probe Method

Another method using the needle-contact probe has been used to measure the temporal mean film thickness. Hewitt, King, and Lovegrove[27] and Hilding and Coogan[25] counted the number of times that the needle is alternately in contact with the gas or water in a given interval of time. With this frequency plotted against position from the wall, the location at which the frequency was a maximum was considered to be the temporal mean film thickness. In both instances, these measurements were compared with the method of McManus, and good agreement between the measurements was noted. The method of McManus was used in this research since it involved much less time in making a given measurement.

The crests and troughs of the waves were measured by monitoring the voltage drop across the needle-contact probe on a Tektronix oscilloscope (Type 502).

The accuracy of the needle-contact probe is discussed in Appendix A.

The measurement of mean film thickness with the needle-contact probe necessitated finding the micrometer setting when the needle was in contact with the lower surface of the test section. This was easily accomplished because of the differences in the electrical conductivity of the steam, water, and lower surface of the test section. The zero reading was

taken when the temperature of the test section, with both steam and water flowing, reached a steady state. The oscilloscope was then connected in parallel between the needle-contact probe and the lower surface of the test section. The initial voltage reading with the probe immersed in the steam was essentially the open-circuit voltage due to the very small electrical conductivity of the steam. When the probe was lowered into the water, the voltage drop across the probe diminished because of the finite electrical conductivity of the water. When the probe came in contact with the lower surface, the voltage drop across the probe decreased sharply because of the relatively large electrical conductivity of the lower surface of the test section. At this point, the micrometer was read. The micrometer setting, with the probe in contact with the lower surface of the test section, was read for each of the eight probes in the steam-water test section. The procedure for the needle-contact probe in the air-water test sections was similar.

c. Discussion. The conductance-probe method has the advantage of being an indirect method of obtaining local film thicknesses. It can also provide information regarding the instantaneous variation of film thickness with time. However, this method requires a calibration to establish the relationship between the conductance of the film, C, and the film thickness, t. Except for small values of t, the variation of C versus t is nonlinear. In addition, the calibration would exhibit a dependency on temperature. Since the needle-contact-probe method does not have these disadvantages, it was chosen to measure film thickness in the steam-water experiments. However, this choice sacrificed the ability to obtain indirect measurements of film thickness and information regarding the instantaneous variation of film thickness with time.

3. Measurement of Temperatures, Pressures, and Flowrates

In the steam-water tests, the thermocouples in the test facility and test section were measured via the reference ice junction by using a Hewlett-Packard integrating DVM (Model 2401C). The integrating time normally chosen was 10 sec.

The sheathed thermocouples were calibrated in a temperature-controlled oil bath. A resistance thermometer, calibrated by the National Bureau of Standards, was used to measure the temperature of the oil bath. The temperature of the oil bath was varied from 70 to 240°F. The resulting calibration was fitted by a quadratic least-squares equation with a maximum error of less than 0.2°F. Since the surface thermocouples could not be calibrated in place in the test section, two thermocouples were randomly chosen from the set fabricated for the test section. These couples were calibrated the same way as noted above. Over the temperature range of 70-240°F, the agreement was within 0.1°F. The resulting calibration was fitted by a quadratic least-squares equation with a maximum error of 0.1°F. As an additional qualitative precaution, the surface thermocouples were checked in

place in the test section when the experimental facility was at room temperature. The maximum difference in temperature between the surface thermocouples was 1/3°F.

The thermocouples used in the air-water experiments were iron-constantan. The temperature was measured with a potentiometer through an ice junction. At room temperature, these thermocouples were within ±1°F of a standard laboratory mercury-in-glass thermometer.

The steam pressure at the exit of the calming section was measured with a 0-50-psig Heise gauge. The gauge was calibrated, and the maximum error was 0.1 psig.

All the orifice plates used were of the knife-edged type, constructed and mounted according to the standards given by Grace and Lapple.[21] The water orifice plates were calibrated by weighing the discharge over a given time interval. The air and steam orifice plates had been similarly calibrated using water whose orifice Reynolds number was varied over the range of steam and air orifice Reynolds numbers of interest.

The standard equation used to calculate the mass flowrate of fluid through an orifice plate is given by

$$W = A_{or} C_{or} \left[\frac{2 g_c \rho_{avg} \Delta P_{or}}{1 - \beta_{or}^4} \right]^{1/2} . \qquad (160)$$

The orifice coefficient, C_{or}, can be selected from the data of Grace and Lapple. For example, this equation predicted flowrates within 2% of the measured flowrates for an orifice with $\beta_{or} = 0.125$ and $C_{or} = 0.61$.

4. Experimental Procedure

a. Air-Water Experiments. The liquid system was filled with softened water until the water level in the separator was approximately 6 in. below the test section. The pump was then started, and the water-control valve opened, permitting flow in the test section. The manometer connected to the water-measuring orifice was then bled. The air-control valve was opened, and air was introduced into the test section. The manometer connected to the air orifice was then opened.

The only energy input to the water was through losses in the pump. As the water was heated, the heat-exchanger coolant-control valve was adjusted to maintain the temperature of the water in the test section at room temperature. The initial heat-up time of the water varied, depending on the temperature of the laboratory service supply. An average heat-up time was 2 hr.

The digital voltmeter used in the conductance-probes measurement method was left on overnight. This allowed stabilization, virtually eliminating drift. Each morning, however, the calibration of the digital voltmeter was checked.

Each day, a sample of water was drawn from the separator and introduced into the calibration cell. The calibration was performed over 0.01-in. intervals. A thermocouple was inserted into the calibration cell, and the temperature of the water measured and compared to the temperature measured at the exit of the test section.

Each test started with setting the air and water flowrates. The thermocouple at the exit of the test section was checked to see if the temperature had changed. The appropriate voltage drops for the various pairs of probes were measured by the DVM over a 10-sec integrating interval. At the end of each test, the flowrate was again checked. A typical test took 20 min.

b. Steam-Water Experiments. The liquid system was filled with softened water until the water level in the separator was approximately 6 in. below the test section. The pump was then turned on and the water-control valve opened, permitting flow in the test section. The manometer connected to the water-measuring orifice was then bled. The steam-supply line was then bled to remove any condensate, and the steam-control valve was opened, introducing steam into the test section. The manometer connected to the steam orifice was then opened. Before any data were taken, the water in the liquid system was allowed to heat up to approximately the saturation temperature corresponding to the pressure in the test section. This allowed any air dissolved in the water to be released and purged from the system through the steam-discharge line.

At the start of each test, the coolant-control valve in the heat exchanger was adjusted so that the temperature of the water in the injector was set at the desired value of subcooling. The system was then allowed to reach steady state, taking 10-30 min. When the system reached steady state, as evidenced by constant temperature in the test section, a test was begun.

The steam and water flowrates were then measured. The barometric pressure was read on a calibrated absolute-pressure gauge. The temperature and pressure of the steam at the exit of the calming section was then read to ensure that the steam was not superheated. The surface temperatures in the test section were then measured by the DVM with a 10-sec integrating period. The injector temperature and the exit-steam temperature were measured. The needle-contact probes were lowered to measure the film thickness, starting at the exit of the test section and proceeding to the inlet. After each measurement, the needle was withdrawn

into the upper surface so that subsequent measurements were not disrupted. At the end of each test, the steam and water flowrates were again measured. The data-acquisition time varied between 30 and 45 min.

5. Preliminary Experiments

a. Dye-injection Studies. To check the assumption that the flow in the film was two-dimensional, dye-injection studies were carried out as part of the air-water experiments. Dye (blue ink) was injected into the water film through the needles imbedded in the lower surface of the air-water test section. (The location of these needles has been described previously.) These studies were carried out over various combinations of high and low water and air flowrates. It was visually observed that the path of the dye from the various injection points was parallel to the centerline of the test section. These results indicated that the mass flowrate of water per unit length of wetted perimeter remained constant in the direction normal to the flow as the water progressed through the test section. Since the aspect ratio of the slit was approximately 100:1, the mass flowrate of water per unit length of wetted perimeter was initially expected to be the same across the width of the slit. Thus, the assumption of two-dimensional flow in the film appeared to be reasonable.

b. Film-thickness Variation Normal to the Flow. As part of the air-water tests, the film-thickness variation normal to the direction of flow was measured by the five pairs of conductance probes, normal to the direction of flow at a distance of 13 in. from the exit plane of the injector. For air velocities, an order of magnitude larger than the water velocity, the average variation in film thickness from the centerline of the test section to 1.25 in. on either side of the centerline, was less than 10%. This result indicated that the flow in the central 40% of the channel was relatively independent of side-wall effects and, therefore, the effect of the side walls on data taken along the centerline of the test section would be small. Cohen[9] found the air velocity in the central portion of a rectangular conduit of 12:1 aspect ratio to be essentially constant over the central 25% of the channel. In this research, the aspect ratio for the air flow was approximately 10:1; thus, Cohen's result is assumed applicable, further confirming the assumption of two-dimensional flow.

c. Comparison of Film-thickness Measurement Methods. In the air-water test section, a needle-contact probe was mounted directly above a pair of conductance probes. To gain confidence in these techniques for measuring temporal mean film thicknesses, data were taken with widely varying air and water flowrates. Table I summarizes these data. Included in this table are the peaks of the highest waves and the troughs of the deepest waves as measured by the needle-contact probe. The agreement represented by these data appears quite good.

TABLE I. Comparison of Film-thickness Measurements Using the Conductance-probes Method and the Needle-contact-probe Method

Film Thickness, in.			
Conductivity Probes	Needle Contact	Peaks	Troughs
0.121	0.121	No waves	
0.080	0.080	No waves	
0.072	0.071	No waves	
0.0635	0.062	0.072	0.037
0.0385	0.042	0.076	0.010
0.033	0.035	0.076	0.010
0.030	0.029	0.105	0.007
0.061	0.062	0.088	0.035

IV. RESULTS AND DISCUSSION

A. Air-Water Experiment

The air-water experiments were undertaken to assess the applicability of the analytical model developed for the stratified turbulent flow of a gas phase over a horizontal film. Of particular interest was whether the assumed shear-stress models yielded predictions consistent with the actual physical phenomena. The shear-stress models have been tested mainly by experiments in which the changes in convective momentum terms of the governing equations were negligible or zero. The opposite is true in this research, where dt/dx is not equal to zero and an additional momentum term, which represents the hydrostatic pressure variation in the film, is included. Since the analytical model for film condensation embodied most of the assumptions made for the model of the two-component flow, the success of the film-condensation model is predicated on the establishment of the physical consistency of the two-component model with the air-water experiments.

This chapter compares the model for two-component flow and the air-water experiments. A flow chart delineating the calculational procedure used in the computer program for the model is given in Appendix B.

The accuracy of the film-thickness measurements presented for the air-water experiments is discussed in Appendix A.

1. Wall-layer Model of the Film

In the development of the model for two-component flow, it was assumed that the wall shear stress in the film could be determined by using the concept of the "wall-layer" model for film flow. Since Hershman had shown the wall-layer model to be applicable to horizontal films up to Re_ℓ of approximately 600, additional confirmation was sought for Re_ℓ greater than 600.

To isolate the effect of the wall shear stress on the film from the effects of interface shear stress and pressure gradient in the air stream, data were taken with $W_a = 0$. In effect, this meant that the momentum change of the film was a result of the wall shear stress and the static pressure gradient caused by the hydrostatic term. Figure 13 compares these data to the predictions from the model of two-component flow. The agreement between the data and the predictions of the model is good for the range of Re_ℓ from 1000 to 8000. In this range of Re_ℓ, the film is turbulent. This result is particularly interesting since the wall-layer model has been used principally for films flowing under the influence of a high-velocity gas stream.

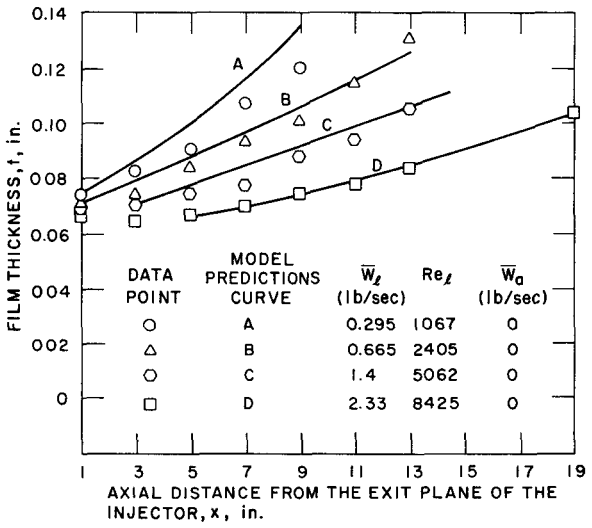

Fig. 13
Comparison of Model Predictions of Film Thickness with Data to Test the Applicability of the Wall-layer Model for Film Flow

The discrepancy between the predictions of the model and the data for $Re_\ell = 1067$ can be discussed by writing the convective-momentum term and the hydrostatic term of Eq. 96 as

$$\left(- \frac{W_\ell^2}{\rho_\ell^2 t^2} + g_y t \right) \frac{dt}{dx}.$$

Examination of the term in parentheses reveals that, for a given value of W_ℓ, there are values of t for which the difference between the two terms in parentheses is small. Since it was assumed in the development of Eq. 96 that

$$\overline{u_\ell^2} = \overline{u}_\ell^2,$$

it is clear that when the aforementioned difference is small, the approximation should be replaced by

$$\overline{u_\ell^2} = \eta \overline{u}_\ell^2. \tag{161}$$

In effect, this result points out that the "nonflatness" of the velocity profile cannot always be neglected.

For example, in the experiments depicted in Fig. 13, where $W_a = 0$, the effect of a "quiescent" ambient was to exert a retarding influence on the film momentum near the surface. The result of this influence would be to make η different from unity. Thus, the assumption that $\eta = 1$ underestimates the film momentum, and when the hydrostatic term in the momentum equation becomes comparable to the convective-momentum term, the analytical model predicts a deceleration of the film that is too large. This was the case for $Re_\ell = 1067$. For the other values of Re_ℓ, the film momentum was large enough so that the assumption that $\eta = 1$ had no noticeable effect.

However, in contrast to the case where $W_a = 0$, the effect of gas flowrates different from zero, especially when waves are present on the gas-film interface, is to promote turbulent mixing in the film, thereby reducing the velocity gradient across the film so that the value of η will approach unity. In addition, another effect of a concurrent gas flow is to reduce the magnitude of a positive gradient of film thickness with respect to axial length. Thus, the difference between the terms in parentheses will increase, further reducing the effect of the approximation for η on the change in film momentum. This will be verified in Section 2 below.

Referring again to Fig. 13, we see that the initial film thickness used in the model was taken at successively larger values of x for successively larger values of Re_ℓ. The film thickness from the injector to the point at which the initial film thickness was chosen is essentially constant. Since the film thickness remains approximately constant, it is inferred from Eq. 69 that the momentum of the film remains constant. However, the existence of the wall shear stress precludes such a conclusion.

To explain this apparent inconsistency, possible ramifications of the assumption that the von Karman universal velocity distribution is applicable to the film are noted. In analogy with pipe flow, the universal distribution is valid only when the velocity profile has become fully developed, i.e., away from the region of entrance effects. According to the wall-layer model, this implies that the von Karman distribution will apply to the film at some distance from the exit plane of the injector where entrance effects have become negligible. Since the analytical model successfully predicts the variation of t with x downstream from the region in which the film is essentially constant, it is tentatively concluded that entrance effects are responsible for the constancy of film thickness. That is, the velocity profile in the film in the region near the exit plane of the injector must change from a profile indicative of flow in the slit of the injector to the von Karman universal velocity distribution. Since the value of η is variable, a change in the momentum of the film is possible, when $dt/dx \simeq 0$, by virtue of the change of the velocity profile. Thus, in the entrance region, the resulting loss of momentum to the wall by shear stress is possibly supplied by the film-momentum change resulting from the velocity-profile variation. More definite conclusions regarding the entrance region of the film require detailed consideration of the effects of the geometry at the exit plane of the injector, together with measurements of the velocity profile in the film. These considerations were not included in this research.

Therefore, since the analytic model developed in this report does not consider the possible variation of the film velocity profile, the first meaningful data point chosen as an initial condition for the model is the point at which the film thickness exhibits a finite gradient.

2. Experiments on the Turbulent Flow of Air and Water

This section compares the predictions of the model for the two-component flow of turbulent gas and liquid phases data taken for the flow of air over water.

Since the range of critical Reynolds numbers for film flow, as cited by Fulford,[19] extends from 240 to 400, the range of Re_ℓ in this set of experiments was varied from 477 to 5062.

Of principal interest was the range of Re_a for which the air-water interface was characterized by three-dimensional disturbances. Wallis,[50] in experiments on the horizontal concurrent flow of air over water, visually determined the velocity at which a three-dimensional (pebbly) structure was present at the air-water interface. The air velocity for the onset of these disturbances was approximately 15-17 ft/sec. For the experiments reported here, this range of velocities corresponds approximately to a value of Re_a of 7000. Visual observation through the Lucite test section in these experiments confirmed the presence of a pebbly structure at this Reynolds number. The air is turbulent at this Reynolds number, and since this value of Re_a corresponds to the lower limit at which Eq. 107 is valid, it was selected as the minimum air Reynolds number in this set of experiments.

As the air velocity is increased, the three-dimensional waves at the interface undergo a transition to the roll-wave regime. According to the data of Wallis,[50] the onset of roll waves occurred at an air velocity of approximately 35-38 ft/sec. The lower velocity corresponds to Re_a of approximately 19,000 for the experiments reported here. The proposed interfacial friction-factor correlation, Eq. 110, was tested in the roll-wave regime in the range of Re_a from 19,000 to 23,500.

Wallis also found that entrainment occurred at a velocity of 53-58 ft/sec. As determined by Van Rossum,[48] this result is compatible with an onset velocity of 59 ft/sec. Since the largest air velocity in these experiments was approximately 44 ft/sec (Re_a = 23,500), the problem of entrainment was avoided.

Figures 14-18 compare the predictions of the model and the experimental data. In Figs. 14-17, the mass flowrate of air was varied while the mass flowrate of water was kept approximately constant. Alternately, in Fig. 18, the air velocity was kept approximately constant at a value such that the interface disturbances were in the roll-wave regime and the water flowrate was varied. The overall agreement between the predictions of the model and the data is excellent.

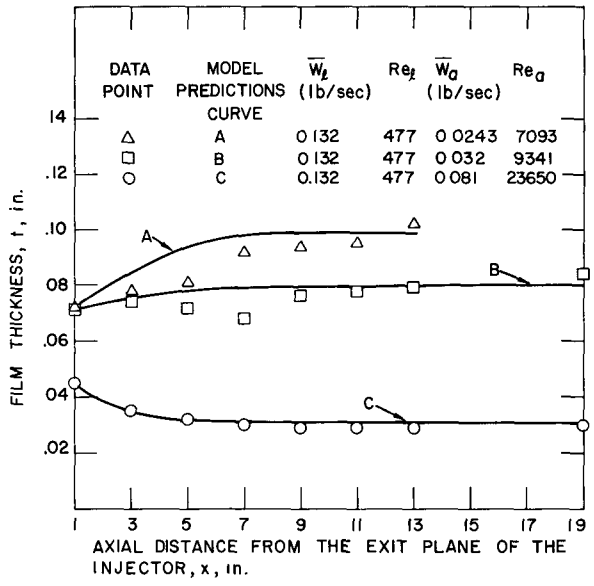

Fig. 14. Comparison of Model Predictions of Film Thickness with Data, for $\overline{W}_\ell$ = 0.132 lb/sec

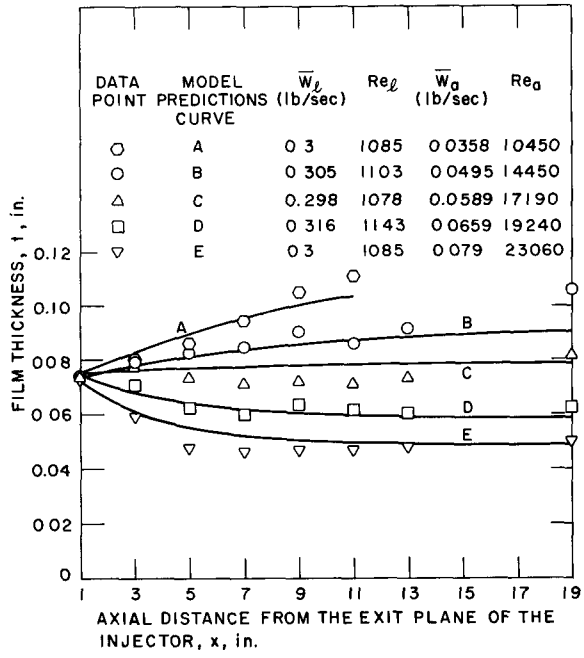

Fig. 15. Comparison of Model Predictions of Film Thickness with Data, for $\overline{W}_\ell \simeq$ 0.3 lb/sec

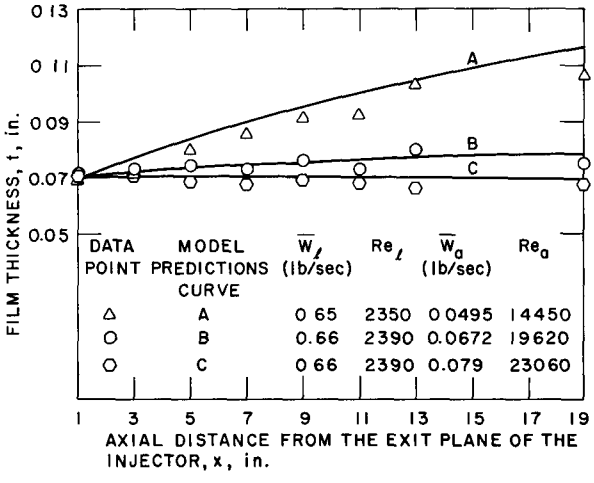

Fig. 16. Comparison of Model Predictions of Film Thickness with Data, for $\overline{W}_\ell$ = 0.66 lb/sec

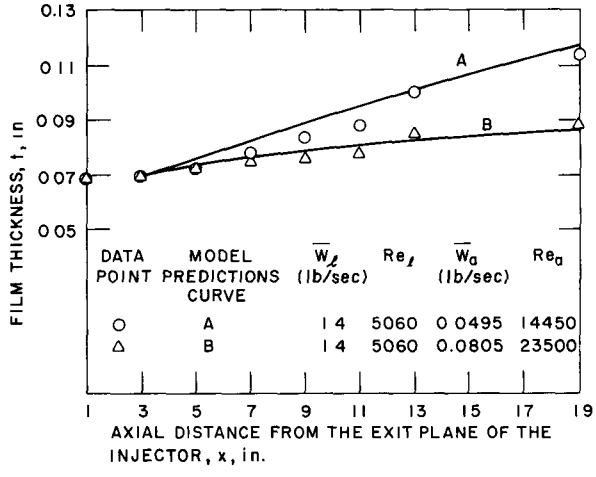

Fig. 17. Comparison of Model Predictions of Film Thickness with Data, for $\overline{W}_\ell$ = 1.4 lb/sec

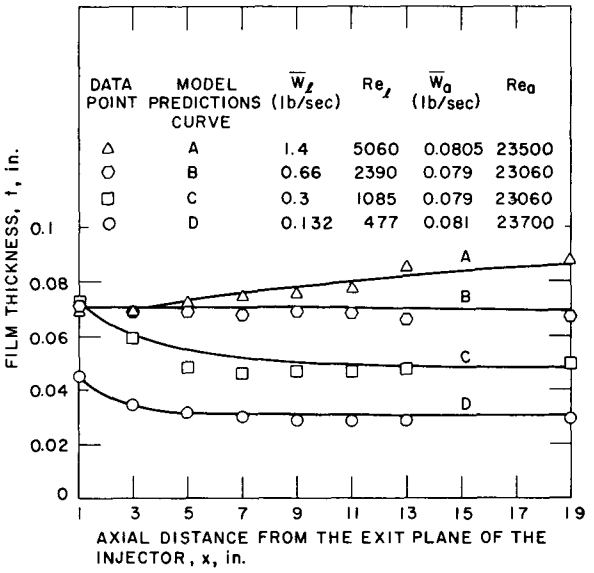

Fig. 18. Comparison of Model Predictions of Film Thickness with Data, for $\overline{W}_a \simeq 0.08$ lb/sec

Although the wave crests and troughs were not measured, except for those results presented in Table I, monitoring the conductance-probes signal on an oscilloscope revealed that the waves deeply penetrated the film. Also, the frequency of the disturbances decreased in the direction of flow. These observations emphasized the complex nature of the interfacial disturbances. Thus, the success of the simple interfacial friction-factor correlation for three-dimensional disturbances is gratifying since it affords a convenient method of evaluating the interface shear stress without referring to the details of the interfacial structure.

In the roll-wave flow regime, the assumed correlation for the interfacial friction factor for three-dimensional disturbances was not applicable. However, by trial and error the following simple correlation, which was again found to be independent of Re_a, was established:

$$f_i = 5.1 \cdot Re_\ell \cdot 10^{-5} + 0.056. \qquad (162)$$

Figure 19 shows the friction-factor correlations for the three-dimensional and roll-wall regimes. The fact that the friction factor at the interface is substantially increased by a factor of approximately 3 for $Re_\ell = 5062$ may be attributed to the change in the character of the disturbances.

Since the waves greatly increase the complexity of the fluid mechanics, it is concluded that the model of two-component flow developed in this report with the aid of various simplifying assumptions has been justified. It is also concluded that the simple correlations proposed for the interfacial friction factor are useful in describing the momentum transferred from the gas to the liquid phase in the presence of waves.

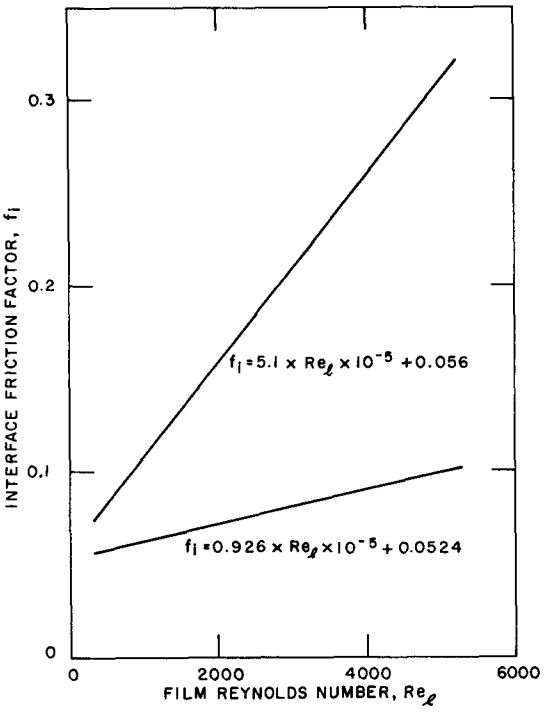

Fig. 19. Interface Friction Factors for the Three-dimensional and Roll-wave Regimes

3. Experiments on Conditions for Laminar Flow in the Film

According to Fulford's criterion, for Re_ℓ less than 400 but greater than 240, the film may be either laminar or turbulent. To test this criterion, additional experiments were made for $Re_\ell = 300$. Figure 20 compares the predictions of the model and the data. The film was assumed turbulent in all three experiments. Good agreement is noted, except at $Re_a = 7000$, where the model predicts film deceleration at a rate greater than what was actually observed. The computer results revealed that the convective-momentum term was approximately equal to the hydrostatic term. This suggested that the value of η in Eq. 161 should not be unity. Since Re_ℓ is in the range where the film can be laminar, a value of $\eta = 1.3$ (which is characteristic of a laminar-film velocity profile) was substituted into the model for further calculation. To be compatible with the assumption of a laminar film, the relationship for the wall shear stress in the film was modified. From Eqs. 65 and 69, the wall shear stress can be estimated from

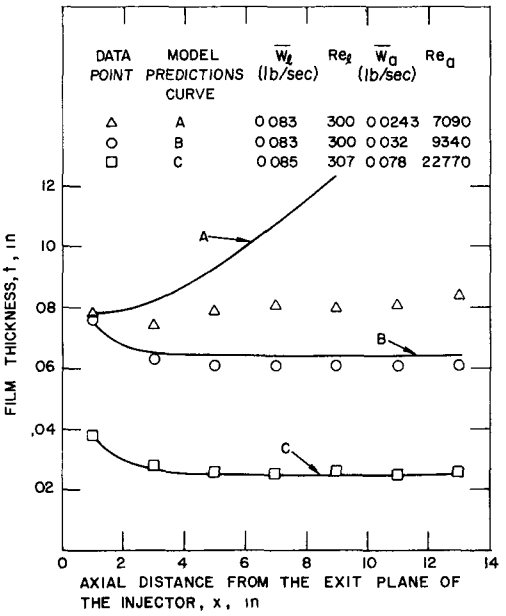

Fig. 20. Comparison of Model Predictions of Film Thickness with Data for a Critical Film Reynolds Number

$$\tau_0 = \frac{6}{Re_\ell} \frac{b + t}{3b + t} \frac{W_\ell^2}{\rho_\ell t^2}. \qquad (163)$$

The predictions of the model for both laminar and turbulent film are plotted together with the data in Fig. 21. Also included in this figure are data for films where Re_ℓ are above and below the range of critical Reynolds numbers. Thus, for Re_ℓ above the range of critical Reynolds numbers, the film behaves turbulently. For Re_ℓ below the range of critical Reynolds, the film exhibits a laminar behavior. For Re_ℓ within the range of critical Reynolds numbers, the film behaves turbulently for high air velocities, but as the influence of the air is reduced, laminar-type behavior is noted. This implies that for the Re_ℓ flows in the range of critical Re_ℓ, the value of η varies from 1 to 1.3 as a function of Re_a.

B. Steam-Water Experiments

The purpose of the steam-water experiments was to test the validity of the model developed for film condensation. Of particular interest was verification of the effect of mass transfer on the interfacial shear stress and of the constancy of the Stanton number.

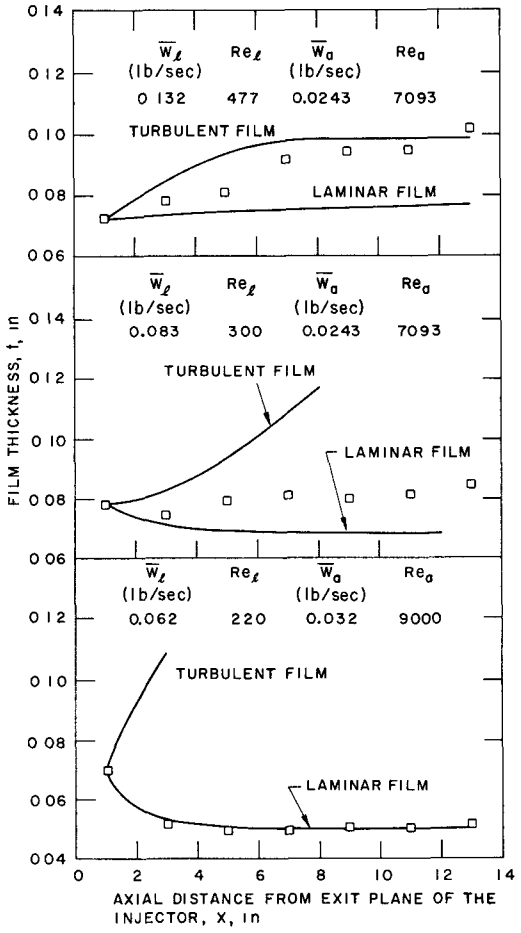

Fig. 21. Comparison of Model Predictions for Laminar and Turbulent Films vs. Data

Since it was desired to evaluate the ability of the model to predict film condensation when the interfacial structure was three-dimensional, the inlet steam Reynolds number was varied from approximately 14,000 to 17,500. This ensured that the decrease in Re_s through the test section, by virtue of condensation, was small enough so that three-dimensional waves were in the entire test section. As discussed in Section III.B.1.e, the steam at the inlet to the test section was saturated and had a quality above 97%. The inlet film Reynolds number was varied from approximately 250 (in the range of critical Reynolds number) to 1800. The effects of condensation rate were observed by varying the inlet subcooling of the water from approximately 70°F (limit set by cooling capacity of the heat exchanger) to 200°F (limit set by heat losses from the experimental facility).

1. Evaluation of the Stanton Number

In the development of the expression for the condensing heat-transfer coefficient, it was shown that the Stanton number, St_ℓ, should be constant. This result can be tested with the aid of

$$St_\ell = t \frac{dT_0}{dx} \frac{1}{\left[1 + \frac{T_s - T_0}{h_{fg}}\right] (T_s - T_0)}. \qquad (156)$$

Table II lists data from three steam-water experiments used in the evaluation of the Stanton number. Over the range of data listed, Re_ℓ varied from 340 to 1800 and Re_s varied from 13,000 to 17,500. These data were selected since the subcooling in the film was large and, therefore, the effects of any errors in temperature measurements were minimized. In the range of data presented, dT_0/dx and $T_s - T_0$ are each larger than 10°F/in. and 10°F.

TABLE II. Experimental Data Used to Evaluate the Stanton Number, St_ℓ

$\overline{W}_\ell$, lb/sec:		0.057		0.099		0.192		
$\overline{W}_s$, lb/sec:		0.039		0.04		0.04		
T_s, °F:		211		211		211		
x, in.	t, in.	T_0, °F	x, in.	t, in.	T_0, °F	x, in.	t, in.	T_0, °F
0		70.5	0		70.3	0.375		116.8
0.375		100.9	0.375		84.7	1.375	0.039	129.1
1.375	0.013	128.2	1.375	0.019	112.9	2.375		143.6
2.375		162.9	2.375		144.6	3.375	0.030	155.1
3.375	0.017	184.5	3.375	0.021	168.5	4.375		169
4.375		194.7	4.375		183.3			
5.375	0.017		5.375	0.024	191.6	5.375	0.029	177.6
7.375	0.028		7.375	0.030		7.375	0.036	

To further minimize possible errors in the film-thickness and temperature measurements, the data in Table II were fitted by cubic least-squares equations. The least-squares equation for T_0 was differentiated with respect to x, and the gradient of T_0 was obtained. These equations were substituted into Eq. 156, and the Stanton number was evaluated for each set of test data from x = 1.4 in. to x = 4.4 in. The value of x = 1.4 in. was selected to correspond approximately to the location of the first film-thickness measurement. The value of x = 4.4 in. was dictated by the desire of keeping $dT_0/dx > 10°F/in.$ The Stanton number was evaluated at 0.1-in. intervals for each set of data; the average Stanton number for 90 determinations was found to be 0.0073. Although the range of Stanton numbers calculated varied from approximately 0.0055 to 0.01, over 70% of the determinations were between 0.006 and 0.008.

The variation of the Stanton number is within the range of possible experimental errors in the determination of the film thickness and temperature. For example, in Appendix A it is stated that the error in the film-thickness measurement could be as large as ±0.002 in. For the data in Table II, this represents a variation in the measured film thickness of ±15% for t = 0.013 in. to ±5% for t = 0.039 in. Since St_ℓ is directly proportional to t, this measurement error is a possible explanation for the indicated variation in the calculation.

For the three experiments under consideration, it is concluded that the Stanton number is approximately constant. Additional confirmation of this result will be offered in Section 2 below, where the predictions of the model of film condensation are compared to the data from all the steam-water experiments.

2. Comparison of the Model of Film Condensation with Experiment

In this section, the predictions of the model of film condensation are compared to the data taken for the steam-water experiments. The measured film thickness, t, and surface temperature, T_0, and those values calculated using the model are to be compared to justify the models chosen for the interfacial friction factor, λ_i^*, and the heat-transfer coefficient, h. Also included in the presentation of film thickness are some of the crests of the highest waves and troughs of the deepest waves for the three-dimensional waves encountered in these experiments. Since they are not explicitly considered in the model, their value lies in emphasizing the complexity of the phenomenon in question in comparison to the relative simplicity of the model chosen to represent their effects.

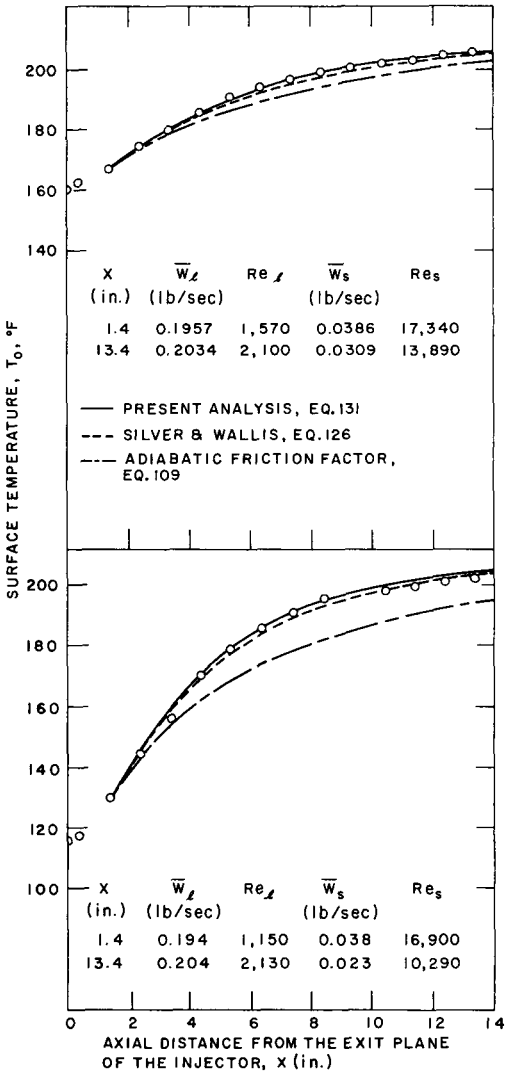

Fig. 22. Effect of Model of Interface Shear Stress on Predictions of Film Surface Temperature

a. The Effect of Condensation on the Interfacial Shear Stress. To illustrate the effect of condensation on the interfacial shear stress, several methods for determining τ_i were tested against data. In particular, the model of Silver and Wallis (Eq. 126), the model proposed in this report (Eq. 131), and the model used in the air-water experiments (Eq. 110), were used in predicting the temperature, T_0, and the film thickness, t, for two different experiments. Figures 22 and 23 show the results. The predictions of film thickness versus the data indicate that the calculated amount of interfacial momentum transferred using the two-component friction-factor correlation is underestimated. Instead of manifesting the initial acceleration in the film that results from condensing high-velocity vapor, the model predicts a deceleration of the film. However, the models that include the effect of momentum transfer via mass transfer predict the trends of the data rather well.

In both experiments under consideration, the model proposed in this report (Eq. 131) agrees more closely with the film-thickness data than the model of Silver and Wallis. A possible explanation of this result is that, in their derivation of Eq. 126, Silver and Wallis

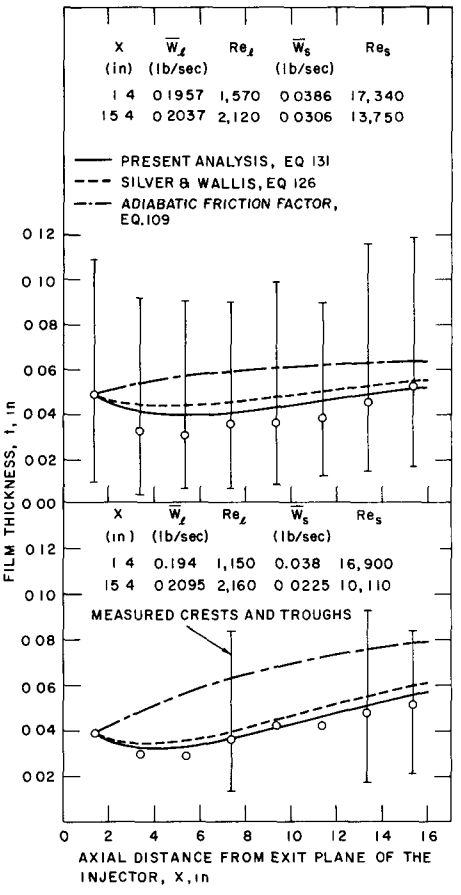

Fig. 23. Effect of Model of Interface Shear Stress on Predictions of Film Thickness

used a simplified theory of the actual phenomenon, neglecting the effects of waves and linear motion of the surface. Although Eq. 131 is not derived from theory, it is consistent with the manner in which Carpenter and Colburn represented the total momentum transferred across the vapor-liquid interface and, since it more closely predicts the momentum variation in the film, its use in the model of film condensation is justified.

Considering the predictions of surface temperature, T_0, versus the data for the various interface friction-factor relationships, Eqs. 126 and 131 agree rather well with the experiment. A further effect of using the two-component friction factor is also evident. The underestimation of the momentum transferred to the film results in an apparent increase in film thickness, which in turn increases the condensing heat-transfer resistance. The overall effect is a decrease in the condensation rate.

b. Comparison of the Model Predictions and Data. To compare the model predictions and the data, experiments were performed varying the inlet-film subcooling and the inlet-mass flowrates of steam and water over the ranges indicated earlier. Figures 24-37 show the results. In general, the agreement is excellent, especially considering the relationship of the waves to the measured film thickness. To put the waves into physical perspective, the characteristic wavelength and the frequency of the waves must be discussed. Although these measurements were not possible in this research, reference can be made to the work of Cohen[9] in which he determined the wavelength and wave velocity at the inception of three-dimensional disturbances on water films. For Re_ℓ = 590, he measured a wave velocity of 1.03 ft/sec and a wavelength of 0.39 in. This corresponds to a frequency of approximately 30 Hz. If these data to some extent represent the three-dimensional disturbances in the steam-water experiments, the assumptions made in Chapter II appear to be reasonable. That is, the notion that the waves tend to act as an effective large-scale eddy motion, which tends to minimize the temperature gradients normal to the flow, is more viable. In addition, this also lends credence to the model proposed for the condensing heat-transfer coefficient. Further justification for this model results from the excellent agreement of the predicted temperature variation along the surface with the measured values. Since Re_ℓ

varied from 260 to 2100, Re_s varied from 18,000 to 7,000, and Pr_ℓ varied from 4.5 to 1.75 in the experiments reported here, the aforementioned agreement also confirms the use of $St_\ell = 0.0073$ as determined in Section B.1 above.

The first meaningful film-thickness measurement was selected as the initial film thickness in the model. This initial film thickness did not always correspond to the first measured film thickness. As in the air-water experiments, the effect of an "entrance region" again appears. In the steam-water experiments, this "entrance region" is related to the assumption of a uniform temperature profile. In particular, the experimental manifestation of the entrance region is observed in the first few surface-temperature measurements. The measurements at $x = 0$ and $x = 3/8$ in. are generally the same. At higher liquid flowrates, the regions of this approximate constancy of surface temperature appear to increase in the direction of flow. The similarity between this result and the constancy observed in the film thickness in the air-water experiments is noted. This entrance region is apparently at least partly dependent on the steam flowrate. This is evidence by the fact that for $\overline{W}_\ell$ inlet approximately equal to 0.19 lb/sec, the entrance region diminishes from just under 3 in. to under 1 in. as the steam flowrate is increased from 0.032 to 0.04 lb/sec. As in the air-water case, the model of film condensation does not describe this region. Therefore, the first meaningful data point was selected at the location of a measured film thickness where the temperature gradient appeared to decrease monotonically.

In the experiments of Figs. 24-29, the initial subcooling in the film is varied for essentially constant inlet-steam and water flowrates. Since the condensation rate is proportional to the difference between the steam temperature and the film subcooling, the condensation rate is largest for the largest initial film subcooling. Since the momentum transferred to the film via the interface shear stress is proportional to the condensation rate, the acceleration would be the greatest in the film with the largest initial subcooling. This is reflected in the measurements of film thickness which show, in the first 7 in., successively smaller thicknesses at any x for successively larger amounts of initial film subcooling. This emphasizes the fact that the momentum transferred to the film via the interface shear stress must include the effects of condensation. As the film subcooling is reduced by condensation, the films that initially accelerated the most now exhibit the largest deceleration. This observation can be attributed to the fact that the films with large initial amounts of subcooling condense more of the steam flow than the lower subcooling films. Therefore, when the condensation rate becomes smaller due to the heating of the film by condensation, the interfacial shear stress, which is now essentially equal to the two-component shear stress, is smaller for those experiments in which the initial subcooling is largest. This allows the wall shear stress in the film to decelerate the film more effectively.

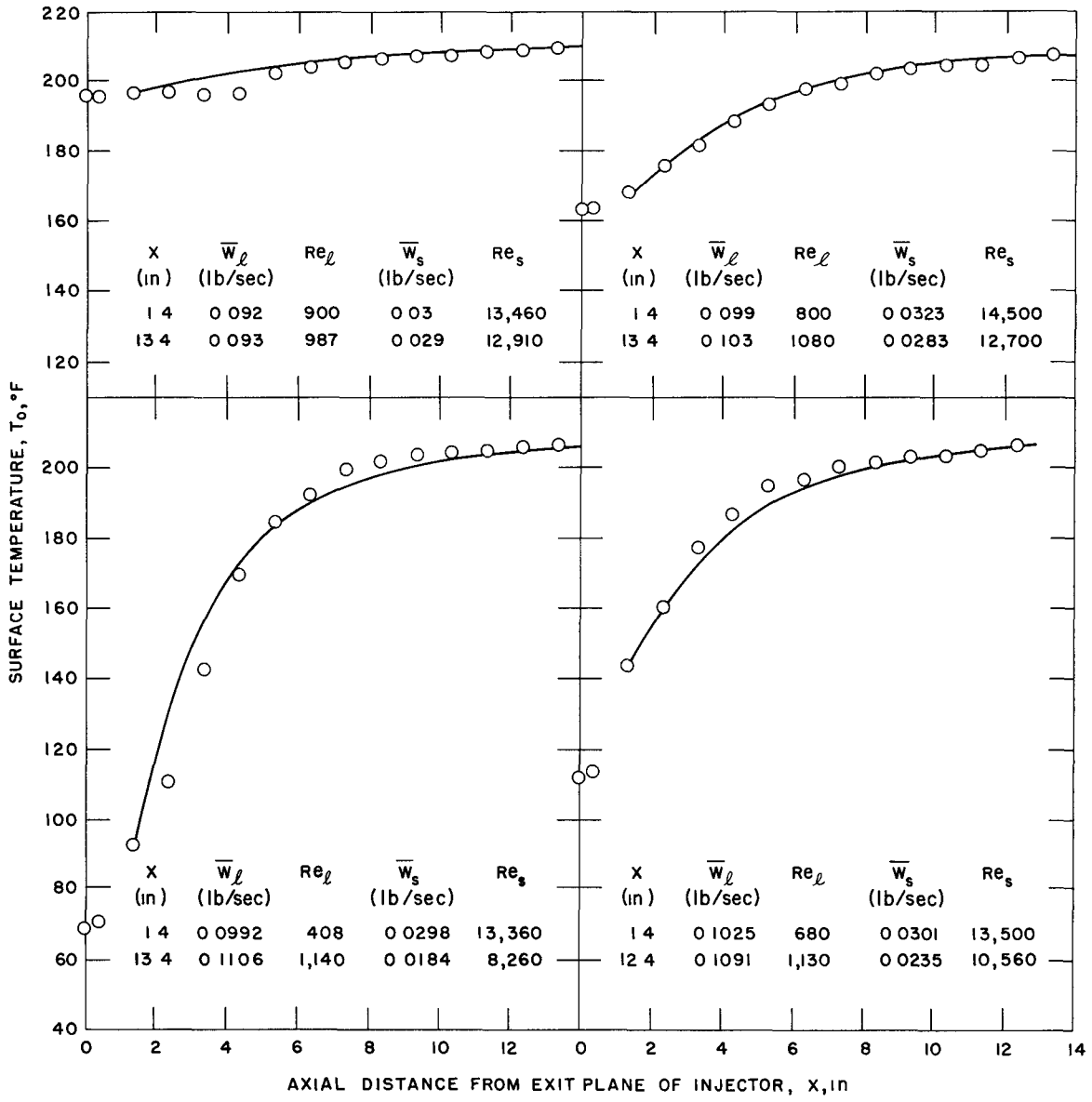

Fig 24 Comparison of Model Predictions of Surface Temperature vs. Data as a Function of Water Inlet Subcooling for $\overline{W}_\ell \simeq 0.1$ lb/sec, $\overline{W}_s \simeq 0.03$ lb/sec

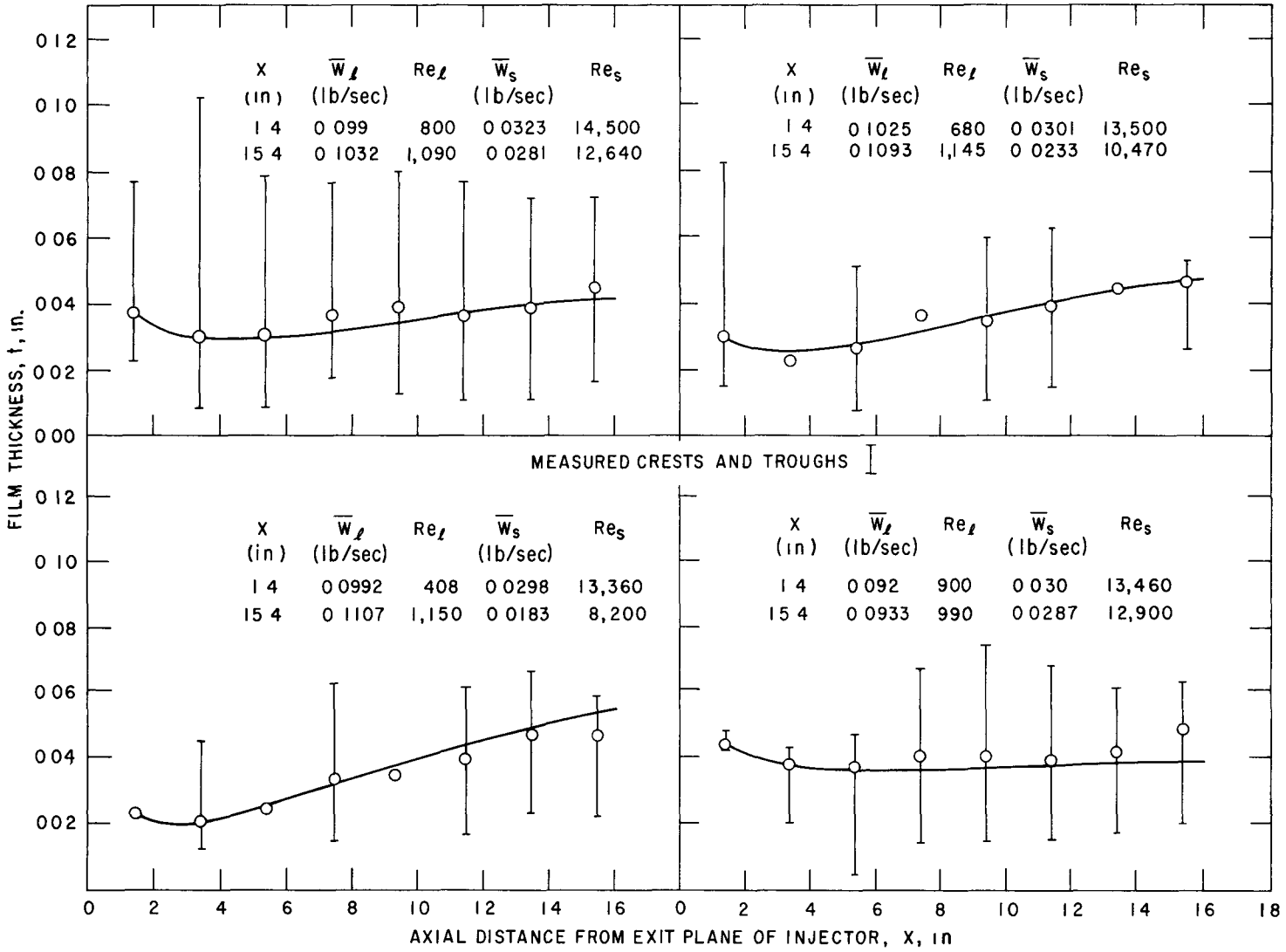

Fig. 25. Comparison of Model Predictions of Film Thickness vs. Data as a Function of Water Inlet Subcooling for $\overline{W}_\ell \simeq 0.1$ lb/sec, $\overline{W}_s \simeq 0.03$ lb/sec

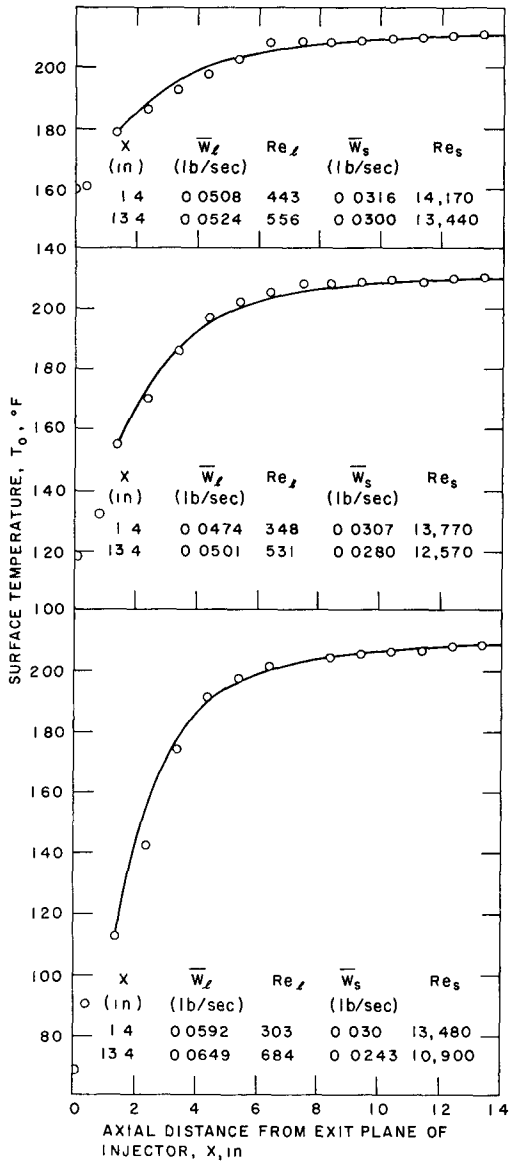

Fig. 26. Comparison of Model Predictions of Surface Temperature vs. Data as a Function of Water Inlet Subcooling for $\overline{W}_\ell \simeq 0.05$ lb/sec $\overline{W}_s \simeq 0.03$ lb/sec

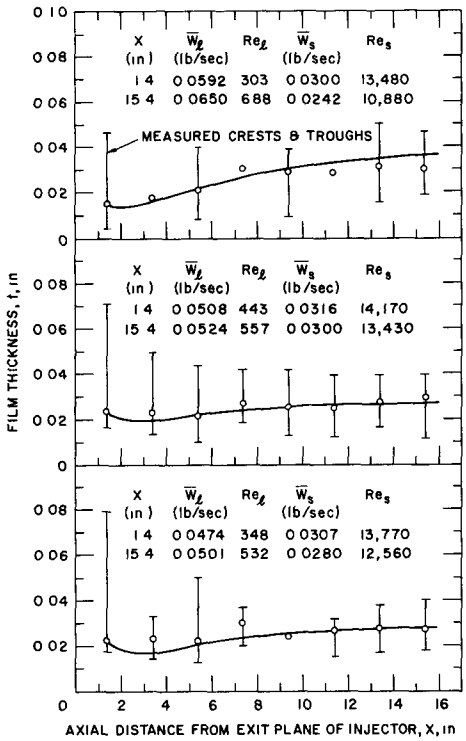

Fig. 27. Comparison of Model Predictions of Film Thickness vs. Data as a Function of Water Inlet Subcooling for $\overline{W}_\ell \simeq 0.05$ lb/sec, $\overline{W}_s \simeq 0.03$ lb/sec

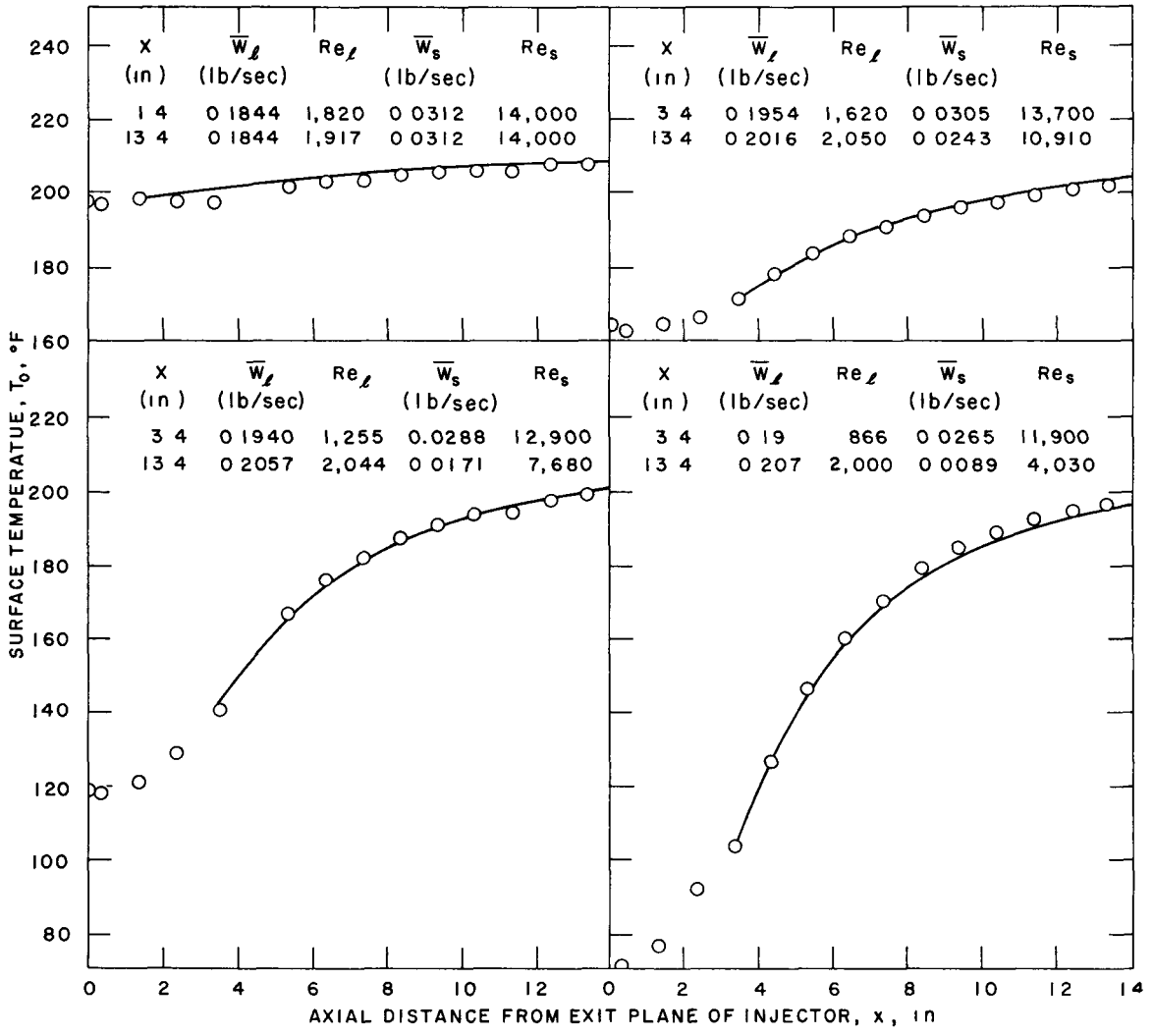

Fig. 28. Comparison of Model Prediction of Surface Temperature vs. Data as a Function of Water Inlet Subcooling for $\overline{W}_\ell \simeq 0.19$ lb/sec, $\overline{W}_s \simeq 0.03$ lb/sec

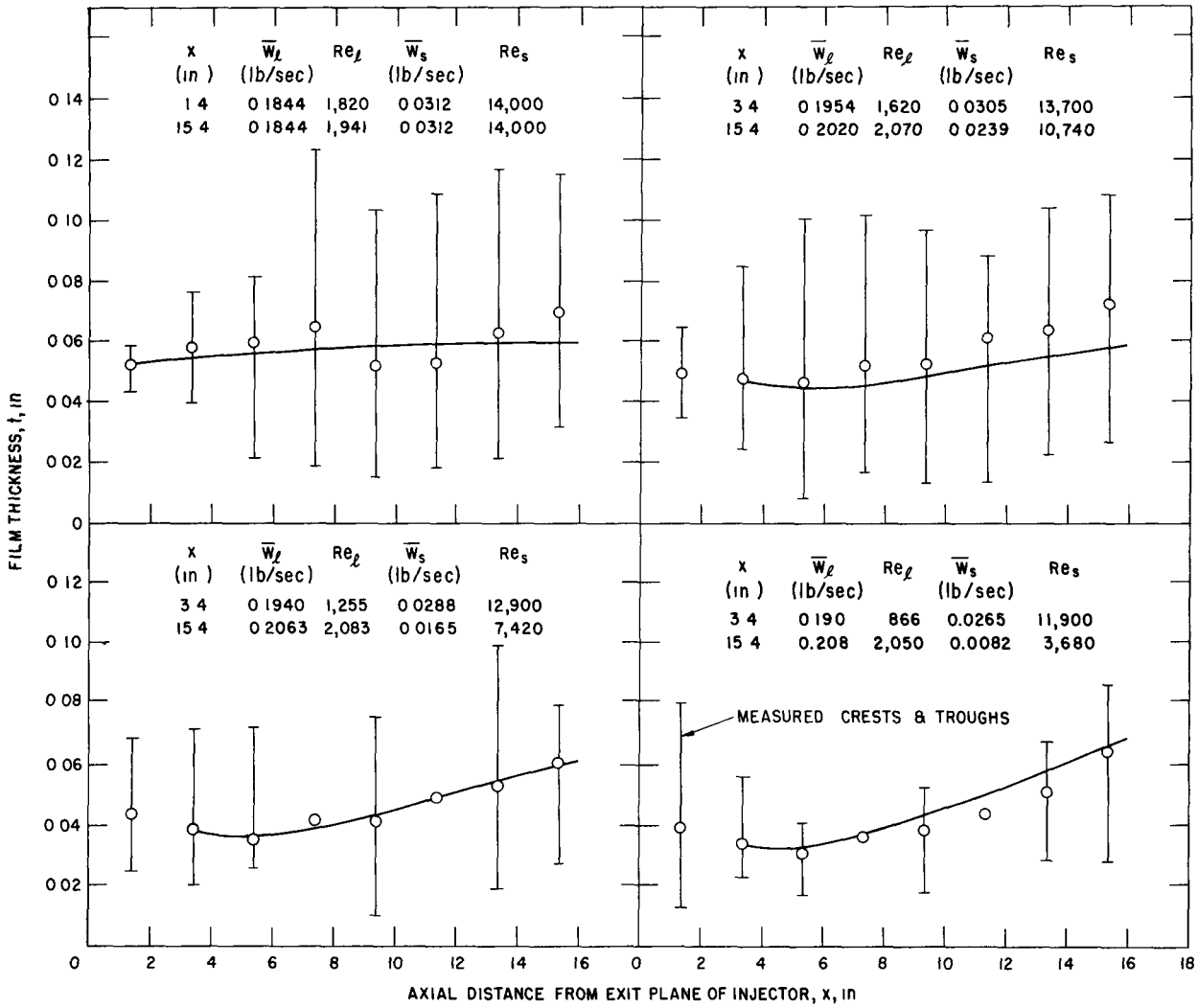

Fig. 29. Comparison of Model Predictions of Film Thickness vs. Data as a Function of Water Inlet Subcooling for $\bar{W}_\ell \approx 0.19$ lb/sec, $\bar{W}_s \approx 0.03$ lb/sec

In Figs. 30-33, the inlet-water flowrate is varied while the inlet subcooling in the film and the inlet-steam flowrate are approximately the same. As was observed in the air-water experiments, the largest water flowrate tended to decelerate most rapidly.

Figures 34-37 show the effect of vapor velocity for essentially constant initial film subcooling and inlet water flowrate. The momentum transferred to the film via the interfacial shear stress is increased as the vapor velocity increased. This is evidenced by the film-thickness measurements, which show that the film accelerates faster for the higher vapor flowrate.

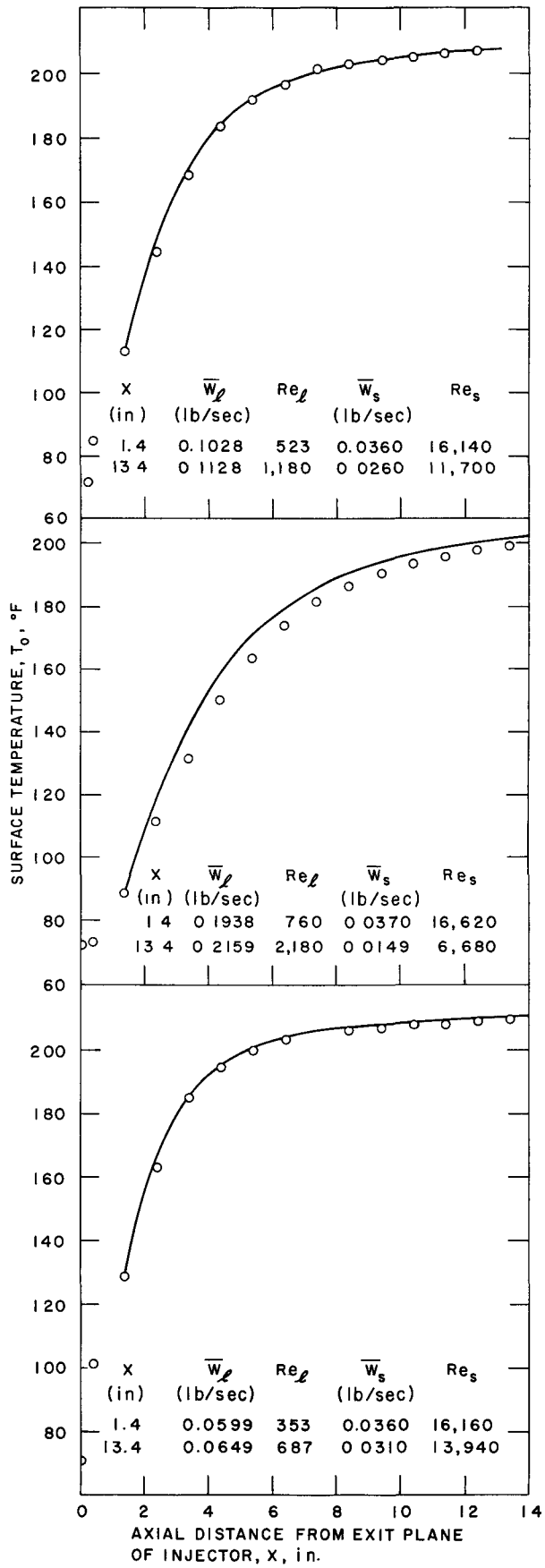

Fig. 30

Comparison of Model Predictions of Surface Temperature vs. Data as a Function of Inlet Water Flowrate for $\overline{W}_s \simeq 0.036$ lb/sec

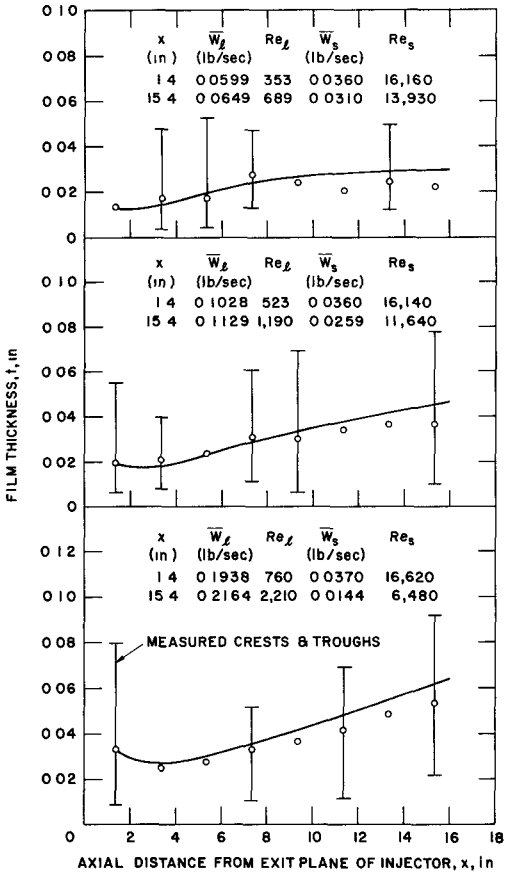

Fig. 31

Comparison of Model Predictions of Film Thickness vs. Data as a Function of Inlet Water Flowrate for $\overline{W}_s \simeq 0.36$ lb/sec

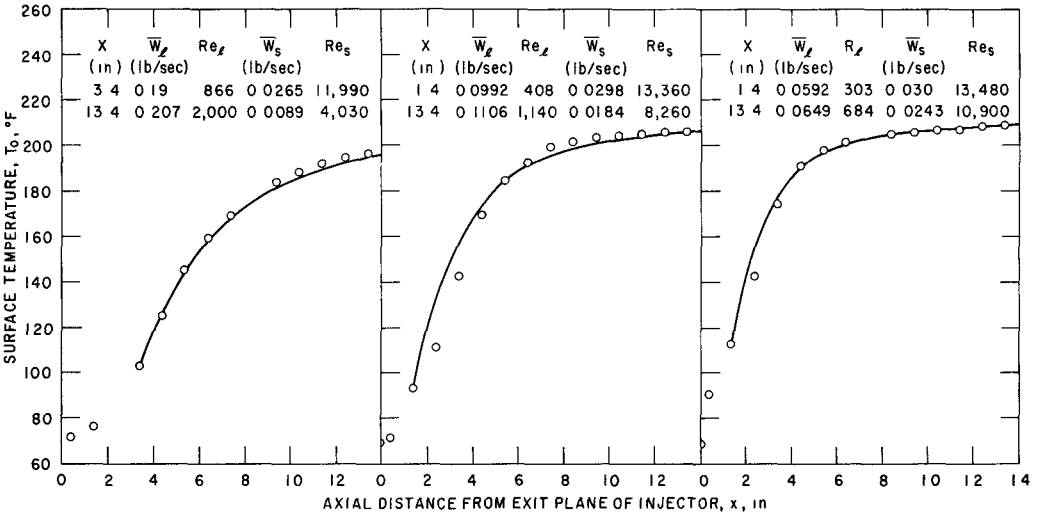

Fig. 32. Comparison of Model Predictions of Surface Temperature vs. Data as a Function of Inlet Water Flowrate for $\overline{W}_s \simeq 0.03$ lb/sec

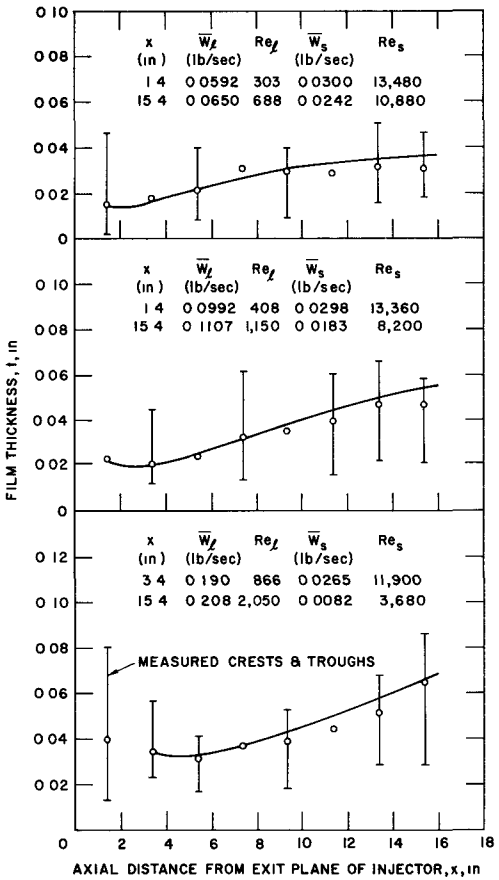

Fig. 33. Comparison of Model Predictions of Film Thickness vs. Data as a Function of Inlet Water Flowrate for $\overline{W}_s \simeq 0.03$ lb/sec

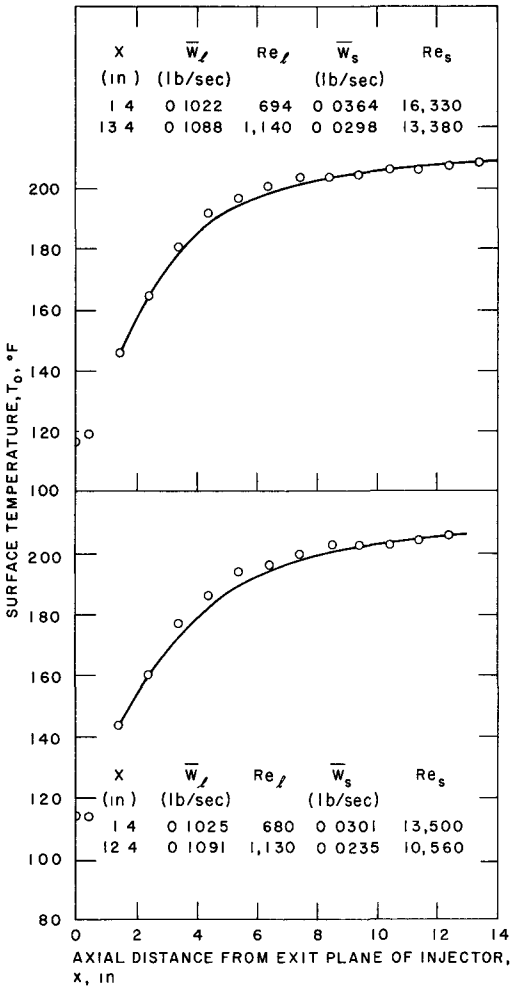

Fig. 34. Comparison of Model Predictions of Surface Temperature vs. Data as a Function of Inlet Steam Flowrate for $\overline{W}_\ell \simeq 0.1$ lb/sec

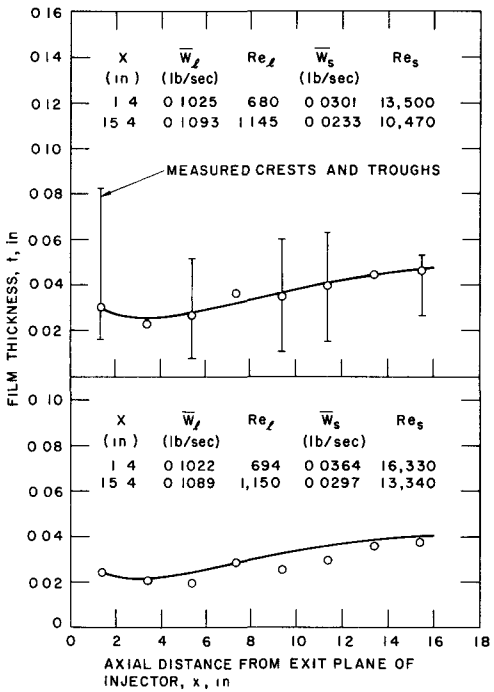

Fig. 35. Comparison of Model Predictions of Film Thickness vs. Data as a Function of Inlet Steam Flowrate for $\overline{W}_\ell \simeq 0.1$ lb/sec

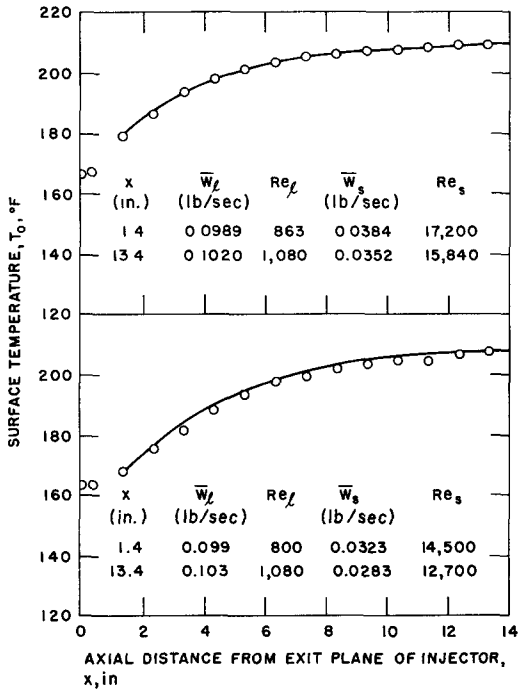

Fig. 36. Comparison of Model Predictions of Surface Temperature vs. Data as a Function of Inlet Steam Flowrate for $\overline{W}_\ell \simeq 0.1$ lb/sec

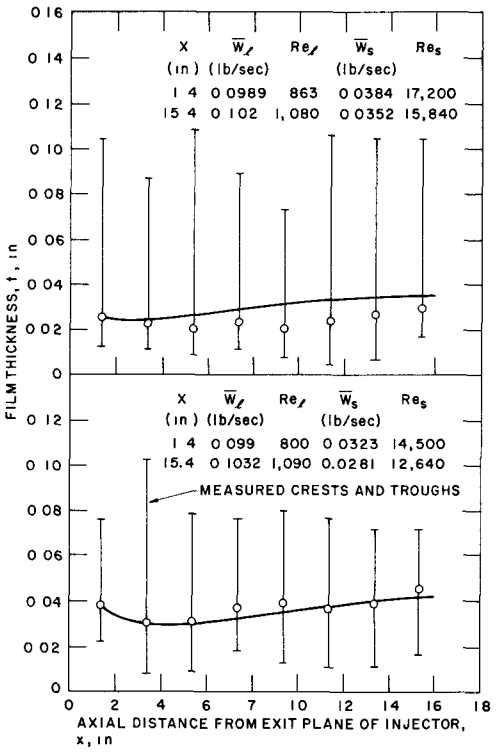

Fig. 37. Comparison of Model Predictions of Film Thickness vs. Data as a Function of Inlet Steam Flowrate for $\overline{W}_\ell \simeq 0.1$ lb/sec

c. Comparison of the Condensing Heat-transfer Coefficient with the Carpenter-Colburn Correlation. The heat-transfer coefficients calculated from Eq. 152 can be compared with those predicted by the correlation of Carpenter and Colburn,[7] which has been widely used in the literature. The Carpenter and Colburn correlation, written in terms of the parameters in this work, is

$$h = 0.043 \frac{k_\ell}{\mu_\ell} \rho_\ell^{1/2} \tau_i^{1/2} Pr_\ell^{1/2}.$$

Comparing the results of the two correlations over a wide range of conditions encountered in the experiments reported here showed that Eq. 152 yields values of h 2.5-4.2 times as much as the above equation does. This result is to be expected since the Carpenter-Colburn correlation was developed on the basis that the major resistance to heat transfer was located in the viscous region of the film near the wall. This region was neglected in developing Eq. 152 in which the overall resistance of the film was considered.

The magnitude of the condensing heat-transfer coefficient calculated by the model for the experiments of this research varied from 1100 to 5000 Btu/hr-ft^2-°F.

V. CONCLUSIONS AND RECOMMENDATIONS

The principal conclusions that can be made by considering the results of the theory and confirming experiments are:

1. The analytical models based on an integrated form of the two-dimensional boundary-layer-type equations are realistic descriptions of the interaction of stratified, turbulent, two-phase flows when the change in the thickness of the film in the direction of flow is small.

2. For two-component flow, the turbulent interfacial friction factors for both the three-dimensional and roll-wave regimes can be determined from simple linear functions of the film Reynolds number.

3. For one-component flows, the momentum transferred to the film via the interface shear stress is augmented by a term that is proportional to the product of the average vapor velocity times the condensation rate. If the effect of condensation rate on the interface shear stress is neglected, the predicted condensation rate is underestimated.

4. A model that emphasized the effect of the interfacial waves on the transport of heat in the film has been developed to describe film condensation on a subcooled film flowing over an adiabatic surface. This model predicts that the film Stanton number is a constant within the range of experimental error. The empirically determined value of the film Stanton number was 0.0073.

5. Use of the wall-layer model in evaluating the wall shear stress in the film is verified.

6. Due to the variation of film thickness in the direction of flow, the resulting hydrostatic pressure variation is a significant contribution to the deceleration of the film in instances where the water flowrate was low.

7. The transition from laminar to turbulent flow in the film is a function of the gas Reynolds number as well as the liquid Reynolds number.

Recommendations for the extension of the work presented in this report are:

1. Inclusion of the MHD effect in the analytical model, and evaluation of the relative merits of the one- and two-component film generator.

2. Consideration of possible alteration of the model developed in this work to describe film condensation where the axial gradient of the film thickness is not small. A practical example of this is the case in which all the steam condenses and the liquid phase fills the channel.

3. Application of the model for the condensing heat-transfer coefficient to the case of condensation on a jet. A practical example of this is the condensing injector.

APPENDIX A

Discussion of Errors in Measurements of Film Thickness

To put into better perspective the relationship between the film thickness measured by the conductance probes in the air-water experiments and by the needle-contact probe in the steam-water experiments, possible sources of error will be discussed. In part, this question of error has already been discussed when, in Section III.B.5, the needle-contact probes and conductance probes were compared through air-water experiments. The agreement was good; however, the relationship between the measured mean film thicknesses and the actual mean film thickness must be examined in light of possible inherent errors in each method.

Considering first the conductance probes, a possible significant source of error results from the nonlinearity of the relationship between C and t, as evidenced in Fig. 10. In data acquisition, the voltage measurements were averaged with time, the film thickness was determined from an average value of C. However, since C varies nonlinearly with t, and waves are present at the air-water interface, the average value of C does not necessarily correspond to the average value of t. For the smaller film thicknesses, the calibration curve is approximately linear; therefore, the average of C is approximately equal to the average of t. This conclusion is verified in Table I. However, for larger values of t, waves might cause significant errors. To test the magnitude of the possible error, the calibration curve is approximated from t = 0.04 to 0.14 in. by the relationship

$$C = 0.6t^{0.7}.$$

Since the actual form of the waves is unknown, it is assumed, for purposes of discussion, that the waves have a sawtooth shape and the heights of the crests and troughs of the waves are 0.14 and 0.04 in., respectively. The "true" average film thickness is then 0.09 in. The average film thickness determined by integrating C over one period of the wave is 0.086 in. Thus, the film thickness calculated by averaging C is approximately 4.5% too low. Although this discussion is limited by the lack of quantitative information concerning the actual wave form, it is somewhat conservative with regard to the estimation of the wave amplitudes. The amplitudes of the waves were estimated by observing the conductance-probe voltage on an oscilloscope. For the films that tended to thicken (decelerate), as occurred when the air flowrate was low, the wave amplitudes were smaller than those assumed in the preceding discussion. This means that averages are taken over smaller ranges of t, and as the range of t decreases, the variation of C with t becomes more linear. Thus, the error due to the method of averaging leads to a measured mean film thickness for the larger values of t approximately 5% less than the actual mean film thickness.

Another possible source of error in the measurements made with the conductance probes is due to the fact that the measured mean film thickness is actually a three-dimensional average. Tests made on the calibration cell to determine the range of the field affecting the current flow through the liquid indicated that the field was concentrated in the region between the two probes. Since the variation in film thickness was small, of the order of 10^{-3} in./in., this error was negligible.

In the needle-contact-probe method of measuring film thicknesses, a possible source of error is due to contact hysteresis; i.e., surface forces depress the liquid when the needle is initiating contact and extend the liquid when the probe is exiting the liquid. McManus[36] stated that because the liquid is flowing and the surface is agitated, this effect is negligible. The results in Table I appear to support this conclusion.

Another source of error was a result of the method of measurement. In the determination of the relative contact time, the position of the needle-contact probe was noted when the current reading was 50% of the value measured when the needle touched the troughs of the waves. Since the microammeter used was a relatively slowly responding instrument, most of the fluctuations in the readings were "integrated out." However, for the experiments in which the wave activity was largest, determination of the current reading, within the fluctuations present, was difficult, since current did not vary significantly with small displacements of the needle-contact probe on either side of the mean film thickness. This made it difficult to decide on the location of the mean film thickness. In general, the maximum error attributable to the method of measurement was conservatively estimated at ± 0.002 in.

APPENDIX B

Details of Computer Computation

The method of computer computation was essentially the same for both the one- and two-component analytical models. The governing momentum equations were a pair of simultaneous, nonlinear, ordinary differential equations, whose dependent variables were the film thickness, t, and the static pressure, P. Given initial values of t and P at some value of x, successive values of t and P at $x + m\Delta$ were evaluated in a step-by-step manner by using a Taylor series. The first derivative in the Taylor series could be used when Δ was chosen as 0.001 in. Choosing Δ as 0.00001 in. produced no noticeable change in the results. The first derivatives were evaluated by simultaneously solving the momentum equations for dt/dx and dP/dx. In the one-component model, the variation of T_0 with x was found in a similar manner.

Calculations were performed on the CDC-3600 Computer. Typical computing times were approximately 2 min for each set of input data in the one-component model and approximately 1 min for each set of input data in the two-component model.

Data on the physical properties of air were taken from Eckert and Drake.[18] The properties of steam and water were taken from Keenan and Keyes[30] and Kestin and Whitelaw.[31]

The flow diagrams of the computer programs used in this model computations are shown in Figs. B.1 and B.2.

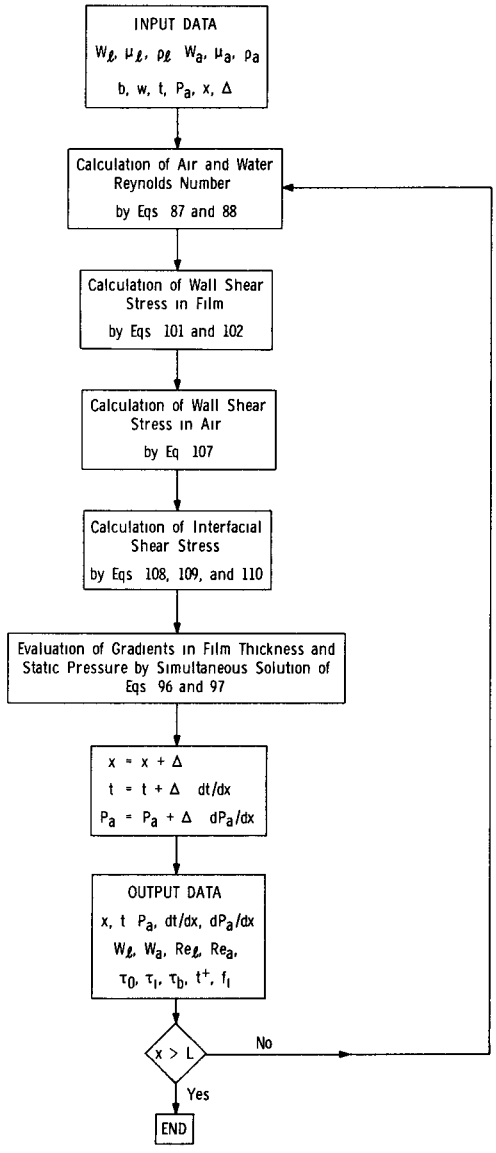

Fig. B.1. Flow Diagram for Two-component Computer Program

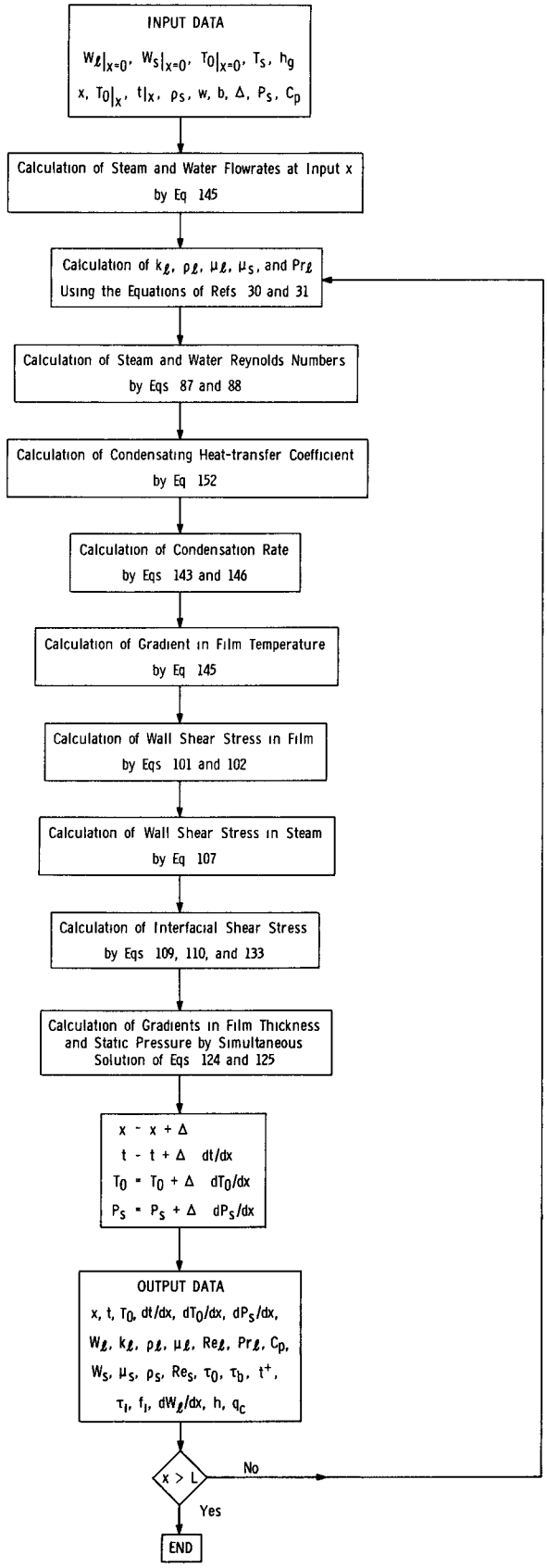

Fig. B.2. Flow Diagram for One-component Computer Program

ACKNOWLEDGMENTS

I wish to express my sincere appreciation to Professor M. M. El-Wakil for his assistance and encouragement throughout my graduate program at The University of Wisconsin. In addition, I am indebted to Dr. Michael Petrick for suggesting the problem and offering his valuable guidance in support of the research.

This research was performed under the auspices of the U.S. Atomic Energy Commission at the Argonne National Laboratory through joint support of the Reactor Engineering Division and Associated Midwest Universities Fellowship Program. In addition, the support of the Ford Foundation while in residence at The University of Wisconsin is gratefully acknowledged.

The assistance rendered by the staff of Building 11 throughout the experimental program of this report is appreciated. In particular, Messrs. M. P. Gats and G. A. Lambert contributed substantially to the success of the experiments.

REFERENCES

1. Akers, W. W., Deans, H. A., and Crosser, O. K., *Condensing Heat Transfer Within Horizontal Tubes*, Chem. Engr. Prog. Sym. Series *55*, No. 29. 171 (1959).

2. Altman, M., Staub, F. W., and Norris, R. H., *Local Heat Transfer and Pressure Drop for Refrigerant-22 Condensing in Horizontal Tubes*, Chem. Engr. Prog. Symp. Series *56*, No. 30, 151 (1960).

3. *Analysis, Criteria Development, and Design of an Orbital Condensing Heat Transfer Experiment*, AiResearch Report No. 67-1797-1, *2*, Los Angeles, Calif. (1967).

4. Anderson, G. H., and Mantzouranis, B. G., *Two-Phase (gas-liquid) Flow Phenomena-I*, Chem. Engr. Sci. *12*, 109 (1960).

5. Bergelin, O. P., Kegel, P. K., Carpenter, F. G., and Gazley, C., *Co-Current Gas-Liquid Flow, II: Flow in Vertical Tubes*, Heat Transfer and Fluid Mechanics Institute, Berkeley, Calif. *19* (1949).

6. Borchmann, J., *Condensation of R-11 and Steam in Annuli at High Vapor Velocities*, Proc. International Institute of Refrigeration, Low Temperature Heat Transfer *1* (1967).

7. Carpenter, E. F., and Colburn, A. P., *The Effect of Vapor Velocity on Condensation Inside Tubes*, Proc. General Discussion on Heat Transfer, Institution of Mech. Engr. *20* (1951).

8. Carpenter, F. G., *Heat Transfer and Pressure Drop for Condensing Pure Vapors Inside Vertical Tubes at High Vapor Velocities*, Ph.D. thesis, University of Delaware (1948).

9. Cohen, L. S., *Interaction between Turbulent Air and a Flowing Liquid Film*, Ph.D. thesis, Dept. of Chem. and Chem. Engr., University of Illinois (1964).

10. Colburn, A. P., *Note on the Calculation of Condensation When a Portion of Condensate Layer Is in Turbulent Motion*, Trans. A.I.Ch.E. *30*, 187 (1933).

11. Collier, J. G., and Hewitt, G. F., *Data on the Vertical Flow of Air-Water Mixtures in the Annular and Dispersed Flow Regions*, Part II, Trans. Inst. Chem. Engrs. (London) *39*, 127 (1961).

12. Collier, J. G., and Hewitt, G. F., *Film Thickness Measurements in Two-Phase Flow*, British Chemical Engineering *12*, No. 5, 709 (1967).

13. Deissler, R. G., *Analysis of Turbulent Heat Transfer, Mass Transfer, and Friction in Smooth Tubes at High Prandtl and Schmidt Numbers*, NACA Rept. 1210 (1955).

14. Dukler, A. E., and Bergelin, O. P., *Characteristics of Flow in Falling Liquid Films*, Chem. Eng. Progress *48*, 557 (1952).

15. Dukler, A. E., *Fluid Mechanics and Heat Transfer in Vertical Falling-Film Systems*, Chem. Engr. Progr. Symp. Ser. *56*, 1 (1959).

16. Dukler, A. E., *Comparison of Theoretical and Experimental Film Thickness*, ARS Journal *31*, 86 (1961).

17. Dukler, A. E., *Discussion of Paper 132,* Proc. Third International Heat Transfer Conference *6,* Chicago (1966).

18. Eckert, E. R. G., and Drake, R. M., Jr., *Heat and Mass Transfer,* 2nd Edition, McGraw-Hill Book Co., New York (1959).

19. Fulford, G. D., "The Flow of Liquids in Thin Films," *Advances in Chemical Engineering,* Vol. 5, Academic Press, New York, N.Y. (1964).

20. Gill, L. E., and Hewitt, G. F., *Further Data on the Upwards Annular Flow of Air/Water Mixtures,* A.E.R.E.-R 3935 (1962).

21. Grace, H. P., and Lapple, C. E., *Discharge Coefficients of Small-Diameter Orifices and Flow Nozzles,* Trans. A.S.M.E. *73,* 639 (1951).

22. Hanratty, T. J., and Engen, J. M., *Interaction Between a Turbulent Air Stream and a Moving Water Surface,* A.I.Ch.E. J. *3,* 299 (1957).

23. Hanratty, T. J., and Woodmansee, D. E., "Stability of the Interface for a Horizontal Air-Liquid Flow," *Proceedings and Summaries of the Symposium on Two Phase Flow,* University of Exeter (1965).

24. Hershman, A., *The Effect of Liquid Properties on the Interaction Between a Turbulent Air Stream and a Flowing Liquid Film,* Ph.D. thesis, Dept. of Chem. and Chem. Engr., University of Illinois (1960).

25. Hilding, W. E., and Coogan, C. H., Jr., *An Experimental and Analytical Study of the Heat Transfer and Flow Mechanics of Vapor Condensing at High Velocities in Small Straight Tubes,* University of Connecticut, Stowes, Connecticut (Dec 1965).

26. Hilding, W. E., "Differential Equations for the Local Interfacial and Wall Shear Stresses for One-Dimensional Annular Two-Phase Flow," *Proc. Third International Heat Transfer Conference,* Paper No. 132, *4,* Chicago (1966).

27. Hewitt, G. F., King, R. D., and Lovegrove, P. C., *Techniques for Liquid Film and Pressure Drop Studies in Annular Two-Phase Flow,* A.E.R.E.-R 3921 (1962).

28. Hewitt, G. F., and Lovegrove, P. C., *Comparative Film Thickness and Holdup Measurements in Vertical Annular Flow,* A.E.R.E.-M 1203 (1963).

29. Jacob, M., Erk, S., and Eck, H., Forsch. Gebiete Ingenieruw *3,* 161 (1932).

30. Keenan, J. H., and Keyes, F. G., *Thermodynamic Properties of Steam,* John Wiley and Sons (1959).

31. Kestin, J., and Whitelaw, J. H., *Sixth International Conference on the Properties of Steam-Transport Properties of Water Substance,* J. of Engr. Power, Trans. ASME (1966).

32. Kirkbride, C. G., *Heat Transfer by Condensing Vapor on Vertical Tubes,* Trans. A.I.Ch.E. *30,* 170 (1933).

33. Lilleleht, L. W., and Hanratty, T. J., *Relation of Interfacial Shear Stress to the Wave Height for Concurrent Air-Water Flow,* A.I.Ch.E. J. *7,* 548 (1961).

34. Lockhart, R. W., and Martinelli, R. C., *Proposed Correlation of Data for Isothermal Two-Phase, Two-Component Flow in Pipes,* Chem. Engr. Prog. *45,* 39 (1944).

35. Lodge, A. S. *Elastic Liquids*, Academic Press, New York, New York (1964).

36. McManus, H. N., Jr., *An Experimental Investigation of Film Characteristics in Horizontal Annular Two-Phase Flow*, A.S.M.E. paper 62-WA-170 (1957).

37. Meyers, J. A., and Rosson, H. F., *Condensing Coefficients Inside a Horizontal Tube Near Atmospheric Pressure*, Chem. Engr. Progress Symp. Series *57*, No. 32, 150 (1960).

38. Mickley, H. S., Ross, R. C., Squyers, A. L., and Stewart, W. E., *Heat, Mass, and Momentum Transfer for Flow Over a Flat Plate With Blowing or Suction*, NACA-TN-3208 (1954).

39. Nusselt, M., *Die Oberflacken Konclensation Des Wasserdampfes*, Z. des Vereines Deutscher Ingenieure *60*, 541 (1916).

40. Rohsenow, W. M., Webber, J. H., and Ling, A. T., *Effect of Vapor Velocity on Laminar and Turbulent-Film Condensation*, Trans. ASME, *78*, 1637 (1956).

41. Schlichting, H., *Boundary Layer Theory*, 4th Edition, McGraw-Hill Book Co., New York, New York (1960).

42. Shearer, C. J., and Nedderman, R. M., *Pressure Gradient and Liquid Film Thickness in Co-Current Upwards Flow of Gas/Liquid Mixtures: Application to film-cooler design*, Chem. Engr. Sci. *20*, 671 (1965).

43. Silver, R. S., *An Approach to a General Theory of Surface Condensers*, Proc. Instn. Mich. Engr. *178*, (Pt. 1, No. 14), 339 (1963-64).

44. Silver, R. S., and Wallis, G. B., *A Simple Theory for Longitudinal Pressure Drop in the Presence of Lateral Condensation*, Proc. Insts. Mech. Engr. *180*, (Pt. 1, No. 1), 36 (1965-66).

45. Soliman, M., Schuster, J. R., and Berenson, P. J., *A General Heat Transfer Correlation for Annular Flow Condensation*, ASME Paper 67-WA/HT-12 (1967).

46. Subbotin, V. I., Invanovskei, M. N., Sorokin, V. P., and Chulkov, B. A., *Heat Transfer During the Condensation of Potassium Vapor*, Trans. from Teplofizika Vysokikh Temperatur *2*, 616 (1964).

47. Sukhatme, S. P., and Rohsenow, W. M., *Heat Transfer During Film Condensation of a Liquid Metal Vapor*, Report No. 9167-27, MIT (1964).

48. Van Rossum, J. J., *Experimental Investigation of Horizontal Liquid Films-Wave Formation, Atomisation, Film Thickness*, Chem. Engr. Sci. *11*, 35 (1959).

49. von Kármán, T., *The Analogy Between Fluid Friction and Heat Transfer*, Trans. Am. Soc. Mech. Engrs. *61*, 705 (1939).

50. Wallis, G. B., *Two-Phase Flow and Boiling Heat Transfer*, Report No. NYO-3114-14 (1966).

51. Wilhelm, D. J., *Condensation of Metal Vapors: Mercury and the Kinetic Theory of Condensation*, ANL-6948 (Oct 1964).